DESIGN AND VALIDATION OF NOVEL ELECTRICALLY ROTATING EDDY CURRENT PROBES

By

Chaofeng Ye

A DISSERTATION

Submitted to
Michigan State University
in partial fulfillment of the requirements
for the degree of

Electrical Engineering - Doctor of Philosophy

2016

ABSTRACT

DESIGN AND VALIDATION OF NOVEL ELECTRICALLY ROTATING EDDY CURRENT PROBES

By

Chaofeng Ye

Airframe structures typically are composed of multiple layers of aluminum that riveted together using thousands of aluminum, titanium or steel fasteners. These fastener sites are areas of high stress where cracks originate in radial directions. Inspection of multilayered riveted structures and detection of subsurface cracks under fastener head is a major challenge in aviation industry. Some of the difficulties include:

i) defects embedded deep in the structure, ii) arbitrary and unknown orientation of defects, iii) remanence magnetic of steel fasteners which shifts the operation point of the giant magnetoresistance (GMR) sensor out of linear range, iv) detection of small amplitude defect indications in the presence of dominant response signals from fasteners, v) effect of material properties of steel fasteners such as anisotropy, hysteresis, etc. vi) effect of earth's magnetic field on weak magnetic field measurements using GMR sensors.

This dissertation presents an in-depth analysis of these issues and a novel probe design for potentially addressing these problems. The operating principles of the probe is based on inducing eddy currents in the conducting test sample and measuring the perturbations in induced magnetic fields associated with the eddy currents. The sensor system utilizes a very low frequency rotating current excitation that is sensitive to deep embedded cracks of all orientations. An array of GMR sensors are used to measure the induced fields. The contributions of this research are the following: 1) orthogonal coil design for generating

rotation excitation current, 2) novel differential sensor array scheme that eliminates the ambient/background field at sensors, 3) a new optimized non-uniform multilayer coil design for ensuring uniform excitation field; 4) analysis of effect of magnetic susceptibility and anisotropy of steel fastener; 5) magnetic balance measurement scheme using high sensitivity GMR sensor for steel rivets; 6) design and develop a prototype probe with rotating excitation and GMR array sensors 7) evaluate the probe performance for experimental validation of the overall hypothesis.

The second application considered in this research is development of electrically rotating field/current probes for inspection of cylindrical geometry. Two novel probes are studied. The first design is a transceiver probe based on generating rotating fields using three phase windings. The key features of this design are high inspection speed, sensitivity to cracks of arbitrary orientation and simplicity of design. The second probe is based on rotating current excitation using orthogonal coils in axial and circumferential directions. The radial component of the magnetic field is picked up by a linear array of GMR sensors located along the circumferential direction. This probe can detect both circumferential and axial defects, offers high sensitivity over a wide range of frequencies and can potentially provide extremely high spatial resolution.

ACKNOWLEDGEMENTS

I would like to express my sincere gratitude to my advisor and mentor, Dr. Lalita Udpa and Dr. Satish Udpa, for their extraordinary support, guidance and encouragement during my Ph.D study. Special thanks to their invaluable guidance and help in my writing. They have advised me not only on my research, but also on my career and life. I feel fortunate to work with them and proud of being a member of NDEL research group.

I would like to thank my PhD studies committee: Dr. Antonello Tamburrino and Dr.

Rigoberto Burgueno for their time, guidance and suggestions.

I would like thank my colleagues of NDEL for their support and help. Many thanks go to Dr. Yue Huang, for his guidance and help both in my research and life.

I would like to express my heartfelt gratitude to my family, especially my wife, for their constant support and encouragement. I would like to thank my beloved children for their love and companionship.

TABLE OF CONTENTS

LIST OF TABLES	. viii
LIST OF FIGURES	ix
Chapter 1 Introduction	1
1.1 Introduction to Nondestructive Testing	
1.2 Introduction of Rotating Current/Field Probes	
1.2.1 Rotating currents	
1.2.2 Rotating fields	
1.3 Statement of Problem	
1.3.1 Multi-layered Riveted Structure Inspection	4
1.3.2 Steam Generator Tube Inspection	
1.4 Research Objectives	8
1.5 Methodologies	
1.6 Organization of This Thesis	
Chapter 2 Review of Electromagnetic NDE	10
2.1 Electromagnetic NDE techniques	
2.1.1 Static Electromagnetic Methods	
2.1.1.1 Magnetic Flux Leakage Method	
2.1.1.2 Electrical Impedance Tomography (EIT)	
2.1.2 Low Frequency Methods	
2.1.2.1 Conventional Eddy Current Method	
2.1.2.2 ECT with Magnetic Field Measurement Method	
2.1.3 High Frequency Methods	
2.1.3.1 Microwave NDE	14
2.1.3.2 Terahertz Tomography	15
2.1.4 Time Domain Measurement Methods	16
2.1.4.1 Pulsed Eddy Current	16
2.1.4.2 Time-domain Reflectometry	
2.2 Formulation of Eddy Current Problem	19
2.2.1 Maxwell Equation in Eddy Current Problem	19
2.2.2 Formulations - Magnetic Vector Potential	
2.2.3 Reduced Magnetic Vector Potential	21
2.2.4 Penetration Depth	22
2.3 Magnetic Sensors in NDE	24
2.3.1 Comparison of Magnetic Sensors	25
2.3.2 GMR Sensor	27
Chapter 3 Introduction of EC-GMR Probe for Multilayer Structure Inspection	29
3.1 Single Excitation Coil	
3.2 RoC-GMR Probe with Orthogonal Excitation Coils	
3.3 Issues of RoC-GMR Probe with Array Sensors	
3.3.1 Non-Uniform Background Magnetic Field	
3.3.2 Non-Uniform Induced Eddy Currents	

3.4	Conclusion	38
Chapter 4	Novel RoC-GMR Probe with Array Sensors	39
4.1	Differential Measurement Method	39
4.1.1	Operating Principle	39
4.1.2		
4.2	Optimization of Rotating Current Excitation Coil	44
4.2.1	Current Distribution Optimization	44
4.2.2		
4.2.3	B Effect of Air Gap Width	49
4.2.4	Coil Design	50
4.2.5	Performance Analysis	52
4.	2.5.1 Induced Eddy Current	52
4.	2.5.2 Detection of Subsurface Defects at Different Locations	53
4.	2.5.3 Detection of Defect under Fastener Head	54
4.3	Experiment Results and Discussion	57
4.3.1	Experiment Setup	57
4.3.2	2 Inspection of Off-center Defect	61
4.3.3	B Effect of Defect Length	62
4.3.4	Effect of Crack Orientation	64
4.4	Conclusion	65
Chapter 5	Inspection of Steel Fasteners	67
-	Introduction	
5.1.1	Properties of Ferromagnetic Materials	68
5.1.2	Rayleigh Relations	69
5.	1.2.1 3D Rayleigh Relations	69
5.1.3	Geomagnetic Field	71
5.2	Effect of Magnetic Anisotropy	71
5.2.1	C-scan Image of Anisotropic FastenerSimulation	72
5.2.2	2 Experimental Measurement with External DC Field	76
5.2.3	B Effect of Geomagnetic Field	78
5.3	Magnetic Balance Measurement Method	80
5.3.1	Operating Principle	80
5.3.2	2 Effect of the Compensation Coil on Defect Signal	83
5.3.3	Numerical Analysis	84
5.3.4	1	
5.4	Experimental Output Signal of Magnetized Steel Fastener	
5.4.1	1 1	
5.4.2	1	
5.5	Conclusion	91
Chapter 6	Transceiver RoF-EC Probe for Tube Inspection	93
6.1	Introduction	93
6.1.1	Bobbin Probe	93
6.1.2	2 Rotating Probe	94
6.1.3	3 Array Probe	95
6.1.4	\mathcal{E}	
6.2	Rotating Field Transceiver Probe - Structure and Principle	97
6.3	Defect signals from Transceiver Probe	99

6.3.1 FEM model	99
6.3.2 Flat Bottom Hole	99
6.3.3 Axial and Circumferential Notch	101
6.3.3.1 Effect of Defect Depth	
6.3.3.2 Effect of Defect Lengths	102
6.3.3.3 Effect of Circumferential Location of Defect	103
6.3.3.4 Effect of ID and OD Defects	104
6.4 Experiment Validation	
6.4.1 Prototype Probe Design and Experiment Setup	105
6.4.2 Flat Bottom Hole	107
6.4.3 Axial and Circumferential Notch	108
6.5 Conclusion	110
Chapter 7 RoC-GMR Probe for Tube Inspection	
7.1 Motivation	
7.2 Operation Principle	
7.3 Simulation Result of Eddy Current in Tube Wall	
7.3.1 Circumferential Current	115
7.3.2 Axial Current	
7.4 Simulated Signals using RoC-GMR Probe	
7.4.1 Axial and Circumferential Notch	
7.4.2 Effect of Defect Depth	
7.4.3 Effect of Defect Length	120
7.4.4 Flat Bottom Hole	121
7.5 Prototype Probe Design	122
7.6 Experimental Results and Discussion	
7.6.1 Axial and Circumferential Notches	124
7.6.2 Flat Bottom Hole	127
7.7 Conclusion	128
Chapter 8 Summary and Future Work	
8.1 Accomplishments and Conclusions	130
8.2 Future Work	131
8.2.1 RoC-GMR probe for multilayer structure inspection	131
8.2.2 RoC-GMR probe for tube inspection	131
BIBLIOGRAPHY	133

LIST OF TABLES

Table 2.1. Magnetic field sensor characteristics.	25
Table 4.1. Minimum coil size satisfying $\eta < 10$ for different air gap width	50
Table 5.1.Earth's magnetic field at East Lansing, Michigan, USA	71
Table 5.2. Material properties of the 3D FEM model	72
Table 6.1. Parameters of transceiver rotating field probe	.106
Table 6.2. Axial location of the defects and correlated signal peak	.110

LIST OF FIGURES

Figure 1.1. (a) Excitation currents with different orientation and phase angle. (b) Induced rotating eddy current in test sample
Figure 1.2. (a) Top view of probe current and magnetic field. (b) Induced eddy current in tube wall
Figure 1.3. Layered structure:(a) Aircraft riveted skin structure geometry and(b) hidden crack at fastener sites
Figure 1.4. Schematic of a steam generator in nuclear power plant
Figure 2.1.Detection principle of current field measurement method14
Figure 2.2. Transient response associated with defects at different depth[42]17
Figure 2.3. Schematic diagram of instrumentation for time domain measurement18
Figure 2.4. Typical eddy current problem
Figure 2.5. Penetration depth of eddy current
Figure 3.1. (a) A unidirectional coil with a GMR sensor array at the coil symmetry line for inspecting a layered riveted plate. (b),(c), (d) Induced eddy currents when there is no discontinuity, fastener, and fastener with a defect, respectively[68]30
Figure 3.2. Simulation results of a unidirectional coil with a GMR sensor array at the coil symmetry line. Image of (a) defect free fastener, (b) fastener with defect perpendicular to the current and (c) fastener with defect parallel to the current30
Figure 3.3.Design of the planar excitation coil with a rotating current field. (a) Unidirectional coil with a linear current $I0\cos(\omega t + 90^{\circ})$,. (b) Unidirectional coil with linear current $I0\cos(\omega t)$. (c) The two unidirectional coils producing a rotating current, with the GMR sensor at the center
Figure 3.4. Simulation results of rotating current excitation with single sensor. Image of (a) defect free fastener, (b) fastener and horizontal defect and (c) fastener and vertical defect
Figure 3.5. Experiment setup for rotating current EC-GMR probe with signal sensor
Figure 3.6. (a) Top view of aluminum test sample. (b) Experimental result of rotating current EC-GMR probe with single sensor
Figure 3.7. (a) Background field measured on defect free sample (b) Sample/defect geometry (c) Field measured on the test geometry shown in (b)34

Figure 3.8. (a) Field Image after background subtraction. Line scan of B_z at $y=0$ (b) Real part (c) Imaginary part
Figure 3.9. Induced magnetic flux density Bx (a) and eddy currents Jy (b) in aluminum sample due to y direction coil on y=0 plane
Figure 3.10. Signal (Bz) of defect located at x=0mm and x=25.6mm37
Figure 4.1.Schematic arrangement of the probe showing 3D view of the orthogonal coils and two GMR arrays
Figure 4.2.3D view showing spatial relationship between coil 2 and the sensor arrays.
Figure 4.3. Dimensions of the test sample and sensor arrays location
Figure 4.4. Simulation results showing amplitude of Bz for aluminum fastener with radial notch (length l_d =10mm,orientation α =0°) at (a) z=1 mm. (b) z=9 mm.(c) Differential Image (d) Differential Image after baseline subtraction43
Figure 4.5. Simulation result for cases (a) l_d =0 mm (no crack). (b) l_d =10 mm, α =30 °. (c) l_d =10 mm, α =60 °. (d) l_d =10 mm, α =90 °
Figure 4.6. Lateral view of the y direction excitation coil and sensor array45
Figure 4.7.Theoretical current density vs. x for different parameter 'a'
Figure 4.8. η defined as equation (4.32) vs. parameter 'a'
Figure 4.9. η vs. parameter 'a' for different air gap width
Figure 4.10. Optimization result: (a) current density vs. x and (b) wire distance vs. x
Figure 4.11. Top view of the optimized coil
Figure 4.12:Numerical calculation results of (a) Bx at the observation points (z=-6mm) and (b) Bz at the sensors locations (z=2mm) of optimized coil and uniform coil52
Figure 4.13. Eddy current in aluminum plane induced by optimized non-uniform coil (a) and conventional uniform coil (b)
Figure 4.14. Eddy current in aluminum sample at depth of 5mm from surface53
Figure 4.15. (a) Lateral view of test sample and coil; (b) Simulation results of defect located at x=0 mm and x=30mm after background subtraction
Figure 4.16. Dimensions of the test sample in the FEM model55
Figure 4.17. Simulation results for cases: (a)uniform coil, fastener center located at $x=0$ mm, (b) uniform coil, fastener center located at $x=20$ mm, (c) optimized non-

uniform coil, fastener center located at x=0mm, (d) optimized non-uniform coil, fastener center located at x=20mm
Figure 4.18. Simulation result of defect free fastener
Figure 4.19. Comparison of reduction of ϵ of conventional uniform coil and optimized coil
Figure 4.20. Typical output voltage of GF708 vs. magnetic flux density[73]58
Figure 4.21. Design of the sensor board
Figure 4.22. (a) Sensor connection diagram for each array (b) Circuit diagram of differential measurement probe
Figure 4.23. Schematic diagram of the experimental system
Figure 4.24. Lateral (a) and top (b) view of the two layers aluminum sample60
Figure 4.25. Experiment results of non-defect fastener generated with (a) optimized non-uniform coil probe; (b) conventional uniform coil probe
Figure 4.26. Comparison of experimental deformation coefficient ϵ of optimized coil and conventional uniform coil.
Figure 4.27. Experimental results with different crack lengths $l_{\rm d}$: (a) 0 mm,(b) 6 mm, (c) 8 mm and (d) 12 mm.
Figure 4.28. Deformation coefficient ϵ as a function of crack length
Figure 4.29. Experimental results with different crack orientation α (a) 15°,(b) 30 °,(c) 45 °
Figure 4.30. (a) Contour plot obtained with threshold value set at 30% peak value for different crack orientation angles (b) deformation coefficient ϵ as a function of crack orientation angle
Figure 5.1. Magnetization curve for ferrimagnets and corresponding magnetic susceptibility
Figure 5.2. Cross-magnetization components <i>Mxy</i> and <i>Mzy</i> induced in an anisotropic medium by an applied magnetic field along the y-direction[92]69
Figure 5.3. Lateral view of the 3D model and geometry parameters72
Figure 5.4. Simulation result of anisotropic non-defect steel fastener with rotating current excitation. The permeability tensor: $\mu i = 2$, (a) $\mu H = -0.2$, (b) $\mu H = 0.2.73$
Figure 5.5. Deformation coefficient ϵ as a function of μH of anisotropic fastener74

Figure 5.6. Simulation result of anisotropic steel fastener with 12mm defect heading (a) 0 °, (b) 45 °, (c) 90 °, (d) 180 °. The fastener and the defect are marked by white line in the image
Figure 5.7. Simulation result: deformation coefficient ϵ of anisotropic fastener and 12mm defect as a function of defect orientation
Figure 5.8. DC current in an x direction coil to generate y direction DC magnetic field
Figure 5.9. Experimental results of healthy steel fastener with additional DC current (a) 0.25A, (b) -0.25A, (c) 0.5A, (d) -0.5A, (e) 1A, (f) -1 A, in the x direction coil77
Figure 5.10. Top view of the test sample showing it is rotated by θ in horizontal plane
Figure 5.11. Experiment results of steel fastener with 12mm defect. The sample was rotated relative to the geomagnetic field in horizontal plane (a) 0 °, (b) 45 °, (c) 135 °, (d) 180 °, (e) 225 °, (f) 315 °.
Figure 5.12. Experimental result: deformation coefficient ϵ of steel fastener and 12mm defect as a function of defect orientation80
Figure 5.13. Schematic diagram (a) and simplified model (b) of MBM method81
Figure 5.14. Numerical results of static (a) and AC 100Hz (b) outputs vs. input signal
Figure 5.15. (a) Transient response of the MR sensor output to step input signal. (b) Time domain signal of the MR sensor output with input sinusoid signal of 1V amplitude, 100 Hz frequency and 10V DC bias
Figure 5.16. Experimental setup for measuring magnetic field
Figure 5.17. Experimental results of output voltage vs. magnetic flux density87
Figure 5.18. Experimental setup: (a) Diagram of experiment system (b) Side view of test sample
Figure 5.19. Experimental results of defect free magnetized fastener ($ld=0$) obtained using GF708 to measure Bz directly (a) and using MBM method(b)90
Figure 5.20. Sensor DC bias when measuring the experiment results in Figure 5.19: (a) using the GMR sensor to measure the field directly; (b) using MBM method91
Figure 5.21. Experiment results of magnetized steel fastener with 12 mm defect ($ld = 12$: (a) GF708 measuring Bz directly and (b) MBM method91
Figure 6.1. Axial and circumferential channels for transmit and receive: (a) axial channels C01-A01 and C01-A16, circumferential channel C01-C03, (b) circumferential channels B01-B03 and B01-B15[103]96

Figure 6.2. 3D model of bobbin pickup and three windings inside the tube[104]97
Figure 6.3. (a) 3D diagram of the transceiver coils within a tube. (b) Circuit schematic of the 3 windings
Figure 6.4. (a) Axial direction line scan. (b) Top view of windings100
Figure 6.5. Simulation results: (a) real part and (b) imaginary part of probe output signal for ID flat-bottomed holes: diameter 3.2mm, depth 20%, 40%, 60%, and 80%, of tube wall
Figure 6.6. Peak value of the probe output signal amplitude vs. flat bottom hole depth.
Figure 6.7. Simulation signals obtained with defect located at different circumferential locations
Figure 6.8. Simulation results :probe output signal for varying defect depths for (a) 12mm long axial notch and (b) 60 °circumferential notch
Figure 6.9. Peak value of the probe output signal of axial and circumferential notches vs. defect depth
Figure 6.10. Simulation results: probe output signal for varying defect lengths for 0.8mm deep (a) axial notches, (b) circumferential notches
Figure 6.11. Simulation results: Lissajous Pattern seen when the defect circumferential location is varied from 0° to 45° (a) axial defect and (b) circumferential defect
Figure 6.12. Simulation results: normalized amplitude of probe output vs. Z-axis of varying exciting frequency for axial length 12 mm, depth 0.8mm (a) ID and (b) OD defects
Figure 6.13. Peak value of the probe output signal of ID and OD defects vs. frequency
Figure 6.14. 3D diagram of transceiver rotating field probe
Figure 6.15. (a) Schematic of the excitation system. (b) Constant current source circuit
Figure 6.16: Photo of transceiver rotating field probe for tube inspection107
Figure 6.17. Experimental results: probe output voltage,(a) real part and (b)imaginary part
Figure 6.18. Geometry dimensions of steam generator tube with machined notches.
Figure 6.19: Experimental results: amplitude of probe output as a function of probe location along the tube axis

Figure 6.20. Experiment results: Lissajous Pattern seen when the defect circumferential location is varied from 0 ° to 45 ° of (a) signals of axial notch (b) signals of circumferential notch
Figure 7.1. (a) Top view of RoC-GMR probe for riveted structure inspection. (2) 3D diagram of RoC-GMR probe for tube inspection
Figure 7.2. Lateral view of circumferential coil and tube wall
Figure 7.3. Simulation result of in-phase (a) and quadrature (b) component of circumferential eddy current density in a cross-section of tube wall
Figure 7.4. Top view (a) and lateral view (b) of axial coil
Figure 7.5. Simulation result of (a) real and (b) imaginary component of axial eddy current density, measured on z=0 plane
Figure 7.6. Simulation result of circumferential notch (7.7 mm×0.5 mm, 100% tube wall): (a) real component and (b) imaginary component
Figure 7.7. Simulation result of axial notch (12 mm×0.5 mm, 100% tube wall): (a) real component and (b) imaginary component
Figure 7.8. Simulation result of circumferential notch (7.7 mm×0.5 mm) with different depths: 1/8, 3/8, 5/8 and 7/8 of the tube wall from left to right. First row: Real component; Second row: imaginary component
Figure 7.9. Simulation results of circumferential notches with different depths: amplitude of RoC-GMR probe signal vs. circular distance along the circumferential direction at Z=0mm
Figure 7.10. Simulation results circumferential notches with different depths: Lissajous Pattern seen of real and imaginary component along the circumferential direction at Z=0mm
Figure 7.11. Simulation result of 50% tube wall OD circumferential notch length (a) 1mm, (b) 2.5mm, (c) 5mm × width 1mm
Figure 7.12. Simulation results of 50% tube wall OD circumferential notch with width 1mm and different length. Amplitude of RoC-GMR probe signal vs. circular distance along the circumferential direction at Z=0mm
Figure 7.13. Simulation results of 50% tube wall OD circumferential notch with width 1mm and different length. Lissajous Pattern seen of real and imaginary component along the circumferential direction at Z=0mm
Figure 7.14. Simulation result of 2mm diameter flat bottom hole, left-in-phase component; right -quadrature component
Figure 7.15. (a) Schematic of the prototype probe. (b) Schematic diagram of experimental system

Figure 7.16. Geometry dimensions of steam generator tube sample with machined notches
Figure 7.17. Experimental output images of RoC-GMR probe of OD axial notches. (a) $-$ (c) in phase (real) component for depths 60%,80%, and 100% of tube wall; (d) $-$ (f) quadrature (imaginary) component for depths 60%,80%, and 100% of tube wall125
Figure 7.18. Experimental output images of RoC-GMR probe of OD circumferential notches. (a) $-$ (c) in phase component for depths 60%,80%, and 100% of tube wall; (d) $-$ (f) quadrature component for depths 60%,80%, and 100% of tube wall125
Figure 7.19. Lissajous Pattern of the line scan along the axial direction through the defect center of the experimental data shown in Figure 7.17
Figure 7.20. Amplitude of <i>Br</i> along the axial direction through the defect center of the experimental data shown in Figure 7.17
Figure 7.21. Experimental result of 3mm diameter flat bottom hole: (a) in-phase component; (b) quadrature component

Chapter 1 Introduction

1.1 Introduction to Nondestructive Testing

The term "Nondestructive testing and evaluation" (NDT/NDE) refers to technologies that assess the structural integrity of a material or component without causing damage to the object under test[1]. NDT/NDE techniques are widely used in quality control, safety maintenance, and failure prevention in industry.

A variety of NDT techniques, employing different physical principles, have emerged over the years to inspect different materials. Each technique has certain advantages and limitations. Visual, radiographic, ultrasonic, and electromagnetic methods are four of the most commonly used approaches in NDE.

Radiographic testing is a NDT method of inspecting materials for hidden flaws by using short wavelength radiation to penetrate through materials. A penetrating radiation source, such as gamma rays or X-rays, travels through the object under test. The intensity of the beam energy after transmission is correlated with the material integrity. The energy distribution of the transmitted beam is imaged using imaging media. The density in a defect/crack region is generally lower than the rest of the sample, which produces intensity differences in the radiographic image[2].

Radiographic NDT is extensively applied to find internal defects. It can be used for both for metallic and non-metallic materials. The limitation of radiographic testing lies in its requirement of two-sided access to the component under examination. Moreover, the ionization of the radiation presents risks and also, the equipment is relatively expensive.

Ultrasonic testing utilize high frequency acoustic wave to test a material to detect changes in material properties[3]. The acoustic wave is transmitted, reflected and

scattered within the material under test. The interaction is captured by a transducer, and analyzed to determine the presence and location of flaws or discontinuities.

Ultrasonic NDT is widely used both for inspection metallic and non-metallic materials. A major limitation of ultrasonic testing is that most ultrasonic testing need a couplant to inject the acoustic wave efficiently into material. Furthermore, small and thin objects are difficult to be inspected.

In electromagnetic testing, the material under examination is excited electromagnetically and the interactive between the electromagnetic fields and the material are monitored and measured. The measured signals typically contain information about material anomalies that affect electrical conductivity, magnetic permeability or dielectric permittivity.

Electromagnetic NDT techniques cover a broad range of the electromagnetic spectrum. They have been used extensively in industry for flaw detection, microstructure characterization, and evaluation of mechanical properties.

The major advantages of Electromagnetic NDT are: non-contact, low-cost and high speed of inspection [4][5]. However, most of electromagnetic methods, e.g. eddy current method, are restricted to surface inspection and relatively thin conducting materials.

1.2 Introduction of Rotating Current/Field Probes

The probes discussed in this dissertation employ an electrically rotating eddy current to detect defects in the specimen. Although the probes have different applications; they employ analogous physical principles and offer similar advantages. The probes herein are mainly based on the following physical principles.

1.2.1 Rotating currents

Suppose there are two sinusoid exciting currents in different direction, as shown in Figure 1.1(a). The two exciting currents have identical frequency and different phase angle, as specified in equation 1.1 and 1.2.

$$I_1 = \hat{r}_1 I_1 \cos(\omega t + \varphi_1) \tag{1.1}$$

$$I_2 = \hat{r}_2 I_2 \cos(\omega t + \varphi_2) \tag{1.2}$$

where \hat{r}_1 \hat{r}_2 are the direction vectors of the currents, I_1 , I_2 the are amplitudes of the currents. ω is angular frequency, φ_1 , φ_1 are phase angle of the two exciting currents. If \hat{r}_1 \hat{r}_2 are not in line and $|\varphi_1 - \varphi_2| \neq n \cdot 180^\circ$, where n is any integer, then the induced current rotates in space and time, as shown in Figure 1.1(b), where the arrow indicates the spatial direction and the length of the line shows the current amplitude. If $\hat{r}_{1\perp}\hat{r}_2$, $\varphi_1 - \varphi_2 = (2n+1) \cdot 90^\circ$ and $I_1 = I_2$, the ellipse in Figure 1.1(b) becomes a circle.

The rotating eddy current is disturbed by defects in any orientation. Consequently, the most prominent advantage of using a rotating current excitation is that the probe is sensitive to defects of all orientations.

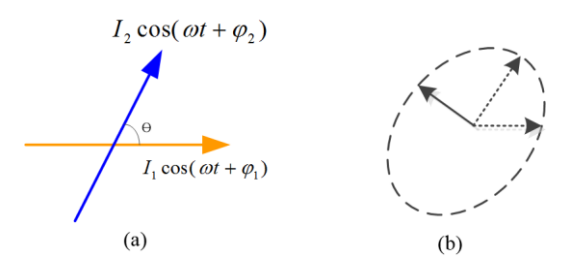


Figure 1.1. (a) Excitation currents with different orientation and phase angle. (b) Induced rotating eddy current in test sample.

1.2.2 Rotating fields

As shown in Figure 1.2(a), three phase windings(A,B,C) located 120° apart on the same physical axis that are driven by a three-phase sinusoidal constant current source whose frequency and amplitude are same generates rotating magnetic field. The

magnetic fields $(\boldsymbol{B}_a, \boldsymbol{B}_b, \boldsymbol{B}_c)$ generated by the three windings vary sinusoidally. The total magnetic field (\boldsymbol{B}) rotates in space with time. According to Maxell's equations, the induced eddy currents in the tube wall (\boldsymbol{J}_e) flows circularly around a radial axis and rotates together the total magnetic field in space, as shown in Figure 1.2(b).

The probe with rotating magnetic field offers detection capability comparable to those obtained with mechanically rotating coil probes but offer higher inspection speed and result in much lower wear and tear.

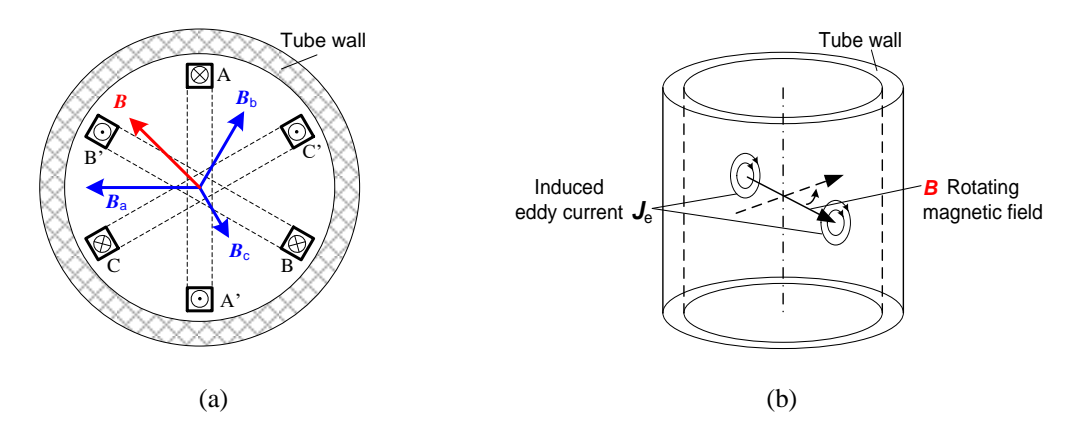


Figure 1.2. (a) Top view of probe current and magnetic field. (b) Induced eddy current in tube wall.

1.3 Statement of Problem

This research focuses on design and validation of novel eddy current probes for two applications, namely, i) detecting subsurface cracks under fastener heads in multi-layered riveted planar structures and ii) detecting defects in tube wall in steam generator tubes in power plants. The problems are introduced in this section.

1.3.1 Multi-layered Riveted Structure Inspection

Aeronautical components such as aircraft wings and riveted fuselage lap joints, undergo fatigue damage that occur around fasteners due to mechanical stresses[6]. Undetected cracks hidden at fastener sites in layered structures can lead to catastrophic failures. Therefore, reliable NDT methods are required to detect these embedded cracks.

A typical aircraft skin structure including fuselage skin or wing splice that is joined together by fasteners is shown schematically in Figure 1.3(a). Fasteners are typically made of aluminum, titanium or steel. This type of structure tends to produce high stress concentration around fastener holes. Hence, fatigue flaws, stress corrosion and cracks usually initiate at fastener sites in subsurface layers, as illustrated in Figure 1.3(b).

As acoustic waves cannot penetrate through the air gap between the layers, ultrasonic NDT is not suitable for this multilayer structure inspection. EC methods are widely used for detecting corrosion and subsurface fatigue cracks in riveted multilayer structures. Some of the challenges of multilayer structure inspection are: (1) Defects are embedded deep in the structure. (2) The fastener behaves as a strong discontinuity through the full depth of the layered structure, masking the response or indication due to small fatigue cracks. (3) The orientation of the cracks is arbitrary and unknown. (4) Edges of the multilayer structure pose additional difficulties in interpreting the measured signal.

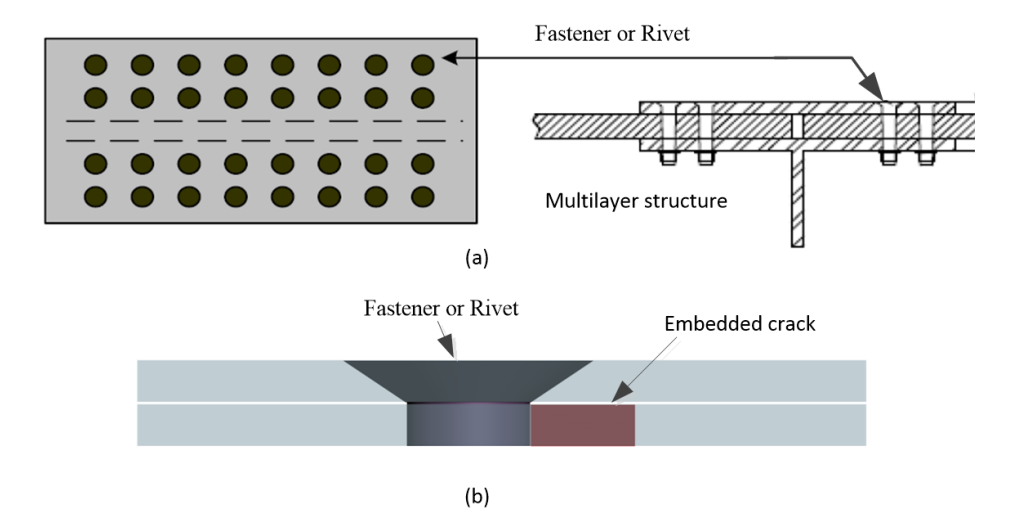


Figure 1.3. Layered structure:(a) Aircraft riveted skin structure geometry and(b) hidden crack at fastener sites

In order to obtain deeper penetration depth, lower excitation frequencies should be used since penetration depth is inversely proportional to the square root of the excitation frequency. However, in conventional eddy current probes where the change

in eddy current flow is measured using one or more detection coils[7]–[9], the drop in signal-to-noise ratio (SNR) observed at lower frequencies can present a challenge. This drawback can be overcome by using giant magnetoresistive (GMR) sensors to directly measure the magnetic field [10]–[13].

EC-GMR system with single, linear excitation coil has been presented by Nair et al. Yang et al use pulsed eddy current (PEC) along with GMR sensors for imaging fastener sites to detect subsurface defects. In these systems, the induced currents are primarily generated along a single direction in the test sample. When the crack is perpendicular to the induced currents, perturbation in the field caused by the defect produces a strong signal at the GMR sensor. However, when a crack is parallel to the EC flow, the perturbation is relatively small and one's ability to detect the defect decreases significantly[14]–[16].

In order to ensure the EC system is capable of detecting defects independent of their orientation, a design with rotating current excitation and one GMR sensor located at the center of the coils was presented by Yang et al. [15]. However, using a probe with a single sensor would require 2 dimensional raster scan is required which can be very time consuming especially in the case of large structure.

1.3.2 Steam Generator Tube Inspection

Steam generators serve as heat exchangers in nuclear power plants, as shown in Figure 1.4 schematically. They transfer heat from nuclear fission process on primary reactor side coolant to the secondary side clean water, which is converted to steam that drives the turbines for electric power production. These tubes constitute a barrier between primary and secondary sides and confine the radioactivity inside the primary coolant circuit. There are approximately 3000 to 16000 tubes inside a heat exchange tower. Inside of these tubes, there is high pressurized water with high temperature and

high fluid flow rate. The mechanical and chemical interaction of the water with these tubes can cause corrosion and crashes in tube wall[17]–[19].

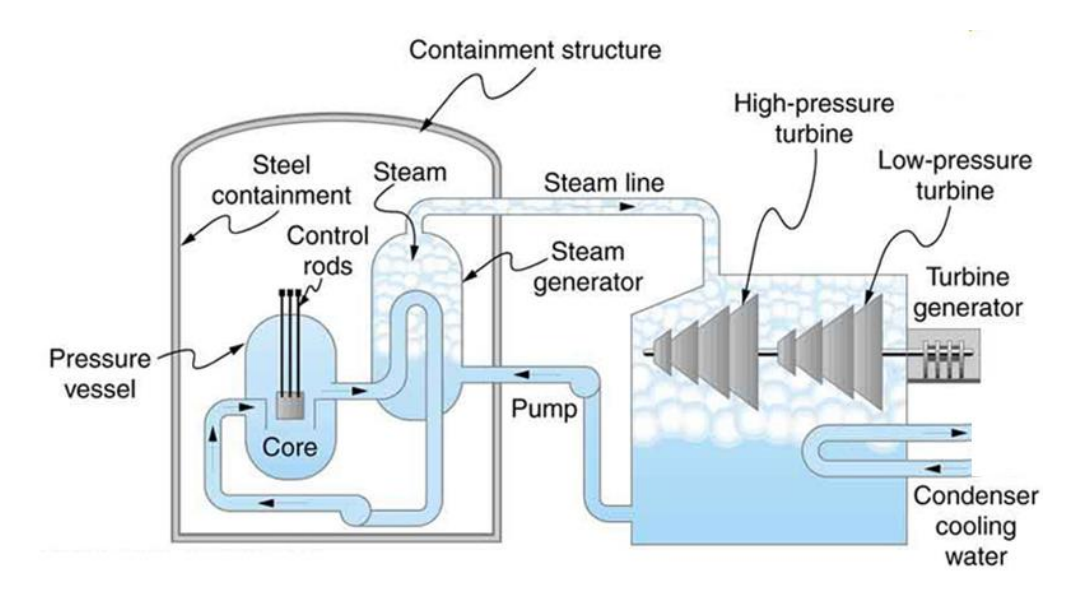


Figure 1.4. Schematic of a steam generator in nuclear power plant.

The deteriorating tubes are a potential safety problem. Periodic inspection and monitoring for timely detection and characterization of any degradation is a key element for ensuring safe operation of the plant.

Eddy current techniques are widely used in in-service inspection of steam generator tube in nuclear power plants. A variety of eddy current probes have been developed for the application[20]. Commercial probes such as bobbin coil probes (absolute and differential modes), rotating probe (Rotating Pancake Coils and Plus-Point), and array probes (X-Probe, Smart Array Probe and Intelligent Probe) have been used widely in industry. Bobbin coil probes, useful for fast initial detection of possible degradation, are not suitable for detecting circumferential defects around the tube, because the induced eddy currents are parallel to the crack orientation[21]. Rotating probes can provide a C-Scan image of tube wall with high resolution, and offer superior ability to characterize and size defects. Such probes are sensitive to circumferential defects, but the helical scanning process is time-consuming, prone to probe wear and the

mechanical control system for rotation is complex and susceptible to failure. Array probes are capable of providing information relating to the angular location of defects. The advantages associated with the use of these probes include high inspection speed and resolution, but they need sophisticated excitation and post-processing schemes. The signal is also contaminated by noise introduced as a consequence of probe vibration[22], [23].

1.4 Research Objectives

Based on the problems stated in section 1.3, the research objectives of this dissertation are as follows.

- (1) Design, analyze, optimize and develop novel rotating current EC-GMR (RoC-GMR) sensor system to detect cracks buried around fastener sites in layered structures. The research should analyze propose solutions to following issues:
 - sensitive to cracks of all orientations emanating radially from fastener;
 - detectable of defect embedded deep in subsurface layers;
 - utilize linear array sensors to increase inspection speed;
 - eliminate effect of remanence magnetic of steel fasteners and keep the operation point of the GMR sensor constant;
 - effect of earth's magnetic field on weak magnetic field measurements using GMR sensors.
- (2) Design analyze, optimize and develop electrically rotating field eddy current probes for steam generator tube inspection. In addition to the rotating field probe, develop a rotating current EC-GMR (RoC-GMR) probe for tube inspection. The probes should have following advantages.
 - Sensitivity to all orientation defects;
 - simple in structure and operation;

- eliminate mechanical rotation and;
- high operation speed.

1.5 Methodologies

To achieve the research objectives, three-dimensional finite element simulation models are used to mimic the underlying physical process, to assess the feasibility of proposed design and also optimize the design parameters. Prototypes are designed, built, and tested. Experimental data using the prototypes on test samples is obtained and analyzed. Experiment results validate the numerical simulation models and further demonstrate the feasibility of the proposed approach.

1.6 Organization of This Thesis

The research conducted in this thesis along with simulation and experiment results are organized as following. Chapter 2 presents review of electromagnetic NDE. Chapter 3 introduces EC-GMR probe for multi-layer riveted structure inspection and analyzes the issues of RoC-GMR probe with array sensors. In chapter 4, differential measurement method is introduced to subtract the strong background field in fly during scan and an optimized non-uniform distributed rotating current excitation coil design is presented to generate uniform exciting field in the sensor region. Chapter 5 analyzes challenges of inspection defect under steel faster. The effect of magnetic anisotropy of steel fastener is discussed. Magnetic balance measurement method is proposed to make MR sensor's bias point constant and extend linear measure range of the GMR sensor. Chapter 6 presents novel transceiver RoF-EC probe for steam generate tube inspection. Novel RoC-GMR probe for tube inspection is proposed in chapter 7. Conclusions and recommendations for future research are summarized in Chapter 8.

Chapter 2 Review of Electromagnetic NDE

2.1 Electromagnetic NDE techniques

Electromagnetic methods of NDE comprise a full spectrum of techniques ranging from static (DC) methods to high frequency (10THz) methods. The principles of electromagnetic NDE are introduced briefly in this chapter.

2.1.1 Static Electromagnetic Methods

Static electromagnetic technologies use DC magnetic or electric field to assess the integrity of materials. Magnetic flux leakage (MFL) and electrical impedance tomography (EIT) are the two most common static electromagnetic methods.

2.1.1.1 Magnetic Flux Leakage Method

In MFL testing, permanent magnets or DC electromagnets are used to generate a strong magnetic field to magnetize the specimen. The magnetic flux lines are coupled into the specimen using metal 'brushes' or air coupling. Where the object has no flaws, the magnetic flux will largely remain with the specimen. If there is defect present in the specimen, then there is magnetic flux leakage around the defect. Magnetic field measuring sensors such as Hall sensors are used to measure different components of the leakage flux.

The MFL method has been largely used for inspection of ferromagnetic structural components in petrochemical, rail, energy and metal industries. MFL techniques are effective in detecting corrosion or surface transverse defects, but have low sensitivity to defect fissures run parallel to the magnetic flux lines. MFL is also adversely affected by increasing inspection speed.

2.1.1.2 Electrical Impedance Tomography (EIT)

EIT measures the electrical conductivity and permittivity inside a body or structure, given simultaneous measurements of electrical currents and potentials at the boundary[24].

Medical imaging using EIT has gained a lot of attention in imaging applications [25]. Typically, conducting surface electrodes are attached to the skin around the part of the body being examined. Small alternating currents are applied to each of a circular array of electrodes; the resulting equi-potentials are recorded from the other electrodes. This process is then repeated for each electrode in the array and the resulting measurements are used in image reconstruction algorithms to get a tomogram [26]. EIT is still under development for nondestructive evaluation purposes. Stacey *et al.* at Stanford University published a technical report in 2006 on 3D EIT imaging[27].

2.1.2 Low Frequency Methods

Low frequency quasi-static methods cover the frequency range from 10Hz to 10MHz.

They are generally referred to as Eddy Current testing (ECT) methods.

2.1.2.1 Conventional Eddy Current Method

Eddy current testing is based on electromagnetic induction. When a coil carrying alternating current is brought close to a metallic specimen, the changing magnetic field (primary field) associated with the alternating current induces eddy current in the specimen. The secondary magnetic field associated with the eddy current opposes the primary magnetic field. Defects in the specimen perturb the eddy current flow.

In conventional eddy current testing, changes in coil impedance are measured as the signal. Defect is characterized from the amplitude and phase variations of coil

impedance. It should be noted that the defect must interrupt the eddy current flow to be detected, and defect lying parallel to the current path will not cause significant interruption and may not be detected [28]. Advantages and Disadvantages of eddy current testing are as follows:

Advantages:

- Non-contact method
- High inspection speeds
- High detectability
- Gives good discrimination
- Easy to automate
- Easy to learn and quick to use
- Economical
- Environmentally friendly

Disadvantages:

- Only applicable for conductive materials
- Sensitive to defects near the surface
- Presence of noise due to factors such as probe lift-off, surface roughness and variations of electromagnetic characteristics of test material

Typical applications of eddy current technologies include:

- Surface and near-surface flaw detection
- Measurement of non-conductive and conductive coating thickness, and detect defects, which are under insulating coatings
- Sort material with different values of conductivity and permeability

2.1.2.2 ECT with Magnetic Field Measurement Method

In conventional eddy current testing, coils are used to pick up the signal which is based on Faraday's law of electromagnetic induction, in which case the intensity of the induced signal is positively correlated with the value of frequency. The signal amplitude drops rapidly as frequency decreases. As a result, signal-to-noise ratio (SNR) observed at lower frequencies can present a challenge. This drawback can be overcome by using sensors with high sensitivity to directly measure the magnetic field associated with the eddy current.

Associated with the current induced in the sample is a magnetic field which will be disturbed in the presence of a defect[29]. The changes in magnetic field are measured as an indication of the presence of defect. As the magnetic field is a complex three-dimensional field, it is possible to measure components of the field that are indicative of the nature of the disturbance and which may be related to the physical properties of any cracks present. Figure 2.1 presents an example, which is a plan view of a surface-breaking crack where a uniform current is flowing[30]. The field component denoted by Bz corresponds to the poles generated as the current flows around the ends of the crack. These responses are principally at the crack ends and are indicative of a crack length. The field component denoted by Bx corresponds to the reduction in current surface density as the current flows down the crack and is indicative of the depth of the defects.

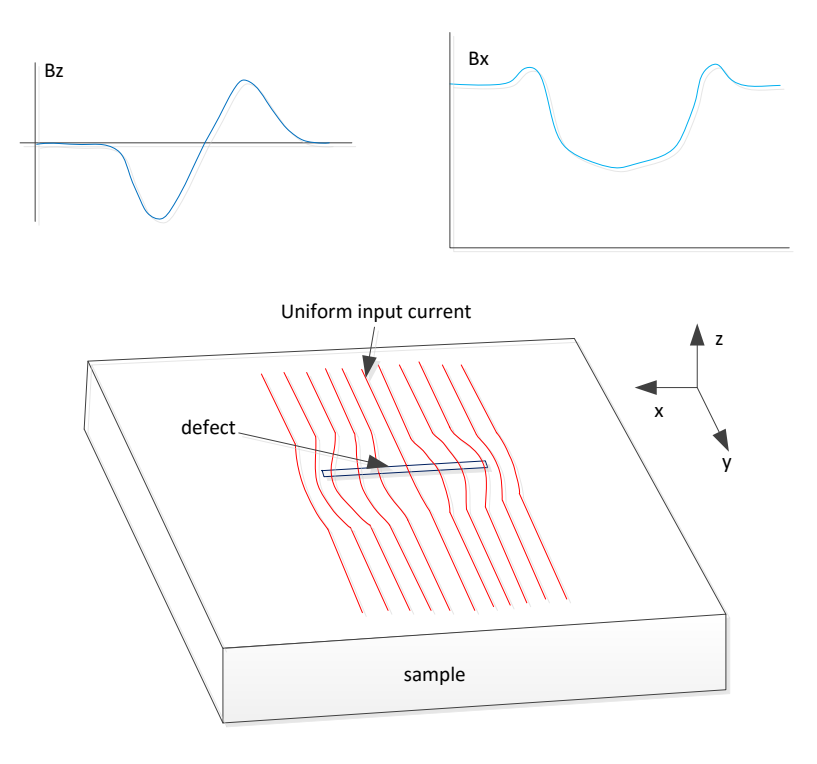


Figure 2.1.Detection principle of current field measurement method.

2.1.3 High Frequency Methods

2.1.3.1 Microwave NDE

The term microwave is used to denote all electromagnetic radiation waves whose frequencies lie between 0.3 and 300 GHz. These frequencies correspond to a range of free space wavelengths in vacuum from of 1m to 1mm. Microwaves propagate readily through most nonmetallic materials. In contrast, microwave reflects almost completely from metal surfaces, penetrating only microscopic distances below the surface[31], [32].

Microwave NDE technique is well-suited for testing dielectric materials and composites because microwave signals can easily penetrate low-loss dielectric materials, such as glass-fiber reinforced polymer skins, foam and honeycomb structures without suffering significant signal attenuation. Typically a dielectric test object is irradiated by microwave energy from an antenna; the field travels through the sample and is received by a receiving antenna. The phase difference between the

incident and the received signal is directly related to the slab thickness and permittivity ε_r , which is in general a complex parameter:

$$\varepsilon_r = \varepsilon_r' - j\varepsilon_r'' \tag{2.1}$$

Microwave NDE sensors usually operate in one of two basic modes: far-field or near-field. Far field information is simpler to interpret than near field measurements. However, the spatial resolution of the far-field technique is proportional to the operational wavelength. The spatial resolution of the near field mode is generally better than that of the far field mode. The disadvantage of the near field mode is that the standoff distance has to be maintained relatively close to the sample, making it more difficult to implement.

2.1.3.2 Terahertz Tomography

Terahertz (THz) technology covers the part of electromagnetic spectrum between 0.1 to 10 THz. Terahertz technology has been undergoing significant progress on the scientific front during the past two decades[33]–[38]. The terms "far infrared" (FIR) or "sub-millimeter waves" (sub-mm) were used earlier instead of the relatively new term "terahertz" [39].

Terahertz waves offer some unique features that make them attractive for applications in non-destructive evaluation (NDE). For instance, THz waves can penetrate most materials, like microwaves, but offer a much better spatial resolution than microwaves that makes them more suitable for imaging and millimeter or sub-millimeter size features. THz waves are safe for human operators because they are non-ionizing, and, finally, THz systems operate in a non-contact manner.

Due to the high costs of terahertz emitters and receivers, the raster scan method is still standard in terahertz applications. The slow raster scan of most terahertz systems for large parts is still a significant drawback in comparison to other non-destructive methods. The use of antennae arrays could solve this problem. Cameras based on micro-bolometer arrays are being developed by groups at NEC (Japan) and CEA-Leti (France), which have produced cameras with enough sensitivity to image the THz beam generated by photo-conductive antennas [40], [41]. Improvement of sensitivity and minimization of interference effects make the application and deployment of this technology for NDE more feasible.

2.1.4 Time Domain Measurement Methods

2.1.4.1 Pulsed Eddy Current

Pulsed excitation produces transient signals with a wide range of frequency components and hence it contains more information compared to single frequency excitation[42] [43].

Similar to ultrasonic testing where the measured time of flight in the received signal can determine a defect's depth, eddy current pulse propagation through the material and shape of the transient response signal are related to discontinuities at different depths. The transient signal parameters and features allow flaw discrimination and characterization in the time domain. Figure 2.2 shows some experiment results of using PEC to test multilayer sample[42]. Some common features in transient characteristics of PEC signals are the peak amplitude, time to peak amplitude and time to zero crossing. The peak amplitude is used to determine the defect size. The time to zero crossing is popularly used to find the depth of a flaw, and the time to peak amplitude is used to identify the defect depth or material thickness.

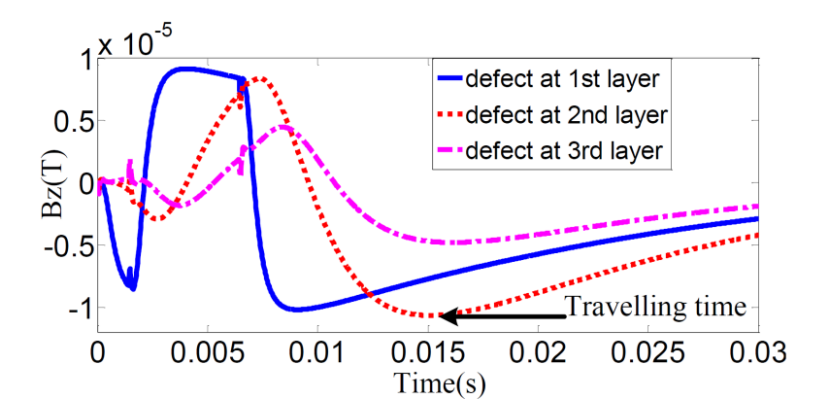


Figure 2.2. Transient response associated with defects at different depth[42].

One can generate PEC C-scan imaging based on characteristics of the transient response. Since an A-scan measurement refers to the transient response at a single position, the mapping of a feature of each A-scan onto the probe position allows the construction of a C-scan feature image. Any time-dependent feature representing the dissipation of transient field associated with different depths can be employed to produce the C-scan image. Therefore, the image produced contains information about the surface, near surface and subsurface [44].

The time interval between successive transient waveforms must be sufficient to allow measurement of each transient response until it decays to zero. Since the diffusion velocity of the EC signal is heavily dependent upon the material, the transient response duration due to one pulse is also material dependent. Also, the transient response duration increases with the thickness of a specimen under test[43], [45].

2.1.4.2 Time-domain Reflectometry

Time domain reflectometry (TDR) is a term used to describe a technique of observing the time dependent response of a sample after application of a time dependent electromagnetic field. The response characteristic, whether measured as a current, charge, or other related observable quantity, is a real valued a function of real time[46][47].

In most TDR system, a train of suitable input signal is applied to a transmission line, usually coaxial with 50Ω characteristic impendence, and the waveform in the line is observed at some point by a probe. As indicated in Figure 2.3, a sample is either inserted or attached to the line with some form of termination. The resultant changes of the transient waveforms is measured to characterize the properties of the sample[48].

There are 4 common modes of operation.

- (1) reflected waveform from the sample in the line terminated by a matched section of 50Ω impedance for no reflection of the transmitted wave;
- (2) reflected waveform from a sample used as the termination, i.e. with an open circuit and no current after the sample section;
- (3) reflected waveform from a short-circuited sample, with no potential difference at the terminal end;
- (4) transmitted waveform in the section of line behind the sample, terminated by 50Ω to eliminate reflections from the end of the line.

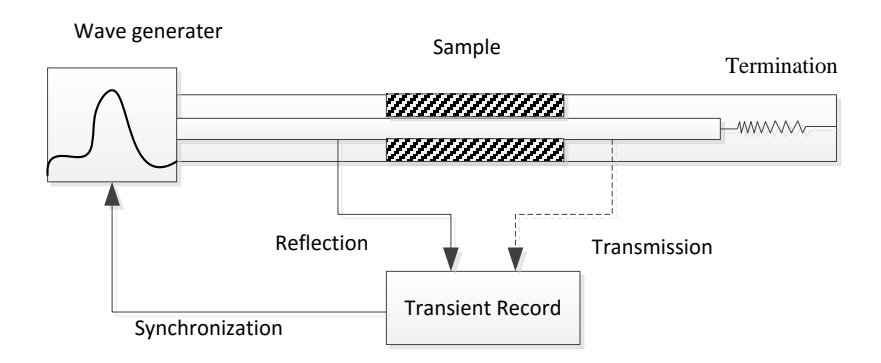


Figure 2.3. Schematic diagram of instrumentation for time domain measurement.

2.2 Formulation of Eddy Current Problem

A typical eddy current problem consists of a conducting region Ω_1 with nonzero conductivity and a surrounding non-conducting region Ω_2 free of eddy currents which may contain source currents J_s , as shown in Figure 2.4.

Where,

 J_s : excitation source current density.

 σ : conductivity of the conducting region.

 $\boldsymbol{\Omega}_{\!\scriptscriptstyle I}$: conducting region with nonzero conductivity.

 Ω_2 : non-conducting region, contains source current, free of eddy current.

 S_{12} : interface between Ω_1 and Ω_2 .

 S_B : boundary, norm component of magnetic flux density is prescribed.

 S_H : boundary, tangential component of magnetic field intensity is given.

n: the outer normal on the boundaries S_B and S_H .

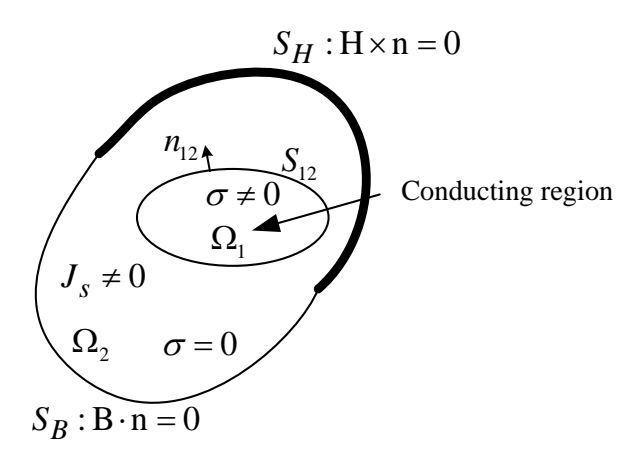


Figure 2.4. Typical eddy current problem

2.2.1 Maxwell Equation in Eddy Current Problem

In eddy current problems the objective is to solve for the magnetic flux density, magnetic field intensity and the induced eddy current in the solution domain for a specific geometry, source current distribution and the material properties such as permeability and conductivity that are prescribed.

Since $\omega \varepsilon \ll \sigma$ is always satisfied due to low frequency fields in eddy current problem, the displacement current is neglected and the Maxwell equation is written as:

$$\nabla \times \mathbf{H} = \sigma \mathbf{E} \qquad (a)$$

$$\nabla \times \mathbf{E} = -j\omega \mathbf{B} \qquad (b)$$

$$\nabla \cdot \mathbf{B} = 0 \qquad (c)$$
2.2

$$\nabla \times \mathbf{H} = \mathbf{J}_{s} \qquad (a) \\
\nabla \cdot \mathbf{B} \qquad (b) \qquad \text{in } \Omega_{2} \qquad 2.3$$

$$\mathbf{B} \cdot n = 0 \quad \text{on } S_B$$
 2.4

$$\mathbf{H} \times n = 0 \quad \text{on } S_H$$
 2.5

$$\begin{array}{ll}
\mathbf{B}_{1} \cdot n_{12} = \mathbf{B}_{2} \cdot n_{12} & (a) \\
\mathbf{H}_{1} \times n_{12} = \mathbf{H}_{2} \times n_{12} & (b)
\end{array} \quad \text{on} \quad S_{12}$$
2.6

where, the subscripts 1 and 2 refer to quantities in regions Ω_1 and Ω_2 respectively. Boundary conditions are the continuity of normal component of flux density and tangential component of magnetic field intensity.

2.2.2 Formulations - Magnetic Vector Potential

Assume magnetic vector potential is represented by ${\bf A}$ and electrical scalar potential by ${\bf V}[49]$, then

$$\mathbf{B} = \nabla \times \mathbf{A}$$
 2.7

$$\mathbf{H} = \nu \nabla \times \mathbf{A}$$
 2.8

$$\nabla \times \mathbf{E} = -j\omega \mathbf{B}$$
 2.9

$$\nabla \times (\mathbf{E} + j\omega \mathbf{A}) = 0 \tag{2.10}$$

$$\mathbf{E} = -j\omega\mathbf{A} - \nabla\mathbf{V} \tag{2.11}$$

where ν is the reluctance. The magnetic vector potential reduces the number of unknowns to be solved compared with the method to solve the magnetic and electric field components directly. So the governing equations for 3D eddy current problem is represented by

$$\nabla \times (\nu \nabla \times \mathbf{A}) + j\omega \sigma \mathbf{A} + \sigma \nabla \mathbf{V} = 0 \qquad \text{in } \Omega_1$$
2.12

$$\nabla \times (\nu \nabla \times \mathbf{A}) = \mathbf{J}_{s} \qquad \text{in } \Omega_{2}$$

$$n \cdot (\nabla \times \mathbf{A}) = 0$$
 on S_B

$$(\nu \nabla \times \mathbf{A}) \times n = 0$$
 on S_H 2.15

$$\begin{array}{ll}
n_{12} \cdot \nabla \times \mathbf{A}_1 = n_{12} \cdot \nabla \times \mathbf{A}_2 & (a) \\
(\nu_1 \nabla \times \mathbf{A}_1) \times n_{12} = (\nu_2 \nabla \times \mathbf{A}_2) \times n_{12} & (b)
\end{array} \quad \text{on } S_{12}$$

$$2.16$$

Since $\nabla \cdot (\nabla \times \mathbf{A}) = 0$ is always satisfied, this ensures that we have $\nabla \cdot \mathbf{B} = 0$. To simplify the programming, the governing equation is merged into one equation:

$$\nabla \times (\nu \nabla \times \mathbf{A}) - \nabla (\nu \nabla \cdot \mathbf{A}) + j\omega \sigma \mathbf{A} + \sigma \nabla \mathbf{V} - \mathbf{J_s} = 0 \qquad \text{in } \Omega: \Omega_1 + \Omega_2 \quad 2.17$$

$$\nabla \cdot (-j\omega\sigma \mathbf{A} - \sigma\nabla \mathbf{V}) = 0 \qquad \text{in } \Omega_1$$

The A, V - A method has stable numerical solution for harmonic quasi-static magnetic field because of the uniqueness of A and V. The method is applied for multiply connected conducting regions. The model for the source current is convenient and easy. It has high computation precision. The disadvantage is that total unknowns are big number.

2.2.3 Reduced Magnetic Vector Potential

In order to decouple the magnetic field due to induced eddy current from the field due the excitation source current, the total magnetic vector potential **A** is decomposed into

 A_s and A_r , where A_s is the magnetic vector potential due to excitation source current in free space and A_r is the magnetic vector potential due to induced current in the conductor, respectively. The total magnetic flux density **B** is the summation of the corresponding terms B_s and B_r and similarly, the magnetic field intensity H is expressed in terms of source and induced components [50], [51].

Then the governing equation is derived from the A,V - A method by substituting A by A_s and A_r as

$$\nabla \times v \nabla \times \mathbf{A}_r - \nabla v \nabla \cdot \mathbf{A}_r + j \omega \sigma \mathbf{A}_r + \sigma \nabla \mathbf{V} = (1 - v_r) \nabla \times \mathbf{H}_s - j \omega \sigma \mathbf{A}_s$$
2.19

$$\nabla \cdot (-j\omega\sigma \mathbf{A_r} - \sigma\nabla \mathbf{V}) = \nabla \cdot (j\omega\sigma \mathbf{A_s})$$
2.20

where v_0 is the reluctance in free space and v_r is the relative reluctance of the conductor. All the variables on the left hand side of equation is independent of excitation source, and only rely on induced current in the conduction region. This implies that there is no need to re-generate the mesh for the exciting coils at different scan positions during inspection. The A_s and H_s on the right hand side of the equation is calculated analytical with highly reduction of computation time. The modeling is easier to simulate the probe scanning than magnetic vector potential formulations, since there is no need to re-mesh the probe at different scan position.

2.2.4 Penetration Depth

Considering Maxwell's equations:

$$\nabla \times \mathbf{H} = j\omega(\varepsilon - j(\frac{\sigma}{\omega}))\mathbf{E}$$
2.21

$$\nabla \times \mathbf{E} = -j\omega \mu \mathbf{H}$$
 2.22

where , μ , σ are the permittivity, permeability and conductivity of the medial, ω is angular frequency.

Taking the curl of Equation 2.22 and then substituting in Equation 2.21 gives the vector wave equation:

$$\nabla \times \nabla \times \mathbf{E} - \mathbf{k}^2 \mathbf{E} = 0 \tag{2.23}$$

Planes waves are the simplest (1D) solution of Maxwell's equations in a homogeneous region of space. A plane wave is an electromagnetic field having the form:

$$\mathbf{E} = \mathbf{E}_0 e^{-\mathbf{j}(k_x x + k_y y + k_z z)}$$
 2.24

where E_0 is constant vector, k_x , k_y , k_z are complex constants that define a wavenumber k.

$$\mathbf{k} = \beta - j\alpha = \omega \sqrt{\mu(\varepsilon - j(\frac{\sigma}{\omega}))}$$
 2.25

The real and imaginary parts of the wavenumber vector \mathbf{k} define the phase $\boldsymbol{\beta}$ and an attenuation $\boldsymbol{\alpha}$.

For a lossy medium, the plane wave decays as it propagates. The depth of penetration (δ) is defined as the distance required to reduce the field level by a factor of $e \approx 2.71828$, so that the field is 36.788 % of the surface value. The depth of penetration is given as:

$$\delta = \frac{1}{\alpha}$$
 2.26

In eddy current problem, penetration depth is a measure of how deep eddy current can penetrate into a material. As shown in Figure 2.5, the density of induced eddy current decreases exponentially from the surface with depth into the specimen. It depends on the testing frequency, as well as test specimen variables such as electrical conductivity and permeability. For most eddy current problem, the penetration depth is estimated using Equation 2.27.

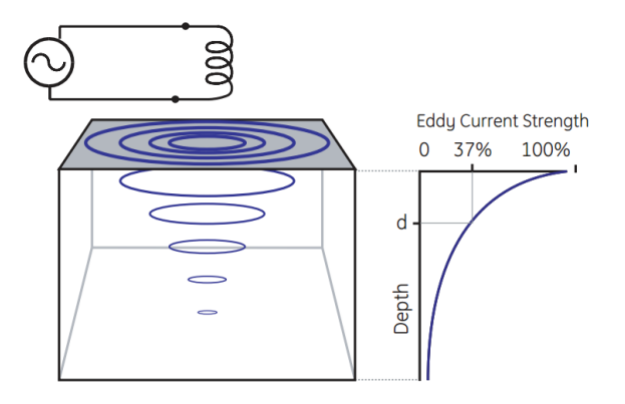


Figure 2.5. Penetration depth of eddy current.

$$\delta = \frac{1}{\sqrt{\pi f \,\mu \sigma}}$$
 2.27

Where,

f: excitation frequency;

 μ : conducting material permeability;

 σ : conducting material conductivity;

Skin depth is a critical parameter for selecting excitation frequency for a given test specimen. Low frequency corresponds to larger skin depth. Each frequency is sensitive to a certain depth of test sample.

2.3 Magnetic Sensors in NDE

Magnetic field measuring methods for NDE have been in use for more than forty years. Magnetic field is measured using a variety of different technologies. Each technique has unique properties that make it more suitable for particular applications. This chapter concentrates on sensors that are commonly used in magnetic field measuring instruments in NDE.

2.3.1 Comparison of Magnetic Sensors

Characteristics of different magnetic field sensors are listed in Table 2.1[52]. The operation principles and applications in NDE of the sensors listed in Table 2.1 are briefly introduced next.

Table 2.1. Magnetic field sensor characteristics.

Sensor type	Range (mT)	Resolution (nT)	Bandwidth (Hz)	Comment
Induction coil	variable	variable	1 to 106	Cannot measure static fields, low sensitivity to low frequency field
Fluxgate	10-4 to 0.5	0.1	DC to 103	Bulky volume, high power consumption
SQUID	10-9 to 0.1	10-4	DC to 5	Highest sensitivity, expensive
Hall effect	10-2 to 104	100	DC to 108	
Magnetoresistance	10 ⁻³ to 5	10	DC to 10 ⁷	Good for mid-range application
Magnetooptic	0.06 to 600	5×10^{-2}	DC to 10	

Induction coil is one of the simplest magnetic field sensing devices. The operation principle of induction coil is based on Faraday's law, which states that if a loop of wire is subjected to a changing magnetic flux, φ , through the area enclosed by the loop, then a voltage will be induced in the loop that is proportional to the rate of change of the flux, as indicated in equation 2.28.

$$e = -N\frac{d\varphi}{dt}$$
 2.28

where e is the output voltage of the coil, N is the number of turns of the coil. In conventional eddy current testing, induction coil is widely used to pick-up signal. The main limitation of the coil sensor is that the induced signal is proportional to the rate of change of flux, and hence will have very low signal to noise ratio at low frequency. Fluxgate is a transducer that converts a magnetic field into an electric voltage. A comprehensive explanation of the fluxgate principle and the different fluxgate configurations is given by Lenz et al.[53]. The fluxgate magnetometers are the most

widely used measuring instruments. They are reliable and relatively less expensive than the other magnetic field measuring instruments.

Third, superconducting quantum interface device (SQUID) is introduced. SQUID is an extremely sensitive magnetic flux-to-voltage transducer [54][55]. A SQUID is based on superconducting loops containing Josephson junctions. The advantages of the SQUID for NDE include high sensitivity, broad dynamic range (>80 dB), and its intrinsically quantitative nature. The ability of SQUIDs to function down to zero frequency allows them to sense much deeper flaws than other sensors, to detect and monitor the flow of steady state corrosion currents, and to image the static magnetization of paramagnetic materials. The wide dynamic range and quantitative nature enables the SQUID to maintain its high sensitivity in the presence of strong dc or noise fields. However, SQUID is extremely expensive as compared to other methods, as low temperature is required for superconductivity. Moving a SQUID-based device is not straightforward. The main difficulties arise from the nature of the SQUID operation and from degradation in the SQUID's noise performance when it is cooled and moved in the Earth's magnetic field.

Hall sensor is widely used in NDE. The Hall Effect device is the oldest and most commonly used magnetic field sensor[56]. The Hall effect is a consequence of the Lorentz force law, which was discovered by Edwin H.Hall in 1897. Three axis hall sensors are housed in a very small package. These devices are most effective for measuring flux densities ranging from 5×10^{-5} to 30T.

The Magnetoresistive (MR) sensors cover the middle ground between the low and high field sensors. Magnetoresistance is the property of a material where the value of its electrical resistance changes when an external magnetic field is applied to it. The effect was first discovered by William Thomson in 1851, but he was unable to lower

the electrical resistance by more than 5%. This effect was later called Anisotropic magnetoresistance (AMR). More recent research has resulted in materials and multilayer devices showing giant magnetoresistance (GMR), colossal magnetoresistance (CMR), tunnelling magnetoresistance (TMR) and extraordinary magnetoresistance (EMR). Generally, resistance can depend both on magnetization magnitude and on magnetic field direction.

The magneto-optical sensors (MO-sensors) are based on the Faraday-effect instead of electrical effects to analyze magnetic fields. Magneto-optical sensors are based on the Faraday-effect discovered in 1845 by Michael Faraday, where polarization angle of light passing through a transparent medium in the presence of external magnetic is rotated in proportion to the magnetic field. This discovery was the first indication of interaction between light and magnetism[57]. Magnetooptic imaging (MOI) was proposed as a possible solution for thick structure inspection[33]. MO-sensors have the technical benefit of producing real time analog image of the magnetic field. Thus, real-time investigations of the magnet field distribution is performed without the need for time-consuming, point-to-point scans, such as that required using Hall sensors or MR sensors. The primary disadvantage of this technique is the lack of a quantitative measure of the field.

2.3.2 GMR Sensor

Giant magnetoresistance (GMR) sensor, a kind of magnetoresistive sensor, is used in this research. GMR is based on the quantum mechanical magnetoresistance effect observed in thin-film structures composed of alternating ferromagnetic and non-magnetic conductive layers. A significant change in the electrical resistance is observed depending on whether the magnetization of adjacent ferromagnetic layers is in parallel or an antiparallel alignment.

In the absence of an applied field, the resistivity of the GMR element is high due to scattering between oppositely polarized electrons in the anti-ferromagnetically coupled multi-layers of the device. An external field aligns the magnetic moments of the ferromagnetic layers, eliminating this scattering mechanism and thereby reducing the resistivity of the material.

The use of giant magnetoresistive (GMR) sensors for electromagnetic nondestructive evaluation has grown considerably in the last few years. Technological advances and development of giant magnetoresistive materials has led to commercially available GMR sensors with many qualities well suited for electromagnetic NDE. Low cost GMR magnetometers are now available which are highly sensitive to the magnitude of the external magnetic field, have a small package size, consume little power, and operate at room temperature. Incorporation of these sensors into electromagnetic NDE probes has widened the application of these sensors. In particular, since GMR sensors respond to the magnitude of the external field instead of the time rate of change of the field and therefore do not lose sensitivity at low frequencies. The low frequency sensitivity of the devices provides a practical means to perform electromagnetic inspections on thick layered conducting structures [59][60][12][61].

Chapter 3 Introduction of EC-GMR Probe for Multilayer Structure Inspection

3.1 Single Excitation Coil

This section describes a probe comprising eddy current excitation with GMR sensor for measuring the fileds associated with induced currents. A schematic of EC-GMR probe with single, planar excitation coil is shown in Figure 3.1 [62]–[66]. The coil is driven by a current and acts like a current sheet. Eddy current is induced in the test sample. As indicated in chapter 2, the penetration depth of eddy current is inversely proportional to the square root of the excitation frequency. This suggests the use of low excitation frequencies to obtain deep penetration. However, the drop in signal-tonoise ratio (SNR) observed at low frequencies using conventional coil to pick up signal can present a challenge. This drawback is overcome by using highly sensitive GMR sensors to measure the magnetic field directly. Array GMR sensors are located on the symmetry line of the linear excitation coil to measure the normal component of the magnetic field. When the probe is placed on top of defect free sample, the excitation current and induced eddy current are such that the normal component magnetic field at the symmetry line is zero resulting in zero output of the sensor array. When defect is perpendicular to EC flow, a perturbation in the current flow produces a normal magnetic field near the defect, causing the GMR sensors to produce a strong signal.

In the EC-GMR probe in Figure 3.1, the current is linear and the probe is very sensitive to cracks that are perpendicular to current direction. When a crack is parallel to the EC flow, the perturbation is relatively small and the ability to detect the defect

decreases significantly, as shown in Figure 3.2(c)[67]. The single coil probe is not sensitive to defect along the current direction. There is a need for a new probe that addresses this problem.

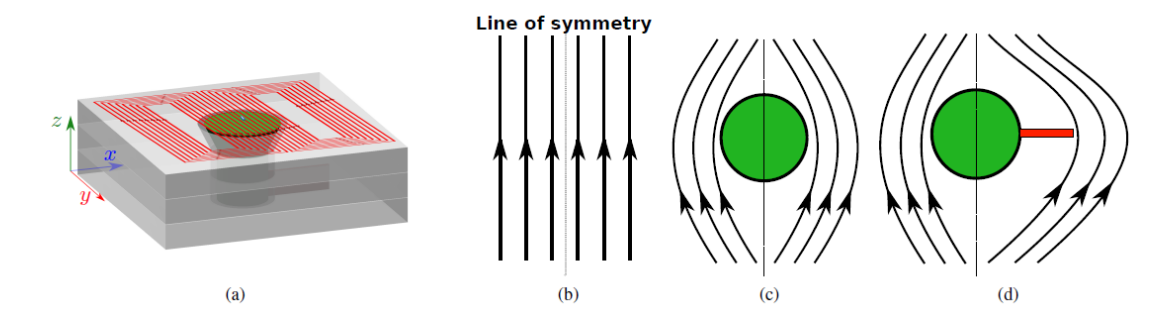


Figure 3.1. (a) A unidirectional coil with a GMR sensor array at the coil symmetry line for inspecting a layered riveted plate. (b),(c), (d) Induced eddy currents when there is no discontinuity, fastener, and fastener with a defect, respectively[68].

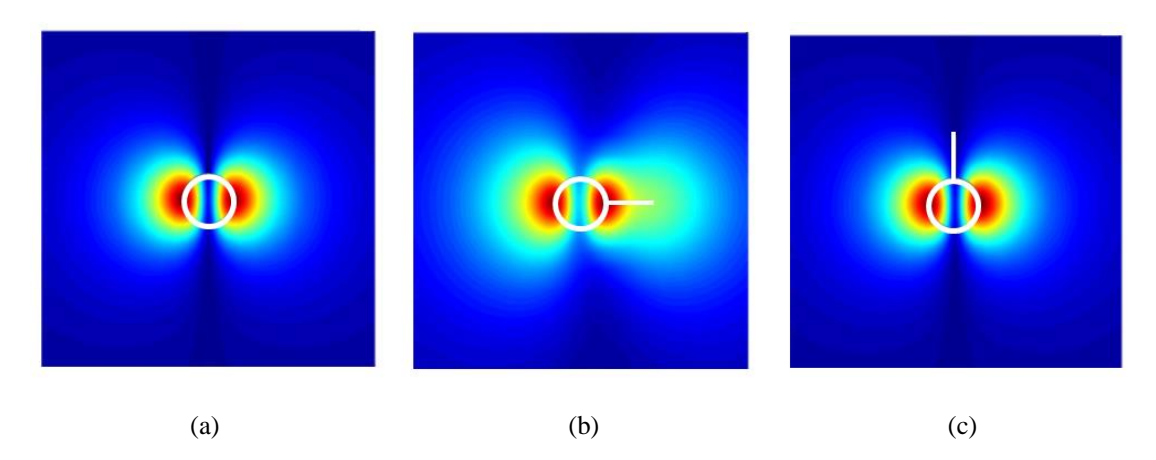


Figure 3.2. Simulation results of a unidirectional coil with a GMR sensor array at the coil symmetry line. Image of (a) defect free fastener, (b) fastener with defect perpendicular to the current and (c) fastener with defect parallel to the current

3.2 RoC-GMR Probe with Orthogonal Excitation Coils

In order to ensure that the EC-GMR probe is capable of detecting defects independent of their orientation, an excitation method using orthogonal coils is proposed for generating a rotating planar excitation current.

Two planar coils as shown in Figure 3.3 that are perpendicular to each other and excited by current sources that are 90° apart in phase can generate rotating eddy currents. If the current in the coil oriented along the x direction is $I_x = I_0 \cos(\omega t)$,

then the current in the y direction coil is $I_y = I_0 \cos(\omega t + 90^0)$, where ω is the angular frequency, and I_0 is the current amplitude. The rotating exciting current generated by the orthogonal coils is sinusoidal in time, and so are the induced eddy currents in the sample.

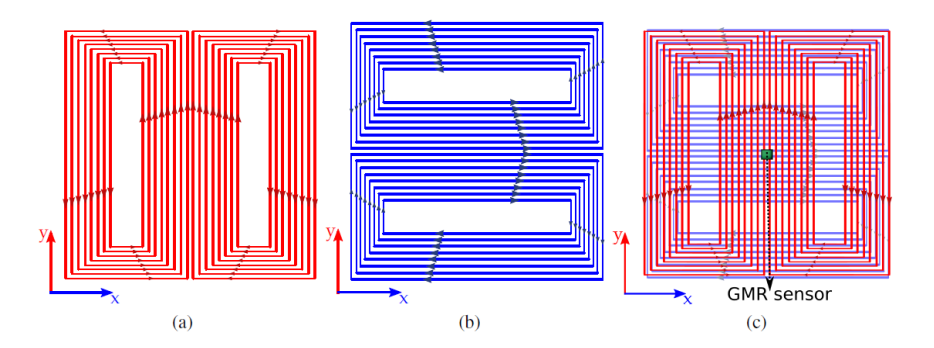


Figure 3.3.Design of the planar excitation coil with a rotating current field. (a) Unidirectional coil with a linear current $I_0\cos(\omega t + 90^0)$,. (b) Unidirectional coil with linear current $I_0\cos(\omega t)$. (c) The two unidirectional coils producing a rotating current, with the GMR sensor at the center.

As the induced eddy current is rotating, the current paths will be disrupted by defects of all orientations. It should be noted that in this configuration, in contrast to a line of symmetry with single excitation coil, there is only one symmetry point at the center of the coils. When the probe is put on top of healthy (defect-free) sample, the net magnetic field is largely tangential and the GMR sensor located at the null point, does not measure a signal. However, in the presence of a defect, the perturbation in eddy current flow produces a normal magnetic field that is measured by the GMR sensor located at the center. A rotating eddy current GMR (RoC-GMR) probe, consequently, offers similar sensitivity to cracks emanating around fastener sites in all orientations, as shown in Figure 3.4.

The operation of rotating current excitation with single sensor located at the center of the coils is validated experimentally. The experimental system is as shown in Figure 3.5. Currents from two sinusoidal currents sources, with 90 °phase difference obtained using a direct digital synthesis (DDS) scheme, are fed to power amplifiers and connected to the orthogonal coils. A lock-in amplifier model RF840 from Stanford

Research System is used to obtain the baseband signal. The output of the lock-in amplifier is sampled and stored. The experimental measurements are obtained using a high resolution scanning system. As there is only 1 sensor, a 2D raster scan is needed to cover a sample surface.

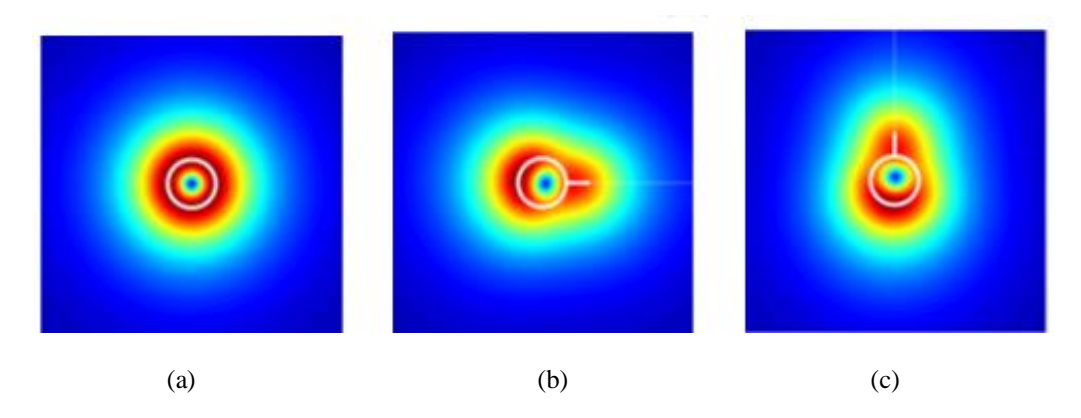


Figure 3.4. Simulation results of rotating current excitation with single sensor. Image of (a) defect free fastener, (b) fastener and horizontal defect and (c) fastener and vertical defect.

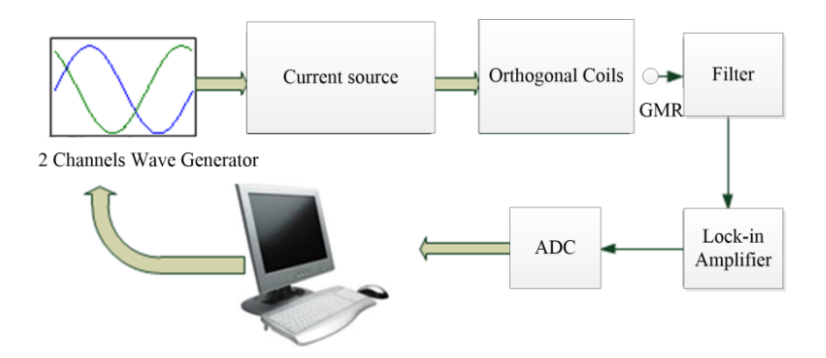
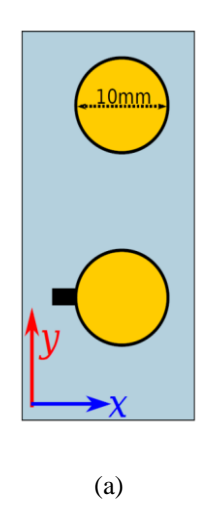


Figure 3.5. Experiment setup for rotating current EC-GMR probe with signal sensor

An aluminum sample, specified in Figure 3.6(a), is inspected using the probe. The thickness of the sample is 3mm. There are 2 circular holes in the sample: one without defect and the second hole has a radial defect. The liftoff of the probe is 1mm above the aluminum sample. The scan step size is 0.2 mm. The GMR sensor measurement is presented in Figure 3.6(b). The defect is visible from the collected data.



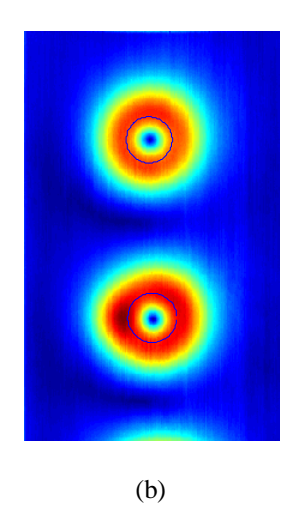


Figure 3.6. (a) Top view of aluminum test sample. (b) Experimental result of rotating current EC-GMR probe with single sensor.

3.3 Issues of RoC-GMR Probe with Array Sensors

As described in the previous section, a single sensor probe needs a 2D raster scan to cover a sample surface which makes inspection very slow. To increase inspection speed, it is necessary to use array sensors. However, there are two major factors associated sensor array in the case of orthogonal coil design namely, 1) non-uniform background field at the sensor location and 2) non-uniform induced currents in the test sample. These issues are described in detail below.

3.3.1 Non-Uniform Background Magnetic Field

With rotating current excitation obtained using an orthogonal coil arrangement, there is only one null field position, and sensors located at points other than the null field point are subject to strong background fields even in the absence of a defect. This is in contrast to a single coil EC-GMR system, which has an entire line of symmetry (null field area), allowing a sensor array to be placed along the line of symmetry.

The field distribution around orthogonal coil pairs was studied experimentally. Coils, each 98 mm long and 82 mm wide with 24 turns in each direction were excited by a 200Hz, 0.1 Ampere sinusoidal current source. The orthogonal coil was placed above a

defect free planar aluminum sample. A GMR sensor was used to scan the coil region in a 2D raster scan pattern to measure the normal component of the source magnetic field 1 mm above the coil. The experimental measurements are presented in Figure 3.7(a). Then the defect free planar aluminum sample was replaced by an aluminum sample containing a hole with a radial defect. The resulting field above the coil region was measured using a single GMR in a 2D raster scan. The defect dimensions are presented in Figure 3.7(b) while the experimental results are presented in Figure 3.7(c).

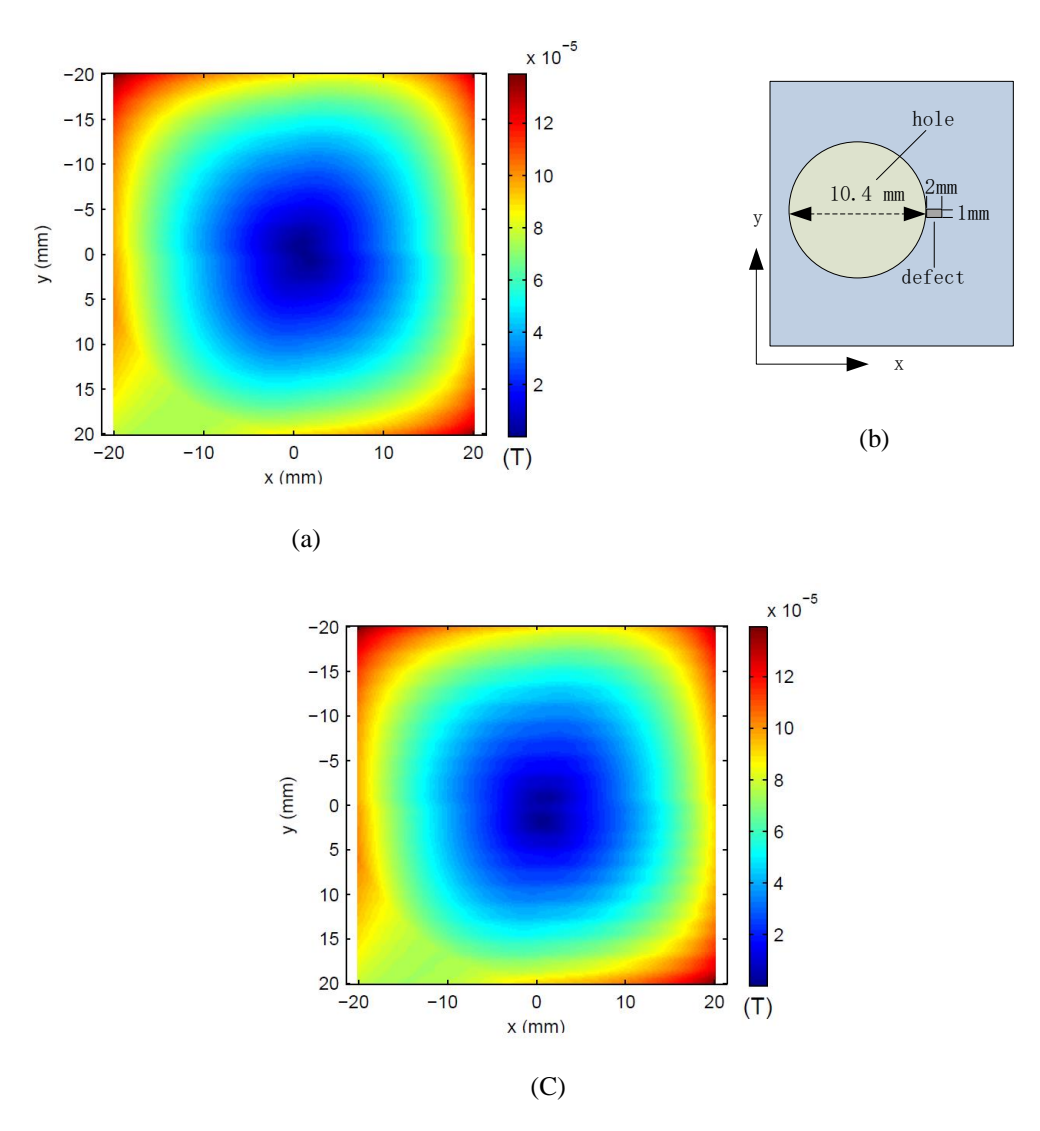


Figure 3.7. (a) Background field measured on defect free sample (b) Sample/defect geometry (c) Field measured on the test geometry shown in (b)

It is obvious that the background field dominates over the small perturbations resulting from the defect. In fact, it is difficult to visualize the difference between Figure 3.7(a) and (c) directly from the images. If the background field is subtracted, the difference signal highlights the flaw. Figure 3.8(a) shows the image of the hole and the radial crack. The difference signal showing the difference in magnitudes of the real and imaginary parts of the total signal and the background signal are plotted along the x direction at y = 0 in Figure 3.8 (b) and (c) respectively. The back ground field is an order of magnitude greater than the signal due to the defect. The background signal, in effect, masks the defect signal making it difficult to detect the defect.

The results shown in Figure 3.7 and Figure 3.8 highlight several challenges:

1) It should be theoretically feasible to measure the background field separately using a healthy specimen, and then subtracting the results from measurements obtained from a test signal to highlight the defect signal. This is difficult to accomplish in practice due to issues of registration and variations in the material and test conditions from test to test. It is simply not practical to measure the total signal and background separately then subtract the background largely due to the fact that the background is influenced by variety of factors, such as sensor liftoff, sample edges, adjacent fastener etc. Small errors in estimating the background signal can affect the result substantially.

2) Secondly, the limited dynamic range of amplifiers and analog-to-digital convertors (ADC) present challenges, since the amplitude of the background signal is much higher than the defect signal. If we wish to enhance the signal to noise ratio (SNR), it is necessary to subtract the background signal from the total signal. If the background signal is not subtracted most bits of the ADC will be used to represent the background signal.

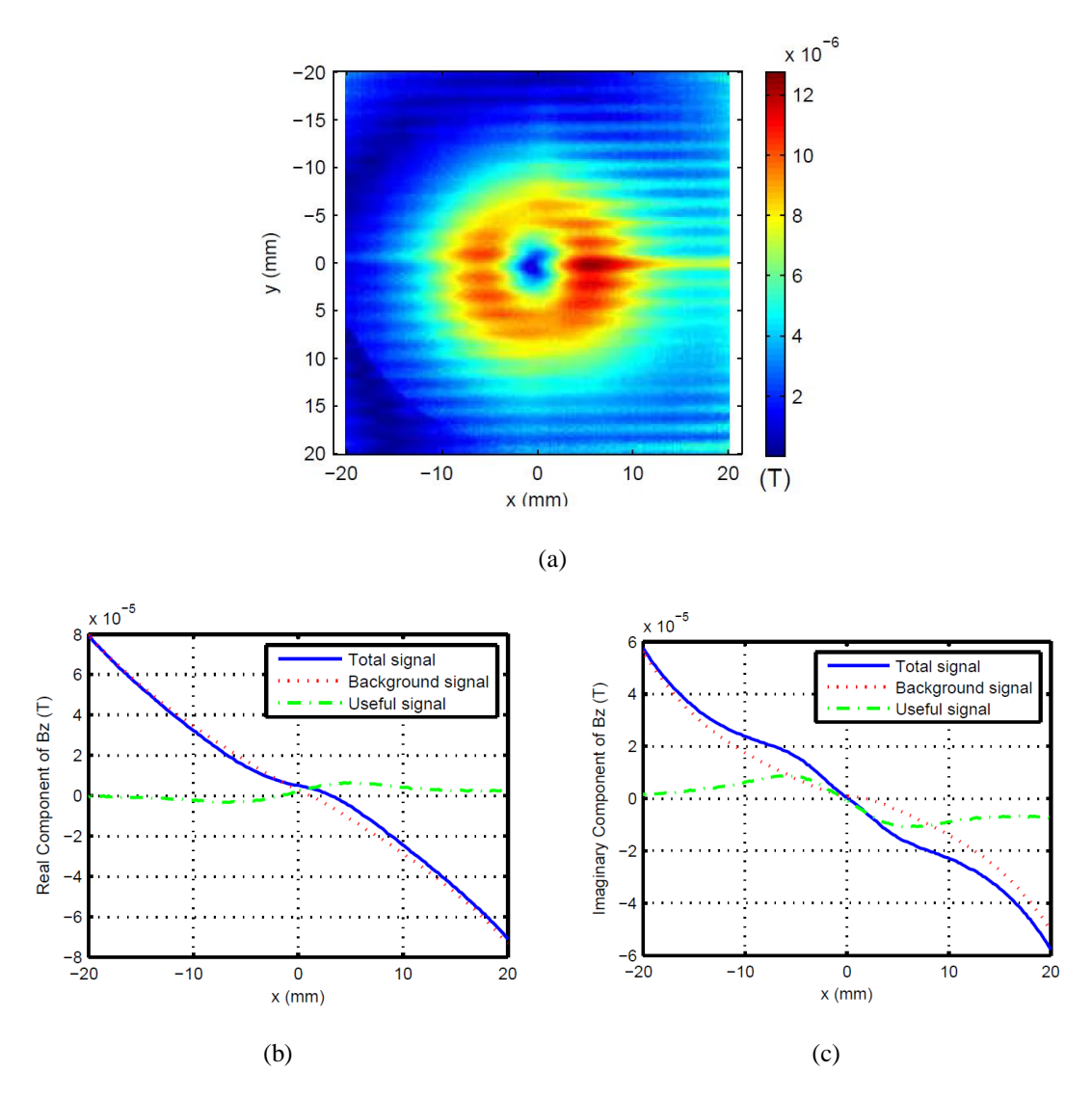


Figure 3.8. (a) Field Image after background subtraction. Line scan of B_z at y=0 (b) Real part (c) Imaginary part

3.3.2 Non-Uniform Induced Eddy Currents

Another issue of combining rotating current excitation with array sensor is that the intensity of induced eddy current is non-uniform along the sensor array. Consider a linear array sensors that are located along x direction at y=0, which are on the symmetry line of x direction coil but perpendicular to the symmetry line of y direction coil. Then the horizontal component of the magnetic field due to the y direction excitation current is not uniform along sensor array. Consequently, the eddy current induced inside the test sample is not uniform. The simulation results showing the x component of induced magnetic flux density (\bar{B}_x) and y component of induced eddy

current density (\bar{J}_y) inside aluminum sample are shown in Figure 3.9(a) and (b) respectively. The eddy current density below the center of the probe is higher in magnitude as compared to the eddy current density below the edge of the probe at the same depth.

The non-uniform distribution of eddy current implies that a defect located closer to the center of the sensor array will produce a stronger response as compared to the signal produced when the defect is located near the edge of the sensor array, as shown in Figure 3.10. When the probe is used to inspect a rivet structure, the fastener image will be distorted due to this inconsistency.

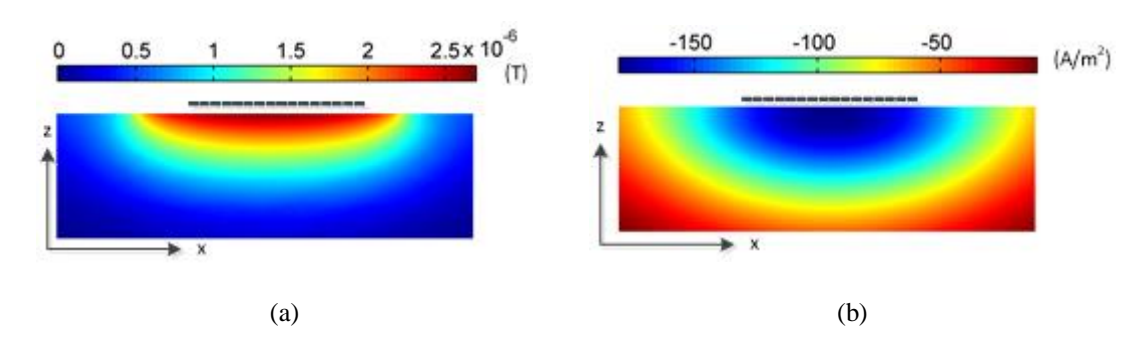


Figure 3.9. Induced magnetic flux density \bar{B}_x (a) and eddy currents \bar{J}_y (b) in aluminum sample due to y direction coil on y=0 plane.

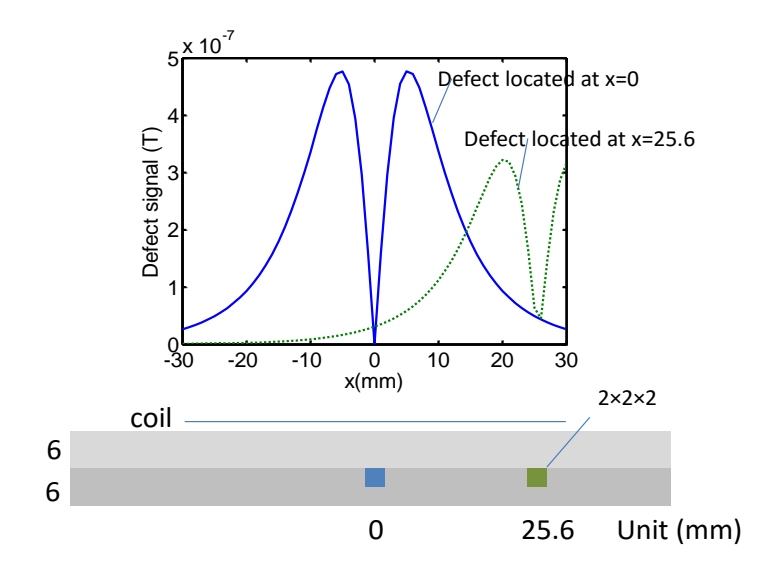


Figure 3.10. Signal (Bz) of defect located at x=0mm and x=25.6mm.

3.4 Conclusion

Following conclusions are derived from the results presented in this chapter.

- (1) The detection ability of EC-GMR system with single linear excitation coil depends on the defect orientation which is unknown.
- (2) RoC-GMR sensor is sensitive to defect of all orientation. The feasibility of RoC-GMR probe with single sensor is validated. However, there is only one null-field point for orthogonal rotating current excitation coils. In this case, a 2D raster scan is needed for a probe with single sensor to inspect a sample surface which is slow.
- (3) To increase inspection speed, it is necessary to use array sensors.
- (4) However, there are two major factors associated with orthogonal coil design, which give rise to challenges in experimental implementation of rotating current exciting coils together with array sensors.
- (5) It is necessary to subtract the background signal on the fly during a scan.
- (6) The excitation coil should be optimized to make the induced eddy current uniform along the sensor array.

Chapter 4 Novel RoC-GMR Probe with Array Sensors

4.1 Differential Measurement Method

Differential measurement method is proposed and discussed in this chapter as a new probe design that subtracts the background signal on the fly during inspection[69]. Effectively, this allows one to use array sensors for achieving rapid scan of the row of rivets.

4.1.1 Operating Principle

The approach used for differential measurement probe is depicted in Figure 4.1. Two linear arrays of GMR sensors are used with orthogonal excitation coils. The first array (GMR array 1) is located above the orthogonal coils and the second array (GMR array 2) is placed below the coils. The two arrays are located symmetrically with respect to the symmetry line of the y direction coil (coil 1) and are on the symmetry line of the x direction coil (coil 2). The output of GMR sensors in Array 1 is subtracted from the output of GMR sensors in Array 2 to obtain the probe output, as expressed in equation (4.1), where \overline{V}_2 , \overline{V}_1 are the output of sensors in array 2 and array 1 respectively.

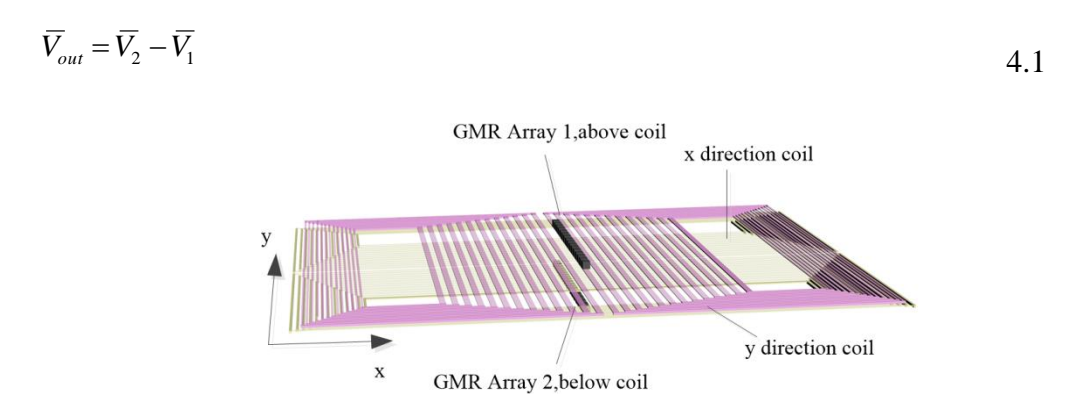


Figure 4.1.Schematic arrangement of the probe showing 3D view of the orthogonal coils and two GMR arrays.

Assuming that the GMR sensors are operating within their linear range, the output voltage is proportional to the local magnetic field. Hence the output of the differential probe is expressed using equation 4.2.

$$\overline{V}_{out} = k(\overline{B}_{z2} - \overline{B}_{z1}) \tag{4.2}$$

where k is the sensor gain constant (the sensor elements need be carefully matched to ensure similar levels of sensitivity), \overline{B}_{z1} and \overline{B}_{z2} are the normal component magnetic flux density at the two observation points. Using the superposition property, the magnetic field is decomposed into three components at every point: the field generated by the y direction coil (\mathbf{B}_{coil1}), the field generated by x direction coil (\mathbf{B}_{coil2}) and field related to the induced eddy currents in the sample ($\mathbf{B}_{eddycurrent}$). Hence the total field \mathbf{B} ,

$$B = B_{\text{coil1}} + B_{\text{coil2}} + B_{\text{eddycurrent}}$$
 4.3

Since the sensors are located on the symmetry line of coil 1, the normal component of $\mathbf{B}_{\text{coil}1}$, $\bar{B}_{\text{z coil}1} = 0$.

As the excitation frequency is low in EC-GMR applications, the magnetic field generated by coil 2 is expressed using equation 4.4.

$$\boldsymbol{B}_{coil2}(\boldsymbol{r}) = \mu \iint_{s} \frac{\boldsymbol{J}_{s} \times (\boldsymbol{r} - \boldsymbol{r}')}{4\pi |\boldsymbol{r} - \boldsymbol{r}'|^{2}} ds$$

$$4.4$$

where μ is permeability, J_s is current density, r and r' are observation point and source point vector respectively, and s is the coil surface domain. Here the current in the coil is modeled as a surface current. The normal component magnetic field ($\overline{B}_{z \text{coil2}}$) is expressed as:

$$\overline{B}_{z \text{ coil2}}(\mathbf{r}) = \mu \iint_{s} \frac{\overline{J}_{sx}(r_{y} - r'_{y}) - \overline{J}_{sy}(r_{x} - r'_{x})}{4\pi |\mathbf{r} - \mathbf{r}'|^{2}} ds$$

$$4.5$$

Since coil 2 consists of multiple line elements on the x-y plane, it is modeled using current elements ($\overline{I}dl$) and the magnetic field generated by coil 2 is synthesized via superposition of magnetic fields of all the current elements at any observation point. For each current element, the normal component magnetic field generated by the current element (\overline{B}_{ze}) is expressed as equation 4.6.

$$\overline{B}_{ze}(\mathbf{r}) = \mu \frac{\overline{I}dl_x \bullet (r_y - r_y') - \overline{I}dl_y \bullet (r_x - r_x')}{4\pi |\mathbf{r} - \mathbf{r}'|^2}$$

$$4.6$$

The two GMR arrays are located symmetrically above and below coil 2, at r_1 and r_2 as shown in 4.7; *i.e.*

$$|r_2 - r'| = |r_i - r'| \tag{4.7}$$

The spatial vectors $r_1 - r'$ and $r_2 - r'$ have identical projection to the coil plane:

$$r_{1y} - r'_{y} = r_{2y} - r'_{y}$$

$$r_{1y} - r'_{y} = r_{2y} - r'_{y}$$
4.8

Substituting equation 4.7 and 4.8 into 4.6, it is seen that:

$$\overline{B}_{ze}(r_1) = \overline{B}_{ze}(r_2) \tag{4.9}$$

This leads to the result

$$\overline{B}_{z \text{coil2}}(r_2) - \overline{B}_{z \text{coil2}}(r_7) = 0$$
4.10

Hence the background field generated by Coil 2 is offset and the output of the probe corresponds to the field due to the eddy current in the sample ($B_{\rm eddycurrent}$). When the probe is placed on a defect free planar sample, sensor pairs at locations other than the null field point of $B_{\rm eddycurrent}$ will be nonzero. We refer to this nonzero signal as "baseline" signal. It is important to note that the baseline signal is of the same order of magnitude as the defect or fastener signal in contrast to the background signal which is an order of magnitude greater than the defect signal. Hence small errors in

estimating the baseline will not affect the result substantially. Moreover, the baseline signal will not affect the dynamic range of amplifiers and analog-to-digital convertors (ADC). As a result, the baseline can be measured and subtracted during inspection.

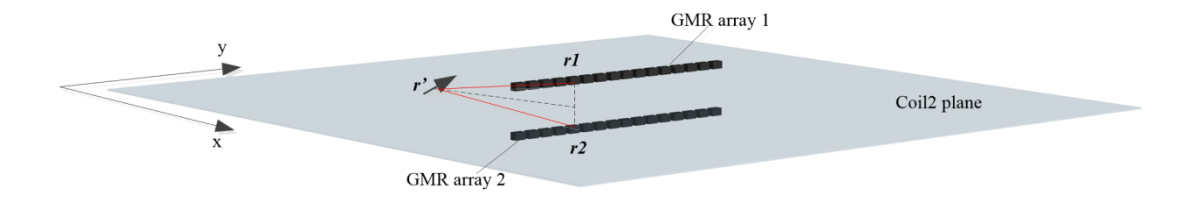


Figure 4.2.3D view showing spatial relationship between coil 2 and the sensor arrays.

4.1.2 Simulation Results

In order to validate the concept, a finite element model (FEM) is used to predict output image of the differential rotating current probe from cracks in a multi-layer riveted structure. The test specimen is a two-layered aluminum structure as shown schematically in Figure 4.3. A radial crack spans the thickness of the bottom layer. l_d represents the length of the crack. The crack orientation is at an angle α with respect to the y-axis. A 200 Hz sinusoidal current is applied to each of the orthogonal coils. $\mathbf{J}_1 = \hat{x} \mathbf{J}_0$ and $\mathbf{J}_2 = \mathbf{j} \hat{y} \mathbf{J}_0$ represent the current densities in the two unidirectional excitation coils. The normal component of the magnetic flux density \mathbf{B}_z is measured at a liftoff of 1mm and 9 mm from the top surface of the sample. The C-scan image is produced by calculating the field values at the center of the mesh elements at a given liftoff distance from the top surface of the test sample at each scan point.

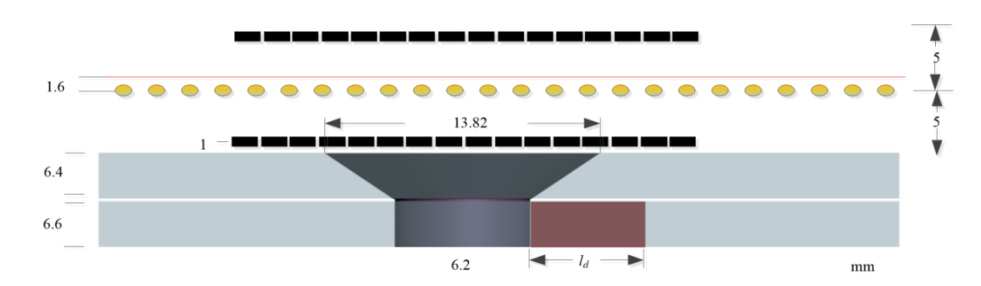


Figure 4.3. Dimensions of the test sample and sensor arrays location.

The simulation results for a crack of length l_d =10mm, and orientation α = 0 °(from the y-axis) are presented in Figure 4.4. Figure 4.4(a) shows the C-scan image of Bz measured by the lower sensors at liftoff z =1 mm. Figure 4.4 (b) shows the C-scan image of Bz measured by the top sensors at liftoff z = 9 mm. Figure 4.4(c) shows the result of subtracting (b) from (a), representing the output of the probe. Figure 4.4 (d) shows the result after the baseline signal is subtracted.

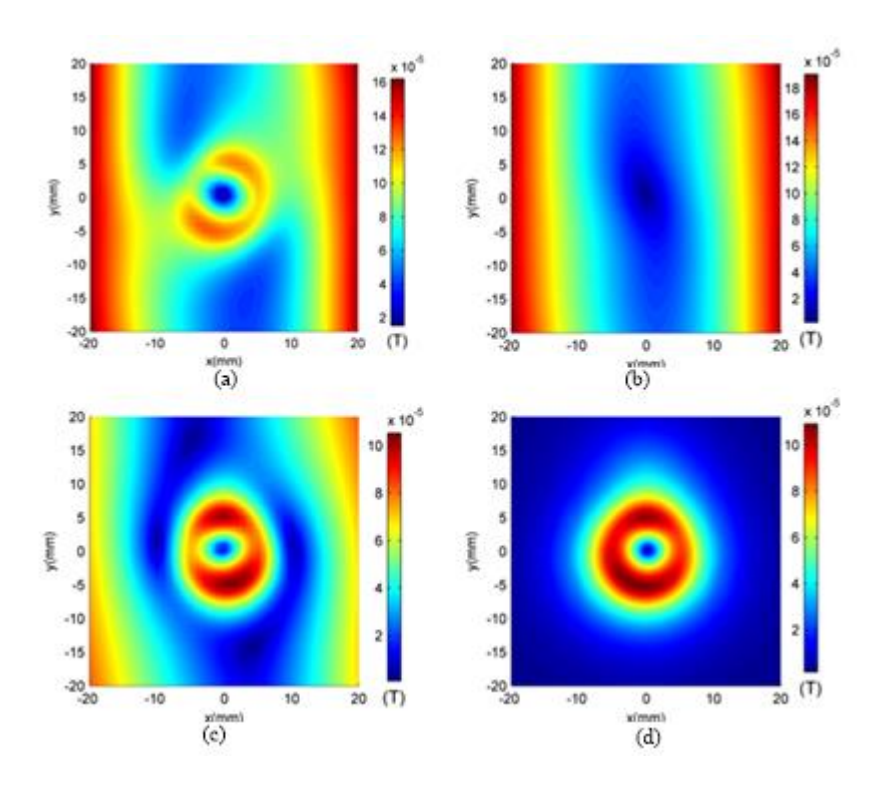


Figure 4.4. Simulation results showing amplitude of Bz for aluminum fastener with radial notch (length l_d =10mm, orientation α =0°) at (a) z=1 mm. (b) z=9 mm.(c) Differential Image (d) Differential Image after baseline subtraction.

Figure 4.5 presents the simulation results of the differential probe with various crack orientations at the fastener site in the second layer. The fastener image is a perfect circle in the absence of a crack, as shown in Figure 4.5 (a). The image rotates as the crack orientation is varied from 30 °to 90 °. These simulation results illustrate that the probe is sensitive to cracks of all orientations.

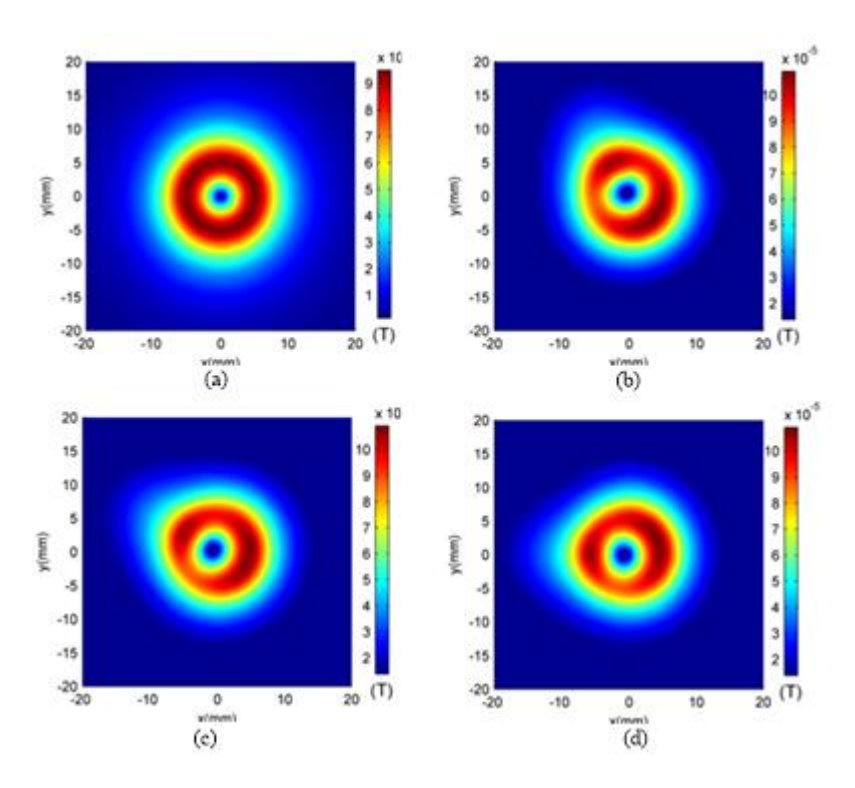


Figure 4.5. Simulation result for cases (a) l_d =0 mm (no crack). (b) l_d =10 mm, α =30 °. (c) l_d =10 mm, α =60 °. (d) l_d =10 mm, α =90 °.

4.2 Optimization of Rotating Current Excitation Coil

As indicated in section 3.3, the second issue using the proposed approach combining rotating current excitation with array sensor is that the intensity of induced eddy current is non-uniform along the sensor array. This problem was addressed by a systematic study of the coil design. Instead of a uniform coil with non-uniform excitation field, the coil parameters were optimized to have spatially varying current densities so that the excitation field and hence induced current density was uniform.

4.2.1 Current Distribution Optimization

The array sensors are located on the symmetry line of x direction coil but perpendicular to the y direction coil. Hence it is important that that the fields generated by the y direction coil in the sensor range is uniform across the array. The lateral view of the y direction coil and the sensors is as shown in Figure 4.6. The coil consists of the active region with excitation coil lines and the region carrying return

paths of the coil. The active part lies in $x \in (-a, a)$ while the return paths lie in $x \in (b, c) \cup (-c, -b)$. Here 0 < a < b < c.

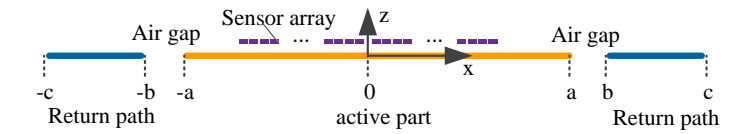


Figure 4.6. Lateral view of the y direction excitation coil and sensor array.

Let $J_{(x)}$ (-c \leq x \leq c) be the current density distribution of the exciting coil in the active region, which follows equations 4.11 and 4.12. Here equation 4.11 is due to the symmetry structure of the coil. Since the current density distribution is an even function; it is only necessary to optimize $J_{(x)}$ $x \geq 0$. Equation 4.12 indicates that the total return current equal to the total exciting current for each half of the coil to satisfy the current continuity theorem.

$$J_{(x)} = J_{(-x)} 4.11$$

$$\int_0^c J(x)dx = 0 \tag{4.12}$$

Since the return part is relatively far away from the sensors and the width of the return part is kept as small as possible to make the coil size small, it is reasonable to assume that the current distribution in the return path is a constant ($J_{(x)} = J_r$). The current density in the air gap between the active region and return path is 0. The current density distribution in the active region is a function of x that must be optimized. Let J(x) be written as n^{th} order polynomial in the region ($x \in [0, a]$).

$$J(x) = \begin{cases} \sum_{k=0}^{n} p_k x^k & 0 \le x \le a \\ 0 & a < x < b \\ J_r & b \le x \le c \end{cases}$$
 4.13

Here p_k ($k = 0,1,2 \cdots n$) are the coefficients of the polynomial[70]–[72], which is unknown and must be optimized. Substituting 4.12 into 4.13,

$$J_r = \frac{1}{b-c} \sum_{k=0}^n \int_0^a p_k x^k dx = \frac{1}{b-c} \sum_{k=0}^n p_k \frac{a^{k+1}}{k+1}$$
 4.14

 B_x in air at observation point (x', 0, z') is written as

$$B_x(x',z') = \int_{-c}^{c} G(x'-x,z')J(x)dx$$
 4.15

where G(x, z) is Green's function of y direction current.

$$G(x,z) = \frac{\mu_0 z}{4\pi\sqrt{x^2 + z^2}} \int_{-l/2}^{l/2} \frac{\mathrm{dy}}{x^2 + z^2 + y^2}$$
 4.16

where l is the length of the current. Invoking 4.11 to 4.15:

$$B_x(x',z') = \int_0^c [G(x'-x,z') + G(x'+x,z')]J(x)dx$$
 4.17

Invoking equation 4.13, 4.14 to 4.17 and interchanging summation and interpolation

$$B_{x}(x',z') =$$

$$\sum_{k=0}^{n} p_{k} \left\{ \int_{0}^{a} [G(x'-x,z') + G(x'+x,z')] x^{k} dx + \int_{b}^{c} [G(x'-x,z') + G(x'+x,z')] x^{k} dx \right\}$$

$$(x,z')$$
 $\frac{1}{h-c} \frac{a^{k+1}}{k+1} dx$ 4.18

Define

$$\gamma_k(x',z') = \int_0^a [G(x'-x,z') + G(x'+x,z')] x^k dx + \int_b^c [G(x'-x,z') + G(x'-x,z')] x^k dx + \int_b^c [G(x'-x,z') + G($$

$$[x, z'] \frac{1}{h-c} \frac{a^{k+1}}{k+1} dx$$
 4.19

Then

$$B_{\mathcal{X}}(\mathcal{X}', \mathcal{Z}') = \sum_{k=0}^{n} \gamma_k p_k \tag{4.20}$$

Suppose there are m observation points $(x'_i, 0, z'_i)$, i=1,2 ·· m. Define vector

$$\mathbf{B}_{x} = [B_{x_{1}}, B_{x_{2}}, \dots, B_{x_{m}}]^{T}$$

$$4.21$$

Then

$$\mathbf{B}_{x} = \mathbf{\gamma} \mathbf{P} \tag{4.22}$$

Here γ is a (n+1)×m matrix that defined as

$$\mathbf{\gamma}(i,j) = \gamma_{i(x'_j,z'_j)} \tag{4.23}$$

P is the unknown power series factors vector,

$$\mathbf{P} = [p_0, p_2 \dots p_n]^T \tag{4.24}$$

To make Bx flat through all the observation points

$$\mathbf{B}_{x}(i) = v \quad i = 1,2 \dots m$$
 4.25

Here v is a non-zero constant value. In matrix notation 4.25 is written as

$$\mathbf{\gamma}\mathbf{P} = \mathbf{V} = [v, v \dots v]^T \tag{4.26}$$

Equation 4.26 is consistent if and only if the coefficient matrix γ and the augmented matrix $\tilde{\gamma}$ of the system have the same rank.

$$rank(\boldsymbol{\gamma}) = rank(\widetilde{\boldsymbol{\gamma}}) \tag{4.27}$$

where $\widetilde{\gamma} = |\gamma, V|$.

4.2.2 Size of Active Region 'a'

The solvability of equation 4.26 depends on the coil's parameters. One of the most important parameters is the size of active region of coil. Consider a sensor array with 32 GMR sensors located at $x'_i = \pm (2i-1)mm$ ($1 \le i \le 16$). Since the defects are typically assumed to be in the second layer at a depth of 6mm in the multiple-layer structure; it is required to have uniform eddy current at this depth. The observation points where the exciting magnetic field is measured are at

$$x'_{i} = \begin{cases} 0 & i = 1mm \\ 2i - 1 & 1 \le i \le 16mm \end{cases}$$
 4.28

$$z'_i = -6 \ 1 \le i \le 17 \text{ mm}$$
 4.29

there are 17 observation points (m=17). We set n=16 to make γ a square matrix.

The width of the return path should be one quarter of the exciting part to guarantee that there is enough space for return wires when fabricating the coil on PCB.

$$c - b = \frac{a}{4} \tag{4.30}$$

Assume the air gap width is 5 mm, as specified in equation 4.31. The effect of airgap width will be discussed later.

b - a = 5 mm 4.31

Then the effect of 'a' is studied numerically by sweeping parameter 'a' from 25mm to 50mm with 1mm step size. For each 'a', 'b' and 'c' calculated according to equation 4.30 and 4.31. γ was calculated from equation 4.19. Then equation 4.26 was analyzed. Equation 4.26 is not consistent when a \leq 26mm with no non-zero solution. When a \geq 27 mm, the non-zero solutions of \mathbf{P} is derived from equation 4.26 and J(x) is calculated from equation 4.13. Some examples of distributions of J(x) are presented in Figure 4.7 (a). It is seen that J(x) oscillates between positive and negative values for value of a \leq 32 mm, and these are obviously not acceptable solutions. So 'a' should be no less than 33mm. This is reasonable considering that the sensor array is located at $x \in (-31,31)$. Figure 4.7(b) presents the optimized current density distribution when $33\leq$ a \leq 39, in which cases J(x) is always positive.

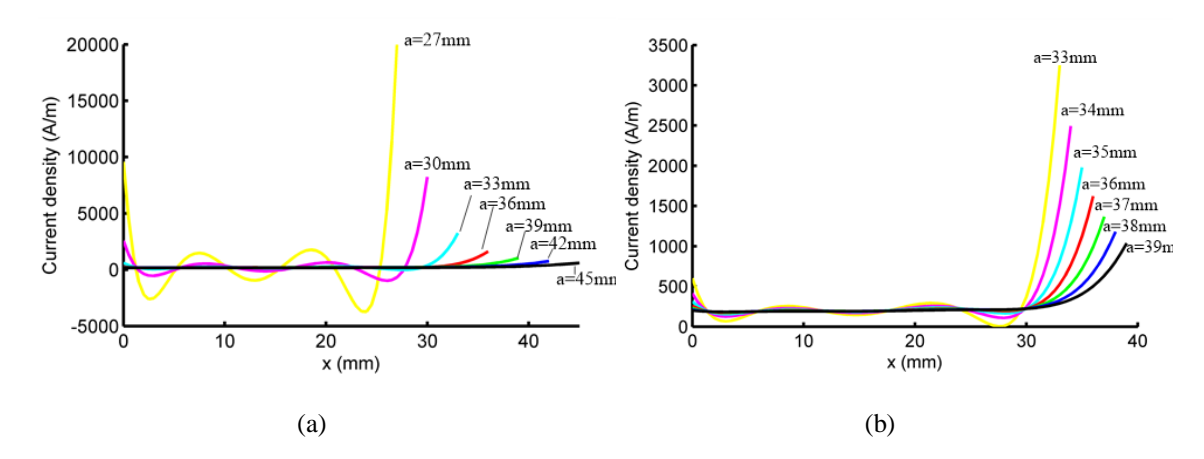


Figure 4.7. Theoretical current density vs. x for different parameter 'a'.

Small 'a' is preferred, since the overall probe size should be small. However, it is should be noted that when 'a' is small, the variation of J(x) is very large, e.g. when a=33mm, the maximum current density is 3248 A/m, while the minimum current density is only 3.78A/m. Such a distribution of J(x) cannot be realized on a PCB. So a constraint is introduced as following:

$$\eta = \frac{\max|J(x)|}{\min|J(x)|} \quad 0 \le x \le a \tag{4.32}$$

Keeping fixed air gap (5mm) between the active region and return path, the variation of η with 'a' is plotted in Figure 4.8. For η to be less than 10, we need $a \ge 36mm$.

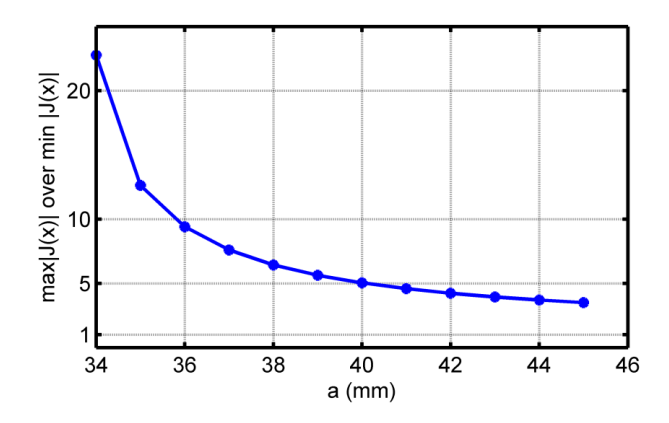


Figure 4.8. η defined as equation (4.32) vs. parameter 'a'

4.2.3 Effect of Air Gap Width

In previous section, the air gap width is assumed to be 5 mm. The effect of air gap width is studied in this section. The air gap width (w_{air}) is varied from 1 mm to 9 mm with step size 1mm and the process described above was repeated. The value of η defined in equation 4.32 is calculated for different air gap widths. The plots of η vs. 'a' for different air gap widths are presented in Figure 4.9.

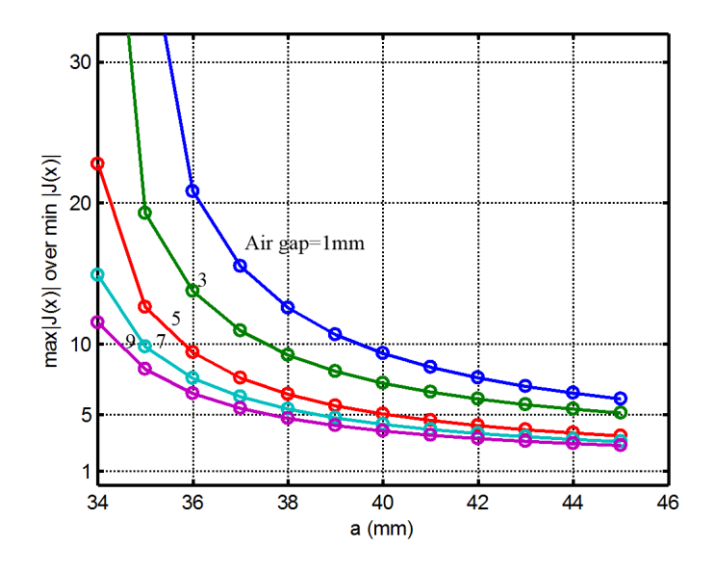


Figure 4.9. η vs. parameter 'a' for different air gap width

For each air gap width, there is a minimum possible 'a' (a_{min}) to satisfy $\eta < 10$, as listed in Table 4.1. The total coil size (w) is calculated according following equation 4.33.

$$w = 2(a + w_{air} + a/4) 4.33$$

As the air gap increases, the value of ' a_{min} ' decreases, hence a good tradeoff is to use air gap=5mm, a=36mm.

Table 4.1. Minimum coil size satisfying η < 10 for different air gap width

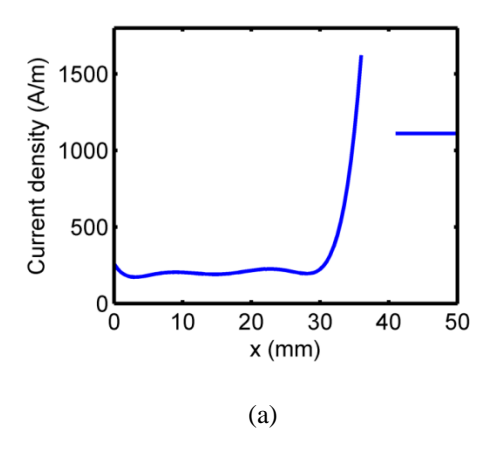
air gap(mm)	1	2	3	4	5	6	7	8	9
'a _{min} ' (mm)	40	39	38	37	36	36	35	35	35
w (mm)	102	101.5	101	100.5	100	102	101.5	103.5	105.5

4.2.4 Coil Design

Using $w_{air} = 5$ mm, a=36mm, the total width of the coil (w) is:

$$w = 2c = 100 \, mm$$
 4.34

The current density distribution with x is shown in Figure 4.10(a) for x>0. The width of each line of the coil d_w is derived from equation 4.35.



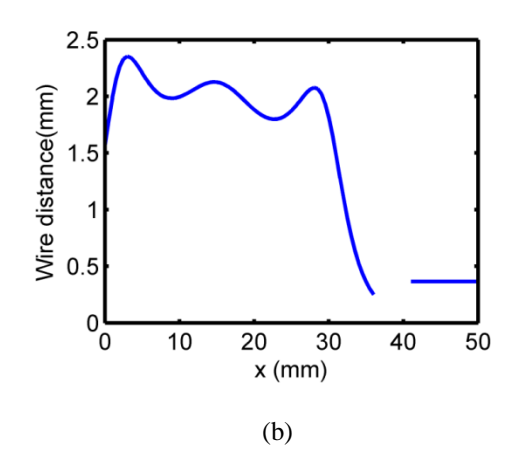


Figure 4.10. Optimization result: (a) current density vs. x and (b) wire distance vs. x.

$$d_w(x) = \frac{1}{J(x)} \times \frac{\max|J(x)|}{d_m}$$

$$4.35$$

where d_m is the minimum width between wire lines. Here we use the result that $d_m = 0.25mm$. The value of d_w vs. x is as shown in Figure 4.10(b).

The positions of each line/wire x_{w_i} are derived according following equations.

$$x_{w_1} = \frac{d_w(0)}{2} \tag{4.36}$$

$$x_{w_{i+1}} - x_{w_i} = d_w \left(\frac{x_{w_{i+1}} + x_{w_i}}{2}\right), i > 1 \text{ and } x_{w_{i+1}} < a$$
 4.37

The final optimized coil design with 50 turns wires is presented in Figure 4.11.

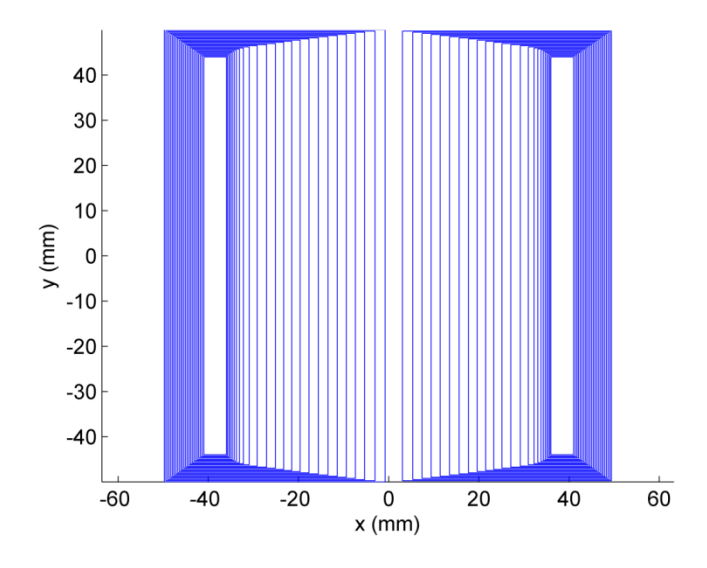
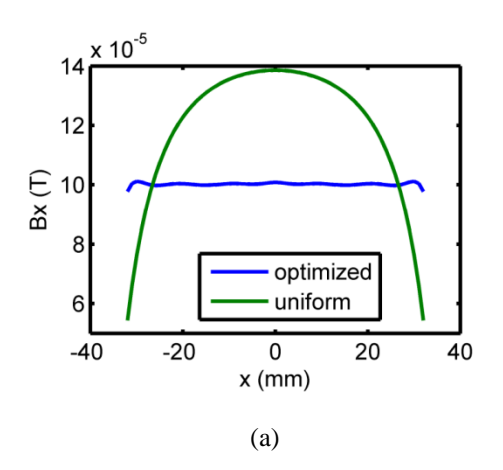


Figure 4.11. Top view of the optimized coil.

The magnetic field generated by the optimized coil in air is calculated and compared with the magnetic field generated by conventional uniform coil. The two coils have identical coil size and number of turns. A current of frequency 100Hz, amplitude 0.39A is used as input. The variation of Bx at the sensor region is greatly reduced by using the optimized coil in comparison to that obtained using conventional uniform distribution coil, as shown in Figure 4.12(a).

Even though the normal component magnetic field (Bz) is not an objective function during this optimization, as seen in Figure 4.12 (b), the distribution of the Bz also becomes flatter with the optimized coil, in comparison to that obtained with uniform coil.



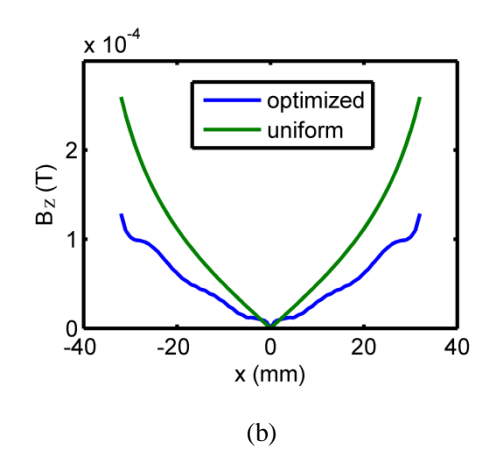


Figure 4.12:Numerical calculation results of (a) Bx at the observation points (z=-6mm) and (b) Bz at the sensors locations (z=2mm) of optimized coil and uniform coil.

4.2.5 Performance Analysis

3D finite element models (FEM) are used to analyze the performance of the optimized coil in detecting subsurface defects.

4.2.5.1 Induced Eddy Current

First, eddy currents induced in an aluminum plate is calculated using both, the optimized non-uniform coil and conventional uniform coil. In order to make the results comparable, the conventional uniform coil has identical size and number of turns as the optimized coil. The liftoff distance of coil from the sample top surface is 1 mm. The excitation current of frequency 100Hz and amplitude 1A is passed through each coil and induced eddy currents are calculated. The results are presented in Figure 4.13, where the amplitude of the induced eddy current density is plotted.

For a quantitative comparison, a line scan at depth 5mm is presented in Figure 4.14. It is found that the eddy current induced by the optimized coil is more constant along the sensor array range at a depth of 6mm from the surface than that of conventional uniform coil.

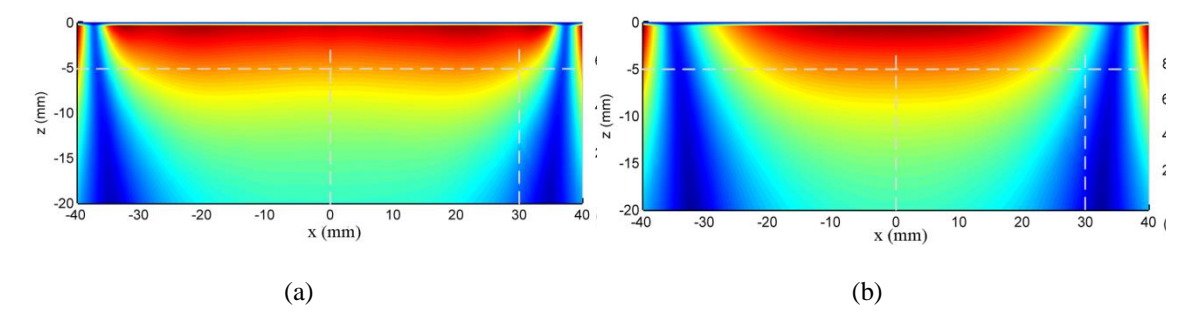


Figure 4.13. Eddy current in aluminum plane induced by optimized non-uniform coil (a) and conventional uniform coil (b).

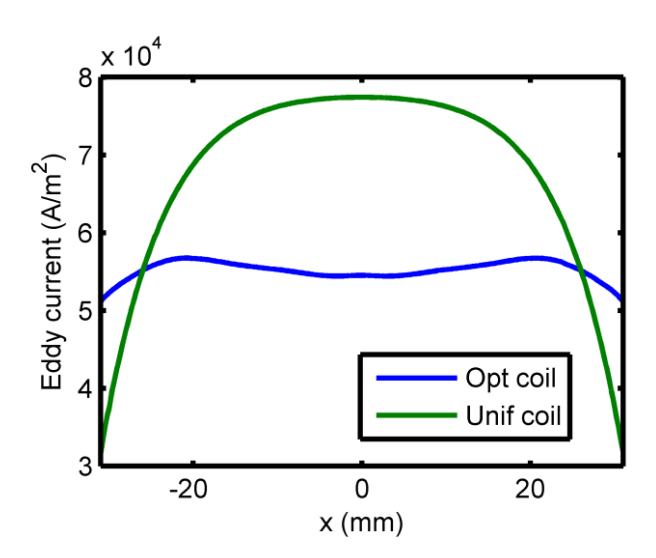


Figure 4.14. Eddy current in aluminum sample at depth of 5mm from surface.

4.2.5.2 Detection of Subsurface Defects at Different Locations

A direct consequence of the eddy current distribution of the optimized coil is presented in this section. Subsurface defects located at the center of the coil (x=0 mm) and away from the center (at x=30 mm) are simulated. The sample and defect geometry dimensions are specified in Figure 4.15(a). Both optimized non-uniform coil and conventional uniform coil are simulated. The liftoff distance of coil from the sample top surface is 1 mm. Normal component magnetic field (Bz) 1 mm above the coil is measured. To highlight the defect signal, background signal is obtained by placing the coil on top of defect free aluminum sample and subtracted from the measured signal.

The simulation results are presented in Figure 4.15(b). For uniform distribution coil, the peak signal is reduced to 39.23% when the defect is moved from the center of the coil to x=30 demonstrating that defect located near the coil edge is detected with a much weaker response as compared to the signal produced by the same defect at the coil center. However, for the optimized coil, the peak signal reduced to 81.25%, thereby confirming better performance of the optimized non-uniform coil.

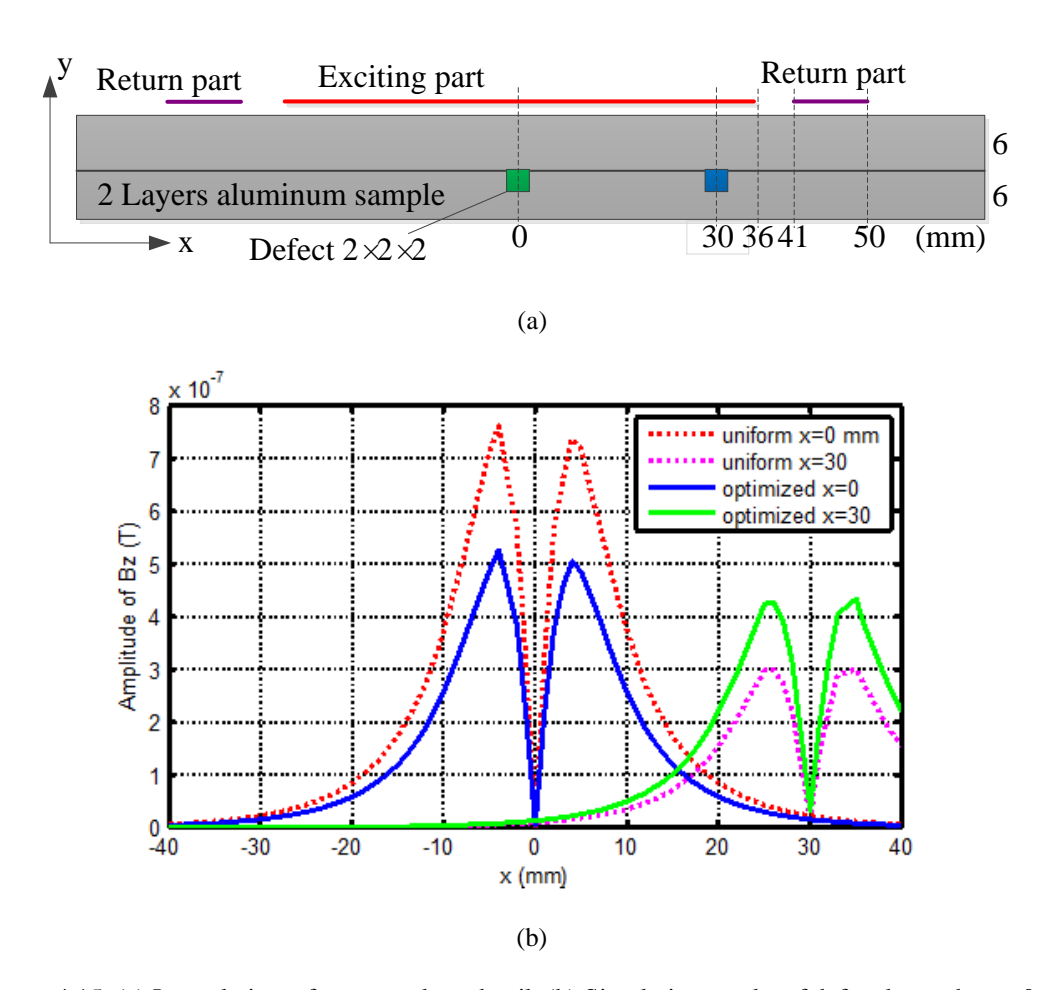


Figure 4.15. (a) Lateral view of test sample and coil; (b) Simulation results of defect located at x=0 mm and x=30mm after background subtraction.

4.2.5.3 Detection of Defect under Fastener Head

Next, a two-layered aluminum structure as shown schematically in Figure 4.16 with fastener and defect is simulated. A radial 10mm length notch spans the thickness of the second layer. The notch orientation is along the x-axis. Two identical orthogonal coils with the optimized design are used to induce rotating eddy current. Sinusoidal

current is applied to each of the orthogonal coils. $\mathbf{J}_1 = \hat{x}\overline{\mathbf{J}}_0$ and $\mathbf{J}_2 = \mathbf{j}\hat{y}\overline{\mathbf{J}}_0$ represent the currents in the two unidirectional excitation coils. The C-scan image is produced by calculating the normal component of the magnetic field (Bz) values at the sensor location at 1mm liftoff distance above the coils at each scan point. To highlight the fastener and defect signal, the background signal obtained by placing the coils on top of defect free sample was subtracted from the measured signal.

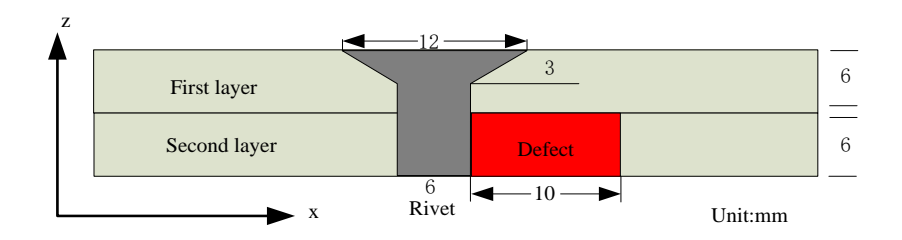


Figure 4.16. Dimensions of the test sample in the FEM model.

Two different cases are simulated for both optimized non-uniform coils and uniform distribution coils: 1) the fastener center is aligned with the orthogonal coils' center (x=0); 2) the fastener center is shifted by 20 mm along x axis (x=20). The simulation results of magnitude of the normal component magnetic field (Bz) is calculated and plotted in Figure 4.17.

To quantify the distortion introduced by the presence of a defect, all contiguous pixels above a preselected threshold value v are identified and a contour plot enclosing the region containing pixels is drawn. The contour plot obtained by setting v equal to 30% of the peak value is indicated by white dashed line in the Figures. Defining the deformation coefficient ϵ is defined

$$\epsilon = \left| \frac{r_{max} - r_0}{r_0} \right| \times 100\% \tag{4.38}$$

where r_0 is the radius of the contour plot of the image obtained with a defect free fastener and infinite current foil excitation, as shown in Figure 4.18, r_{max} is the

maximum distance from the fastener center to the contour plot. The deformation coefficients are compared in Figure 4.19.

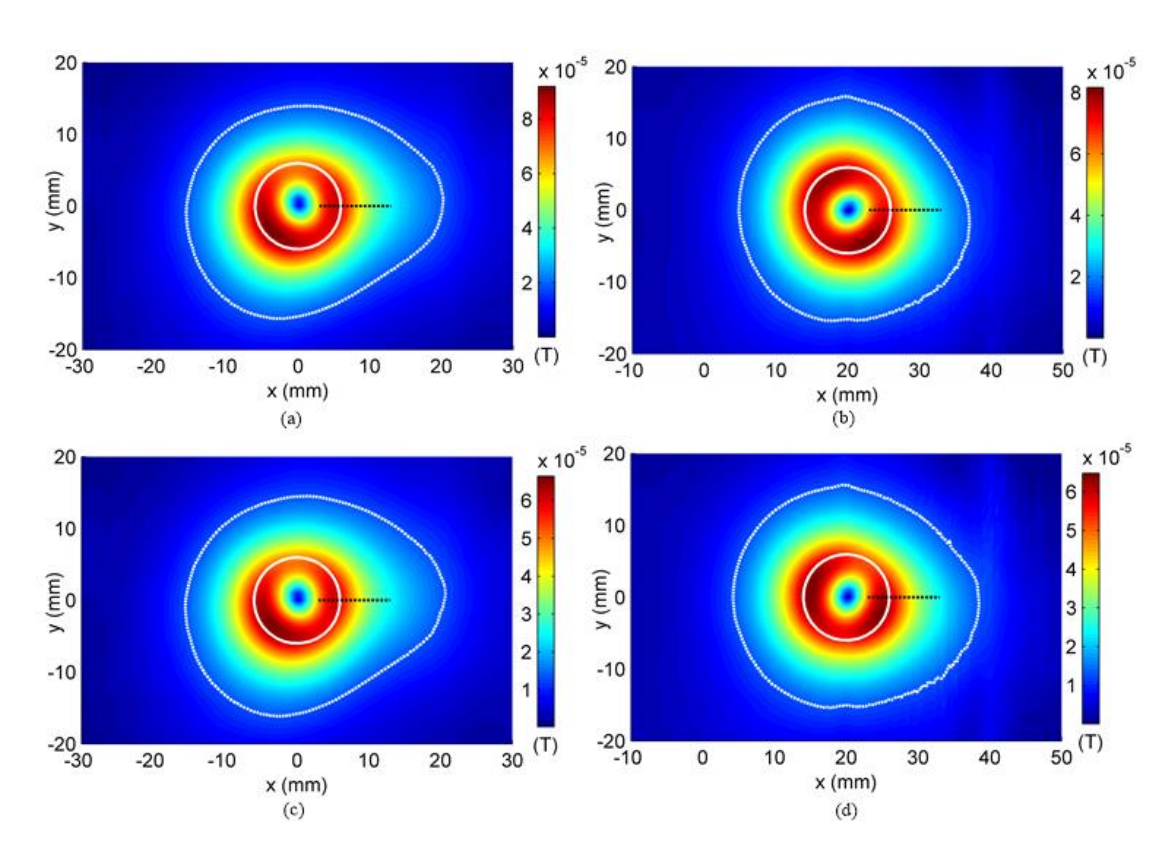


Figure 4.17. Simulation results for cases: (a)uniform coil, fastener center located at x=0mm, (b) uniform coil, fastener center located at x=20mm, (c) optimized non-uniform coil, fastener center located at x=0mm, (d) optimized non-uniform coil, fastener center located at x=20mm.

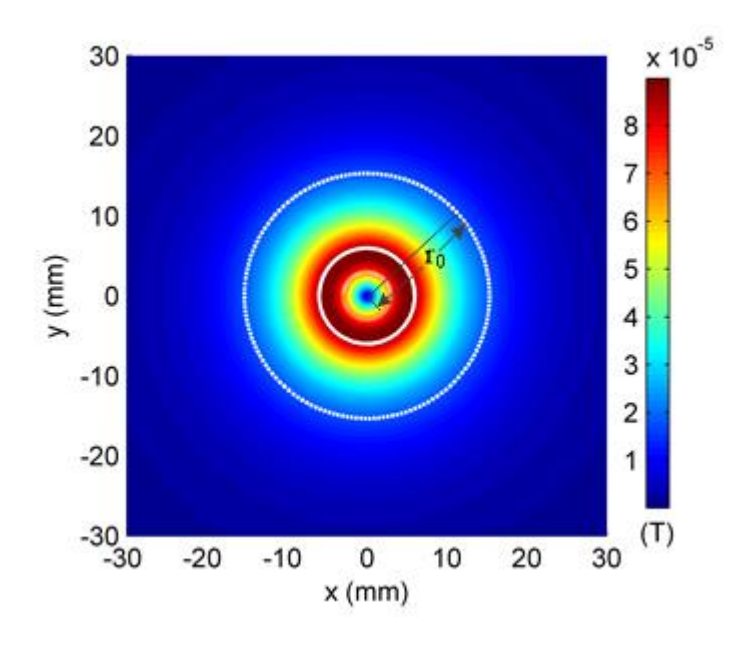


Figure 4.18. Simulation result of defect free fastener.

It is found that the distortion coefficient of optimized coil has better performance than that of uniform coil. When fastener center is shifted by 20mm from coil center along x axis, the distortion coefficient for uniform distributed coil drops from 32.42% to 12.41%. However, distortion coefficient for the optimized coil only reduces from 34.8% to 20.8%.

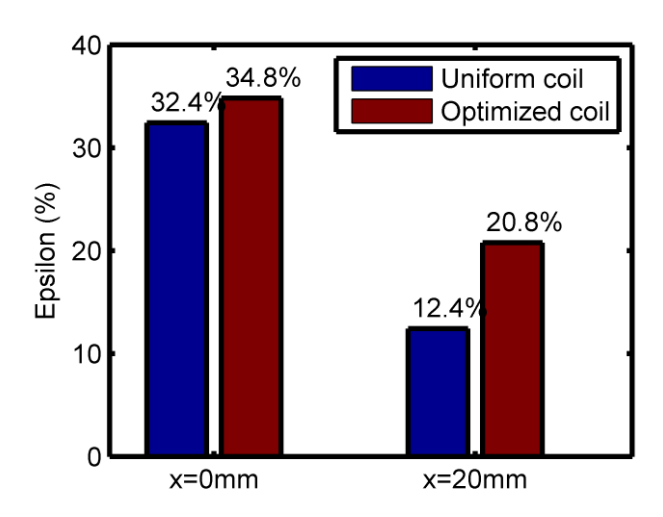


Figure 4.19. Comparison of reduction of ϵ of conventional uniform coil and optimized coil.

4.3 Experiment Results and Discussion

A RoC-GMR probe with array sensors and optimized coil design for multilayer structure inspection was designed, built, tested and validated. The experiment results are presented and discussed in this section.

4.3.1 Experiment Setup

A prototype probe has been built to demonstrate the proof of concept. GMR Sensor Model GF708 from Sensitec is used to build the prototype. The characteristic curve of GF708 is as shown in Figure 4.20. The operating point of GF708 is shifted to the linear part of its characteristic by the manufacturer for analog measurement. The sensor employs on-chip flux concentrators to increase sensitivity (130 mV/mT). The sensor is available as a bare die with gold terminals. This configuration offers the

smallest package size of all commercial GMR sensors currently, allowing us to build a relatively high spatial resolution array.

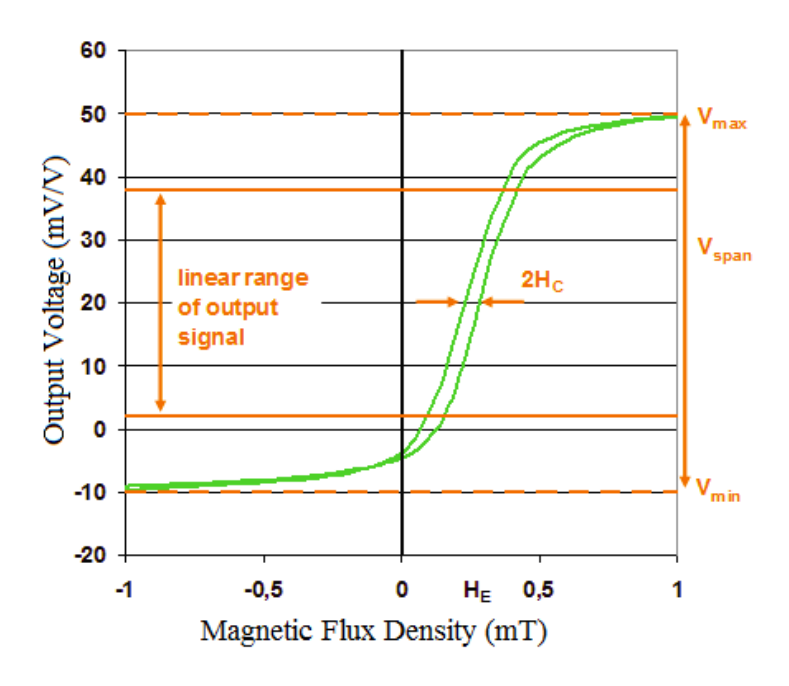


Figure 4.20. Typical output voltage of GF708 vs. magnetic flux density[73].

A printed circuit board (PCB) is used to place the GMR arrays on both sides of the orthogonal coils. The two sensor arrays are located on the two sides of a slot on the PCB as shown in Figure 4.21. The excitation coil board runs through the slot and is perpendicular to the sensor board. The two sensor arrays are placed on the symmetry plane of the top coil. The distance between the lower coil and the GMR sensors is 4 mm for both arrays.

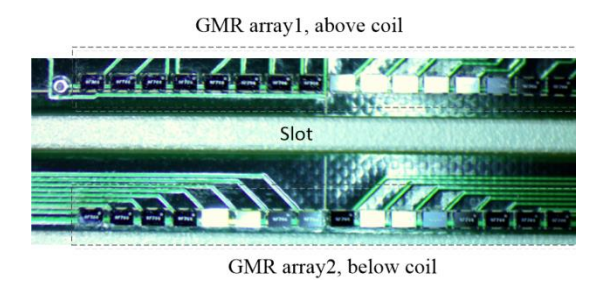
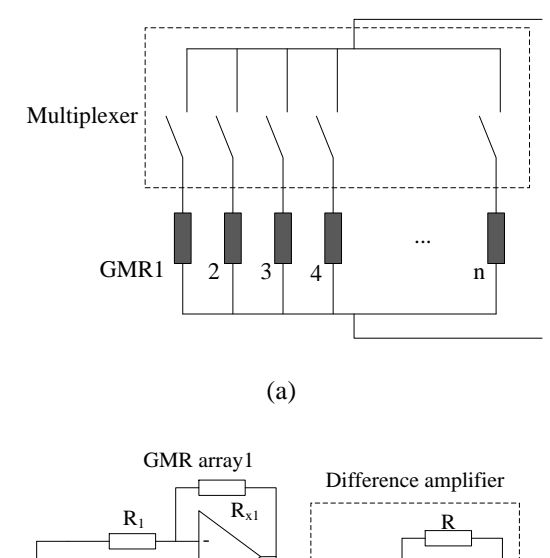


Figure 4.21. Design of the sensor board



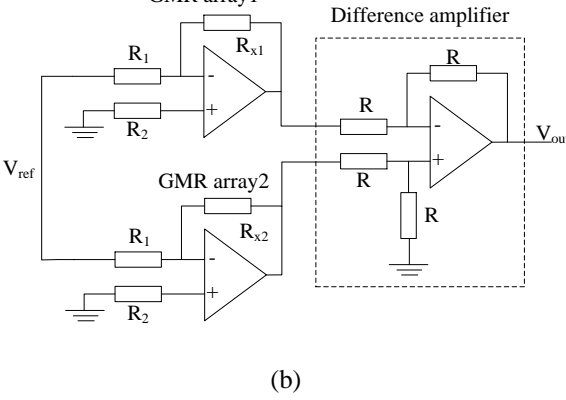


Figure 4.22. (a) Sensor connection diagram for each array (b) Circuit diagram of differential measurement probe

The sensors in each array are connected as shown in Figure 4.22(a). The GMRs are connected together at one end to a common line. The other end is connected to the port of a multiplexer. This offers the advantage of requiring only (n+ 1) wires for an n-sensor array. The two GMR arrays are then connected as shown in Figure 4.22(c). The output of the circuit is given by equation 4.39.

$$V_{out} = -\frac{V_{ref}}{R_1} (R_{x2} - R_{x1})$$
 4.39

The experimental system is shown in Figure 4.23. Two sinusoidal signals, with 90° phase difference were generated using a direct digital synthesis (DDS). These two signals were power amplified and connected to the orthogonal coils. A lock-in amplifier model RF840 from Stanford Research System was used to obtain the baseband signal with the best possible SNR. The output of the lock-in amplifier is

sampled and stored. The experimental measurements are obtained using a high resolution scanning system.

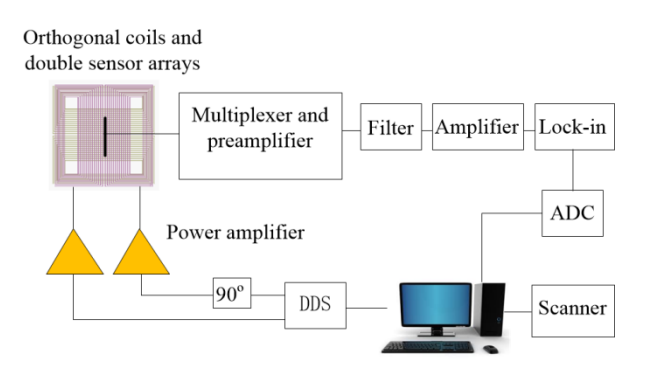


Figure 4.23. Schematic diagram of the experimental system.

Lateral view and top view of the sample are presented in Figure 4.24 (a) and (b) respectively. Notches were machined under the fastener head in the second layer of the sample. The depth of the notches is through the second layer. The width of the notches is about 0.15mm. The notches have different lengths (l_d): 0 mm, 6 mm, 8 mm and 12 mm.

The excitation currents in the orthogonal exciting coil were set at 100 mA at 200 Hz.

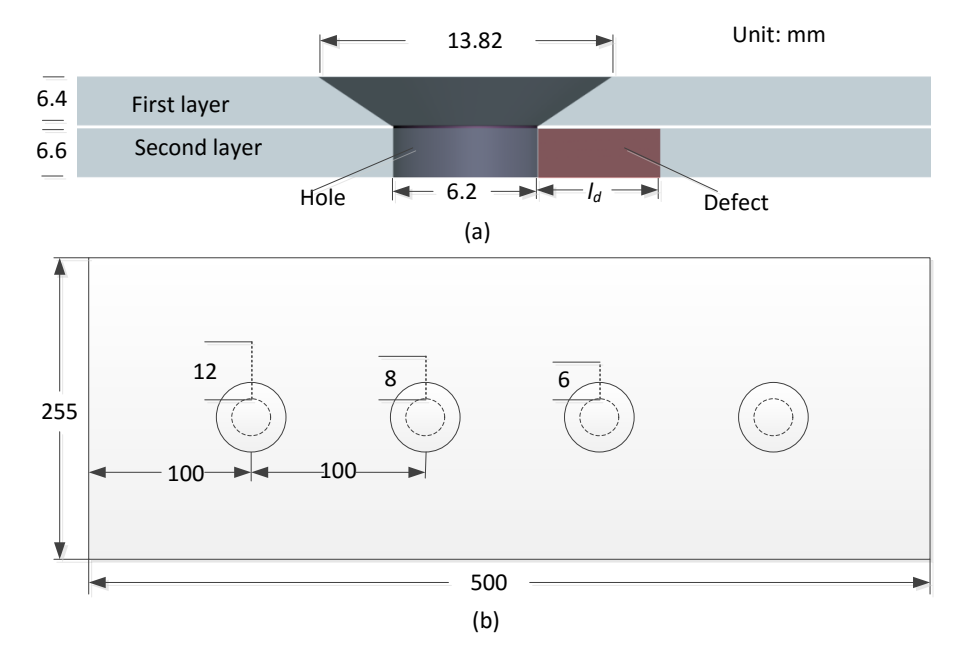


Figure 4.24. Lateral (a) and top (b) view of the two layers aluminum sample.

4.3.2 Inspection of Off-center Defect

The performance of the optimized probe design is evaluated by comparing it with the performance of conventional uniform distribution coil design. The fastener is located at x=20 mm off center of the coils' center. The experiment results of defect free fastener are shown in Figure 4.25. It is seen that the image of health fastener generated using the convention coil is distorted due to the non-uniform distribution of the eddy currents. The deformation coefficient ϵ is calculated and compared in Figure 4.26. For optimized non-uniform coil, ϵ is 6.75% for health fastener and increases to 18.8% for fastener with 6mm length defect. However, for conventional uniform coil, ϵ only change from 21.8% to 23.6% for health and defective fastener. The optimized coil has better defect detection capability compared with conventional uniform distribution coil.

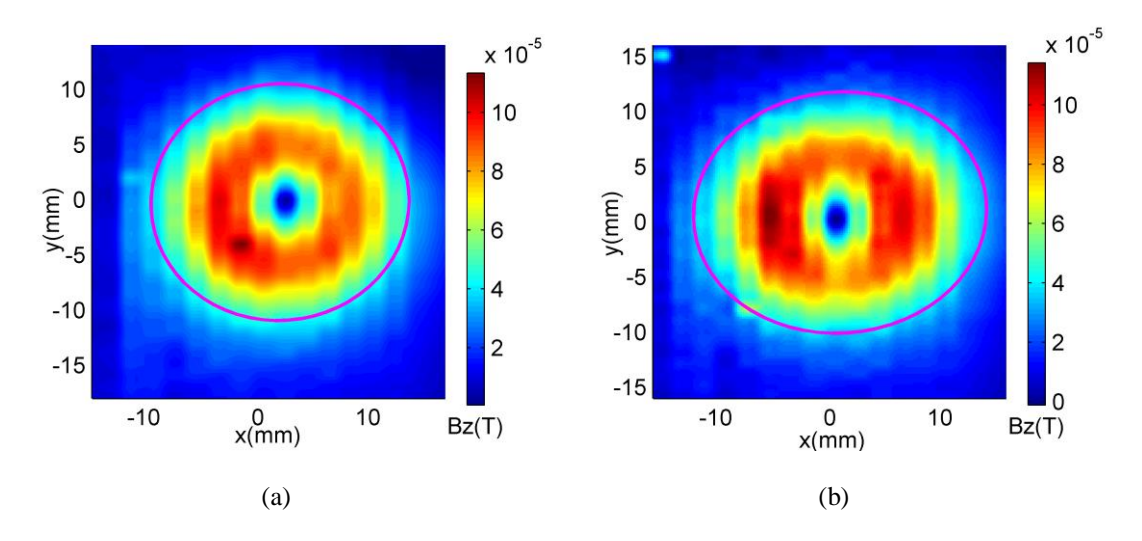


Figure 4.25. Experiment results of non-defect fastener generated with (a) optimized non-uniform coil probe; (b) conventional uniform coil probe.

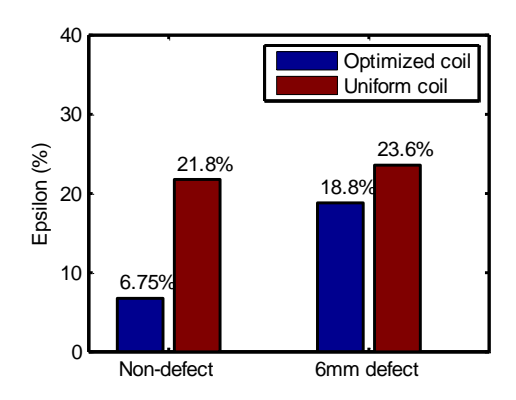


Figure 4.26. Comparison of experimental deformation coefficient ϵ of optimized coil and conventional uniform coil.

4.3.3 Effect of Defect Length

The experimental results of different length notches are shown in Figure 4.27. The image is distorted when a defect is present in the specimen. Deformation coefficient ϵ defined in equation 4.38 was calculated to quantify the distortion introduced by the presence of a crack. The result shown in Figure 4.28 was obtained by setting threshold v equal to 30% of the peak value. Using this threshold, we obtained an average radius $r_0 = 12.5 \, mm$, where the hole radius is 6.5mm. The deformation coefficient for different crack lengths is plotted in Figure 4.28. The distortion coefficient is positively correlated with crack length as expected.

However, several issues relating to differences in the response of the sensor elements in the array still need to be addressed: sources of mismatch include differences in sensitivity and bias point of sensor elements and differences in the orientation/position of the sensor when they are soldered on the board. These problems can be addressed by fabricating the probe with better tools and using a calibration procedure via post processing software.

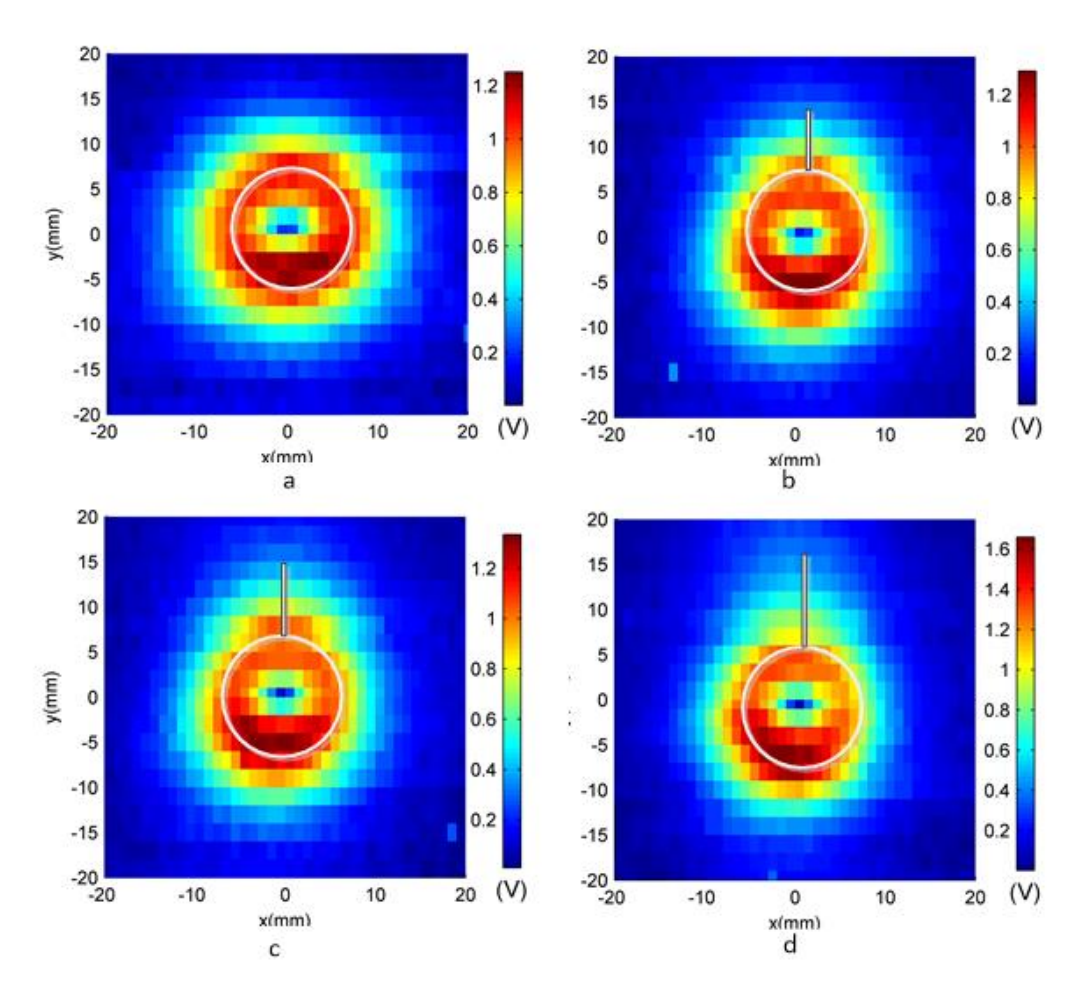


Figure 4.27. Experimental results with different crack lengths $l_{\rm d}$: (a) 0 mm,(b) 6 mm, (c) 8 mm and (d) 12 mm.

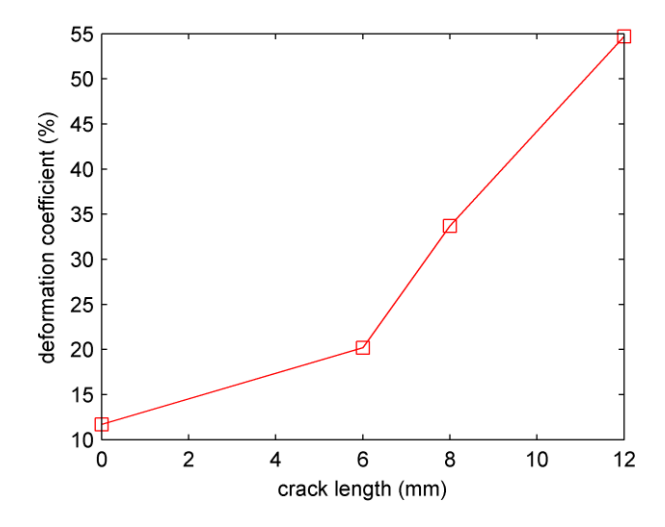


Figure 4.28. Deformation coefficient ϵ as a function of crack length

4.3.4 Effect of Crack Orientation

Cracks of different orientations are inspected with the prototype probe and the results are presented in this section. The sample is rotated through different angles relative to the probe. The experimental results are presented in Figure 4.29. Contours obtained by setting v equal to 30% of the peak value are plotted in Figure 4.30(a). The deformation coefficients are calculated using a procedure similar to the one described in section 4.3.2. The result is shown in Figure 4.30(b). From these results, it is seen that the probe can detect cracks in different orientations.

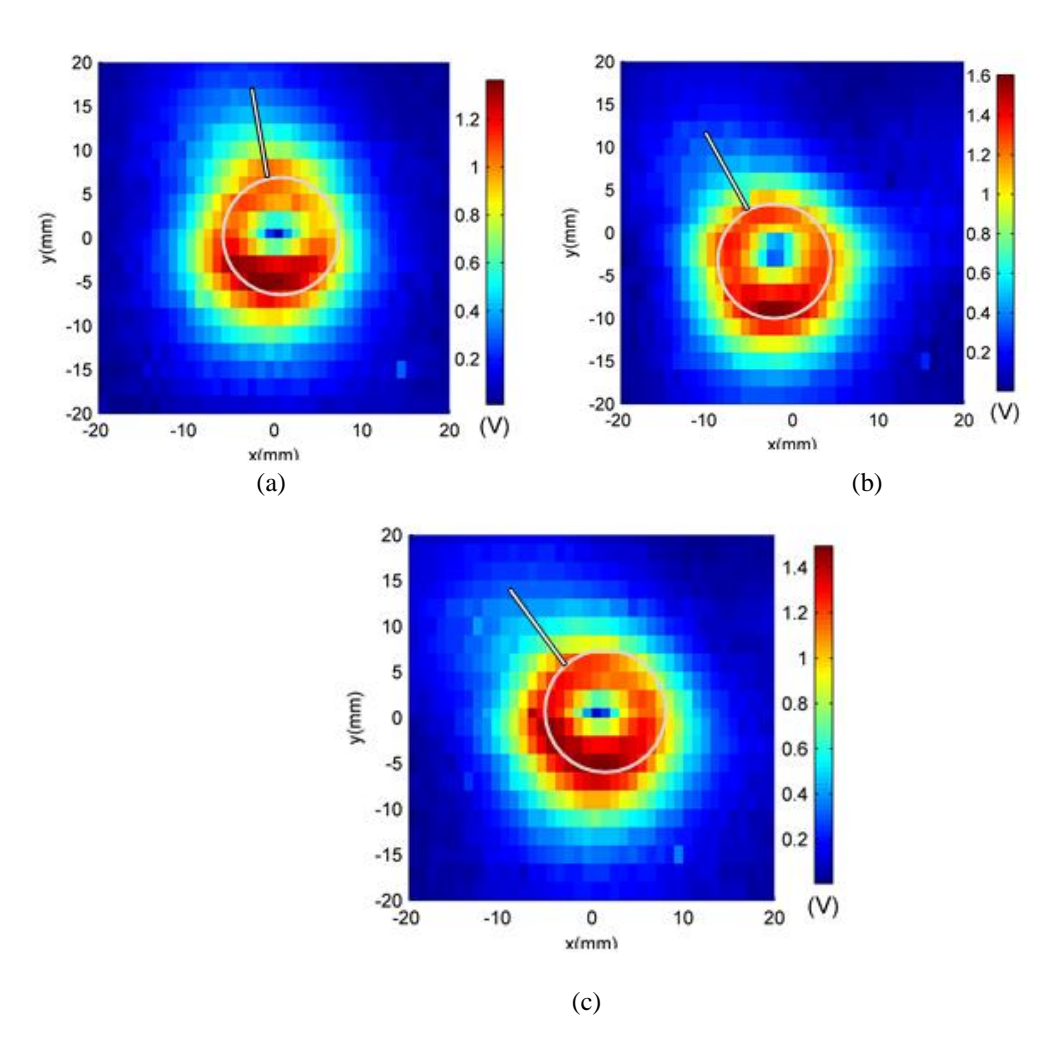


Figure 4.29. Experimental results with different crack orientation α (a) 15°,(b) 30°,(c) 45°.

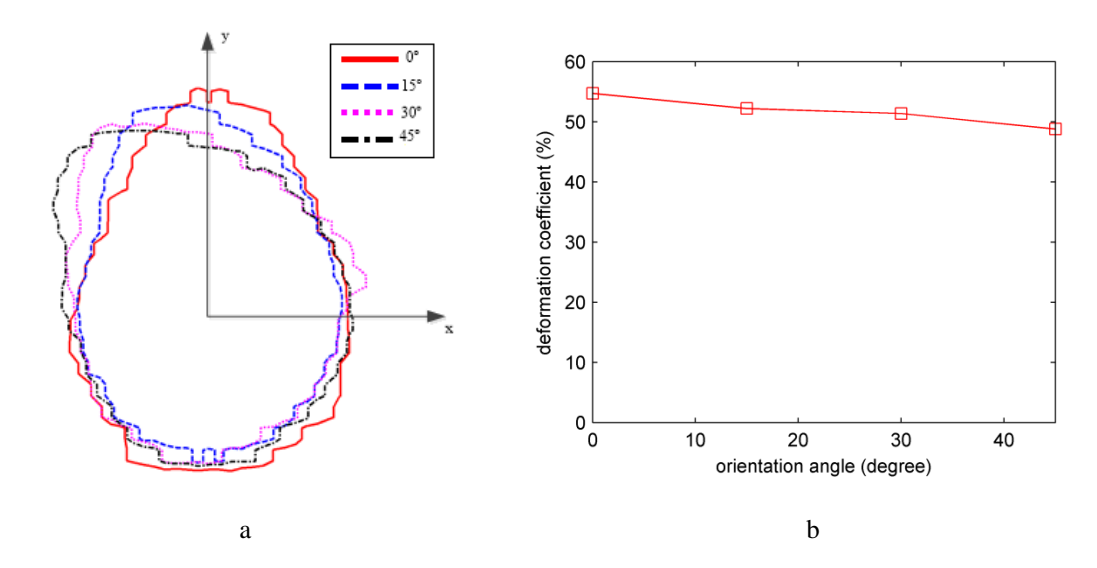


Figure 4.30. (a) Contour plot obtained with threshold value set at 30% peak value for different crack orientation angles (b) deformation coefficient ϵ as a function of crack orientation angle.

4.4 Conclusion

RoC-GMR probe with array sensors for multilayer structure inspection was presented in this chapter.

Differential measurements from two strategically positioned GMR sensor arrays were employed to eliminate the background fields generated by rotating excitation current. The current distribution of the excitation coil was optimized using polynomial approximation method to obtain uniform excitation field. A non-uniform coil design was derived from the optimized current distribution.

The probe performance is analyzed both numerically and experimentally. Simulation results, using both optimized coil and conventional coil, were acquired using FEM model. For conventional uniform coil, subsurface defect located near the coil edge is detected with a much weaker response as compared to the signal produced located at the coil center. However, the signal magnitude for optimized non-uniform coil is seen to be more robust with respect to offset of defects from coil center. For inspection of defect located under fastener site, the distortion coefficient of optimized coil is greater

than that of uniform coil when the fastener and defect is misaligned with the coils center.

Experimental results obtained from cracks of varying lengths show that cracks as short as 6mm under fastener site is detected by the probe. Experimental results from cracks of different orientation angle reveal that the probe can detect cracks irrespective of their orientation. The signal to noise ratio (SNR) in the experimental result without differential measurement is 5.79. The average SNR is increased to 33.46 by using differential measurement method. The differential scheme reduces the impact of the background field and increases SNR.

Chapter 5 Inspection of Steel Fasteners

5.1 Introduction

In most airframe structures composed of multiple layers that are riveted, rivets or fasteners are frequently made of steel which are magnetically permeable. The presence of steel fastener presents special challenges for inspection of cracks buried under the fastener head. First, steel fastener has relative permeability greater than 1 and hence steel fasteners behave as a strong discontinuity and a strong AC magnetic field is generated at the fastener. This strong signal can mask any indications from a defect. Secondly, the linear operation range of MR sensor often is too small to measure samples with ferromagnetic parts. Since fields at a steel fastener are strong and lie in the nonlinear part of MR sensor characteristic. Thirdly, the steel fastener could be magnetized resulting in a strong remanence that poses an additional bias. A strong DC magnetic field from the remanence of the magnetized steel fastener can shift the bias point of MR sensor, consequently distort the measurements or even saturate the sensor. Fourth, the permeability of steel fastener is not a constant, as it can vary with the frequency of the field applied, temperature, stress and residual stress etc.[74][75][76][77][78]. In a nonlinear medium, the permeability depends on the strength of the magnetic field. As a result, the permeability of the fastener can be anisotropic.

The following section presents the study and analysis of the effect of magnetic anisotropy effects in the steel fastener. This chapter also proposes a novel scheme, namely, magnetic balance measurement method to keep the bias point constant and extend the linear operation range of the MR sensor.

5.1.1 Properties of Ferromagnetic Materials

In order to describe the magnetic properties of materials, one must know the magnetic flux density \mathbf{B} , the magnetic field intensity \mathbf{H} , and the intensity of magnetization \mathbf{M} . These quantities are related by [79]

$$\mathbf{B} = \mu_0(\mathbf{H} + \mathbf{M}) \tag{5.1}$$

where μ_0 is the permeability of free space. M is a complex function of H[80]–[83].

$$M = \chi H \tag{5.2}$$

where χ is magnetic susceptibility. Then

$$\mathbf{B} = \mu_0 (1 + \chi) \mathbf{H} = \mu_0 \mu_r \mathbf{H}$$
 5.3

where μ_r is relative permeability. Relative permeability is a scalar if the medium is isotropic or a second rank tensor for an anisotropic medium. A typical magnetization curve of ferromagnetic material is shown in Figure 5.1.

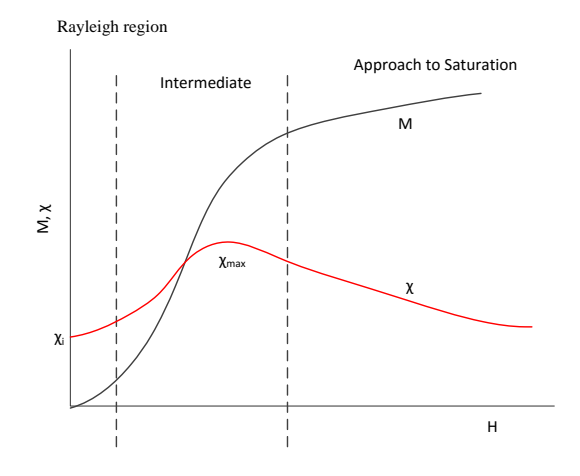


Figure 5.1. Magnetization curve for ferrimagnets and corresponding magnetic susceptibility.

Magnetic susceptibility can vary with position in the material, the frequency of the field applied, temperature, and stress etc. [84],[85], [86]. Typically ferromagnetic materials are nonlinear, e.g. the permeability depends on the strength of the magnetic field. Further permeability as a function of frequency can take on real or complex values[87]–[89].

5.1.2 Rayleigh Relations

The region where the magnetic fields are weak compared to the coercive force is called Rayleigh region, as shown in Figure 5.1. In the Rayleigh region, magnetization **M** is expressed as a quadratic function of the applied field **H**[76], [90], [91]:

$$\mathbf{M} = \chi_i \mathbf{H} + \alpha \mathbf{H}^2 \tag{5.4}$$

where χ_i is initial magnetic susceptibility, α is Rayleigh constant. This phenomenon was first investigated by Lord Rayleigh and the function is called first Rayleigh relation[92]. The second Rayleigh relation postulates the validity of a quadratic function of H also for the expression of the ascendant and descendant branch of a hysteresis loop with cusp point at (H_m, M_m) and $(-H_m, -M_m)$, respectively

$$M = (\chi_i + \alpha H_m) H \mp \frac{\alpha}{2} (H_m^2 - H^2)$$
 5.5

with the negative sign of the quadratic term characterizing the ascendant branch.

5.1.2.1 3D Rayleigh Relations

Imagine a cubic body of a magnetic medium with its edges parallel to the axes of a Cartesian coordinate system, as illustrated in Figure 5.2. If an external magnetic field is applied, say parallel to the y-axis, it induces a magnetization that in general is not aligned parallel to the external magnetic field, but contains components of cross magnetization.

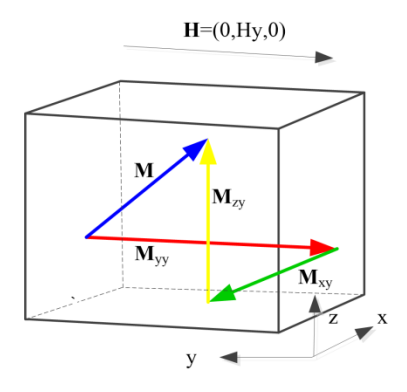


Figure 5.2. Cross-magnetization components M_{xy} and M_{zy} induced in an anisotropic medium by an applied magnetic field along the y-direction[92].

$$M_{XY} = \chi_{iXY}H_Y + \alpha_{XY}H_Y^2$$
 5.6

$$M_{YY} = \chi_{iYY}H_Y + \alpha_{YY}H_Y^2$$
 5.7

$$M_{ZY} = \chi_{iZY}H_Y + \alpha_{ZY}H_Y^2$$
 5.8

Generally speaking,

$$M_{jk} = \chi_{ijk} H_k + \alpha_{jk} H_k^2$$

$$5.9$$

with $j, k \in \{x, y, z\}$. Suppose :

$$\bar{\bar{\alpha}} = \begin{bmatrix} \alpha_{XX} & \alpha_{XY} & \alpha_{XZ} \\ \alpha_{YX} & \alpha_{YY} & \alpha_{XZ} \\ \alpha_{ZX} & \alpha_{ZY} & \alpha_{ZZ} \end{bmatrix}$$
 5.10

$$\bar{\bar{\chi}}_i = \begin{bmatrix} \chi_{i_{XX}} & \chi_{i_{XY}} & \chi_{i_{XZ}} \\ \chi_{i_{YX}} & \chi_{i_{YY}} & \chi_{i_{XZ}} \\ \chi_{i_{ZX}} & \chi_{i_{ZY}} & \chi_{i_{ZZ}} \end{bmatrix}$$
 5.11

Then

$$\overline{\overline{M}} = \overline{\overline{\chi}}_i \overline{\overline{H}} + \alpha \overline{\overline{H}}^2$$
 5.12

Where

$$\overline{\overline{H}} = \begin{bmatrix} H_x & 0 & 0 \\ 0 & H_y & 0 \\ 0 & 0 & H_z \end{bmatrix}$$
 5.13

Also, consider Relay hysteresis:

$$M_{jk} = (\chi_{ijk} + \alpha_{jk} H_{km}) H_k \mp \frac{\alpha_{jk}}{2} (H_{km}^2 - H_k^2)$$
 5.14

And

$$\overline{\overline{M}} = (\overline{\overline{\chi}}_{i} + \alpha \overline{\overline{H}}_{m})\overline{\overline{H}} \mp \frac{1}{2}\alpha (\overline{\overline{H}}_{m}\overline{\overline{H}}_{m} - \overline{\overline{H}}\overline{\overline{H}})$$
5.15

where

$$\overline{\overline{H}}_{m} = \begin{bmatrix} H_{x_{m}} & 0 & 0\\ 0 & H_{y_{m}} & 0\\ 0 & 0 & H_{z_{m}} \end{bmatrix}$$
 5.16

Considering these empirically verifiable relationships, it follows that both the initial susceptibility, Rayleigh constant and external magnetic field have to be interpreted as components of the magnetic susceptibility tensor.

5.1.3 Geomagnetic Field

The effects of geomagnetic field need to be considered for weak magnetic field measurement. The magnitude of geomagnetic field at the earth's surface ranges from 25 to 65 microteslas [93], [94]. The field exists all over the earth's surface and all the time.

At the location of the lab where this research was done (East Lansing, Michigan, USA) as an example, the earth's magnetic field is as shown in Table 5.1 [95]. The effect of geomagnetic field to EC-GMR inspection result will be studied later showing that its effect is inevitable.

Table 5.1. Earth's magnetic field at East Lansing, Michigan, USA

North component (T)	East component (T)	Vertical component (T)	Total field (T)
1.862×10^{-5}	2.108×10^{-6}	5.083×10^{-5}	5.418×10^{-5}

5.2 Effect of Magnetic Anisotropy

Consider the 3D Rayleigh relationships introduced in section 5.1.2. It follows that both the initial susceptibility, Rayleigh constant and external magnetic field have to be interpreted as components of the magnetic susceptibility tensor. If there is external magnetic field along one direction, then the fastener could become anisotropic.

5.2.1 C-scan Image of Anisotropic Fastener--Simulation

FEM model is used to understand the operation of RoC-GMR probe when an anisotropic fastener was involved. Models that allow scanning the excitation source coil above the fastener area would require significant computing time. In order to simplify the model in this study, the planar coil is approximated as an infinite sheet current which produces a uniform magnetic field with uniform eddy currents induced over the whole sample. This approximation has small error compared with the simulation of the actual planar coil, while eliminating the need for scanning. A C-scan image is thereby obtained from a single FEM calculation [68].

A two layer aluminum lap-joint geometry with steel fastener as shown in Figure 5.3 is considered. A radial notch of length l_d spans the thickness of the second layer. l_d equal zero implies that the fastener is defect free. The crack orientation is at an angle α with respect to the x-axis. The material properties used in the model are specified in Table 5.2.

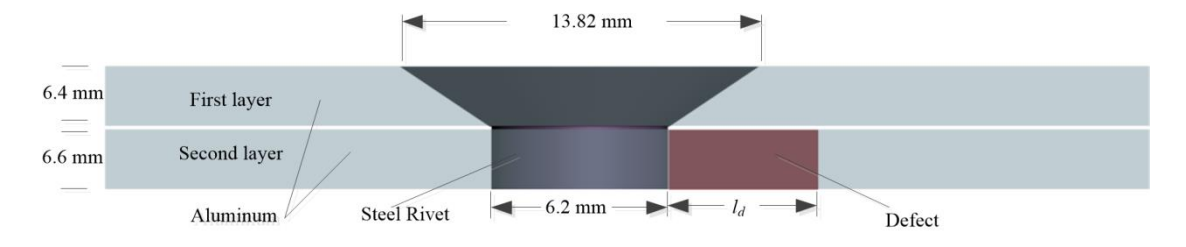


Figure 5.3. Lateral view of the 3D model and geometry parameters

Table 5.2. Material properties of the 3D FEM model

	Conductivity (S/m)	Relative permittivity	Relative permeability
Aluminum plate	2.326×10^{7}	1	1
Steel Fastener	1×10^{7}	1	Tensor

The model assumes that the permeability of the steel fastener is a 2^{nd} rank tensor that has form as given by equation 5.17. If $\mu_H = 0$, the fastener is isotropic with scalar permeability μ_i , otherwise the fastener is anisotropic. Here, the permeability is

assumed to be symmetric to the diagonal axis to achieve good convergence properties during calculation.

$$\mu_r = \begin{bmatrix} \mu_i & \mu_H & 0\\ \mu_H & \mu_i + \mu_H & \mu_H\\ 0 & \mu_H & \mu_i \end{bmatrix}$$
 5.17

The exciting currents in x and y directions are identical in amplitude and frequency but 90° apart in phase to produce rotating current excitation. The frequency was 100 Hz, and current density was 1000 A/m. The simulation results of a health fastener with $\mu_i = 2$ and different μ_H are presented in Figure 5.4.

The images of the healthy fastener are not perfectly circular when the fastener is anisotropic. Deformation coefficient ϵ defined in equation 4.38 was calculated to quantify the distortion of the imagies. Deformation coefficient ϵ as a function of μ_H is presented in Figure 5.5. The result was obtained by setting v equal to 30% of the peak value of isotropic fastener.

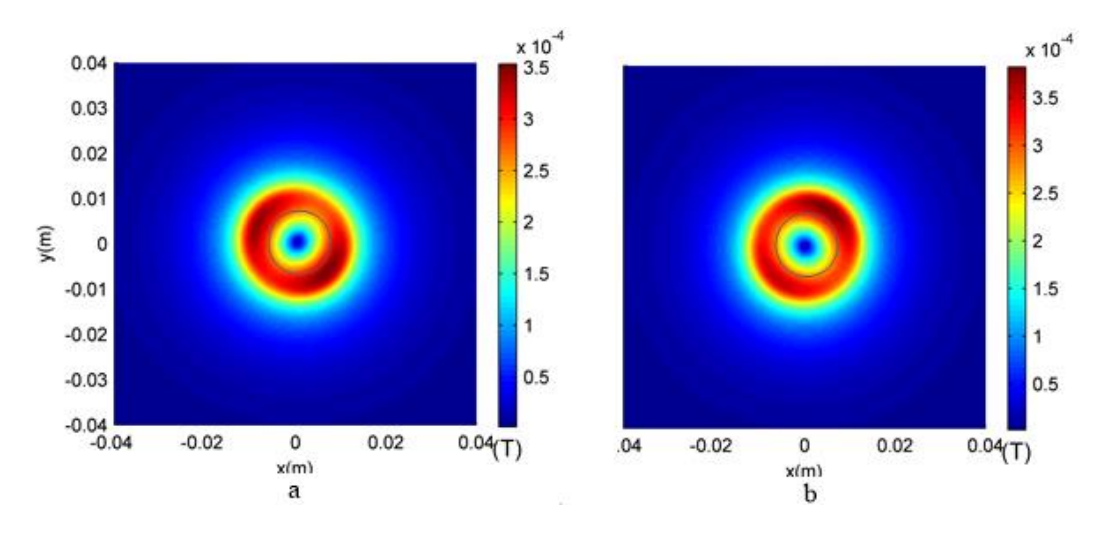


Figure 5.4. Simulation result of anisotropic non-defect steel fastener with rotating current excitation. The permeability tensor: $\mu_i=2$, (a) $\mu_H=-0.2$, (b) $\mu_H=0.2$.

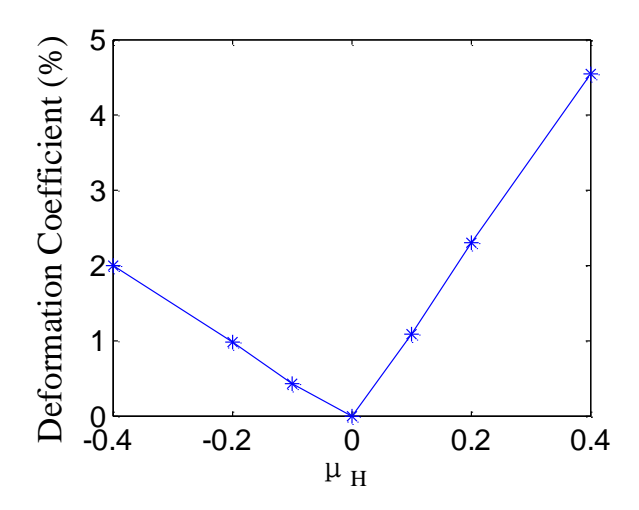


Figure 5.5. Deformation coefficient ϵ as a function of μ_H of anisotropic fastener

The distortion caused by anisotropic fastener interacts with the defect signal if there is defect present. Figure 5.6 presents simulation results of anisotropic steel fastener with defects at different radial orientations. The permeability of the fastener is modeled by the tensor as shown in equation 5.17 with $\mu_i = 2$, $\mu_H = 0.2$. The defect length (l_d) is 12mm. Due to the presence of anisotropy fastener, the signal become orientation dependent.

The deformation coefficient of anisotropic fastener and 12mm defect as a function of defect orientation angle is presented in Figure 5.7, which is smallest when defect located at 135 °.

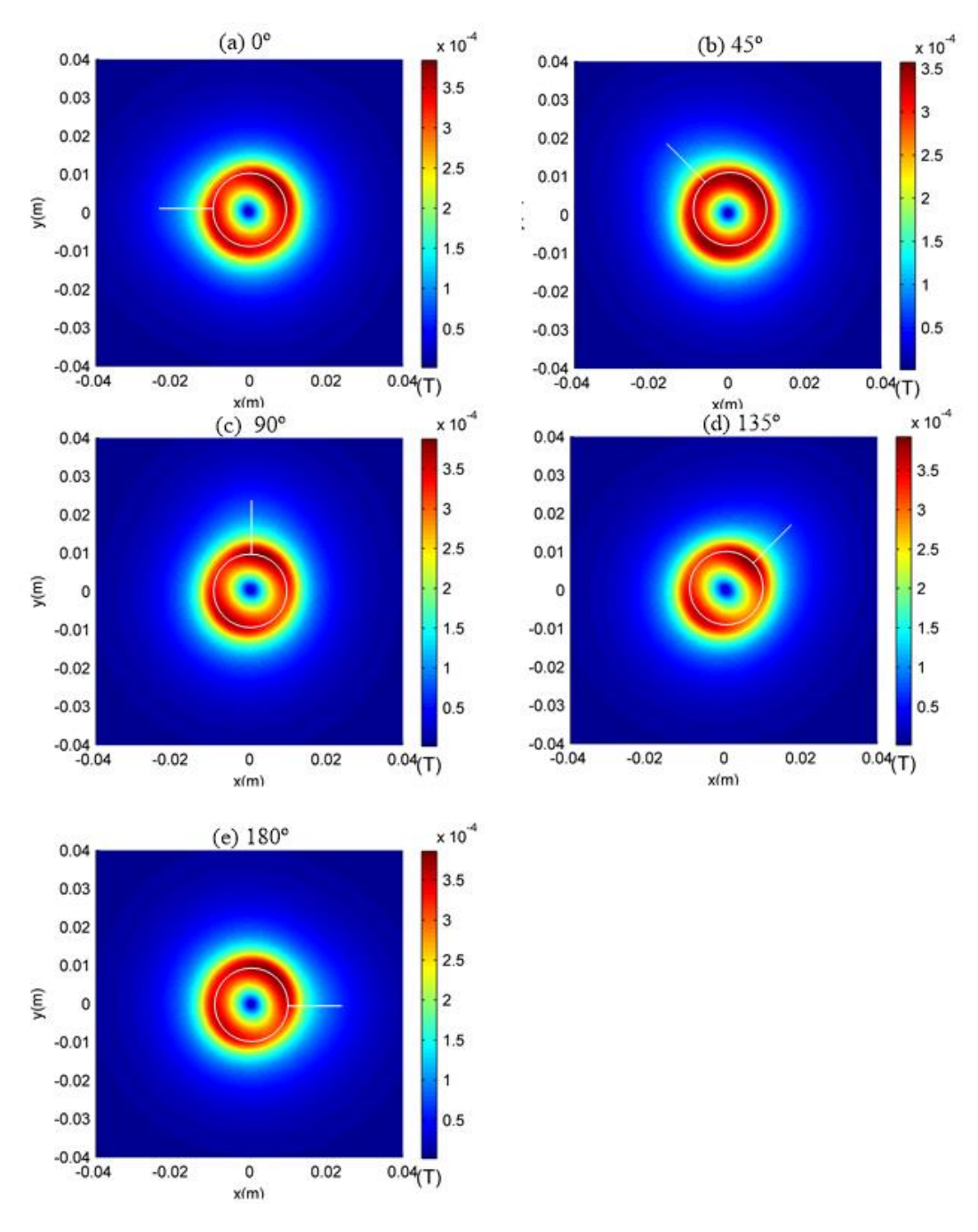


Figure 5.6. Simulation result of anisotropic steel fastener with 12mm defect heading (a) 0° , (b) 45° , (c) 90° , (d) 180° . The fastener and the defect are marked by white line in the image.

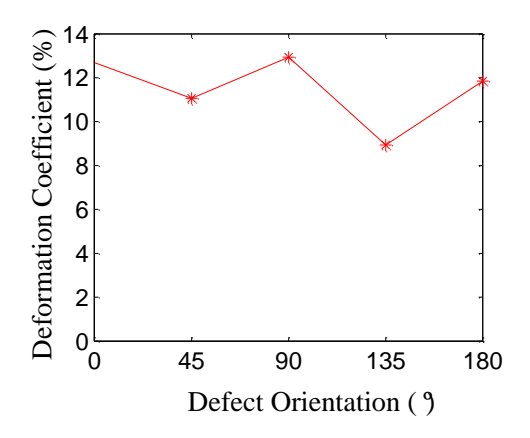


Figure 5.7. Simulation result: deformation coefficient ϵ of anisotropic fastener and 12mm defect as a function of defect orientation.

5.2.2 Experimental Measurement with External DC Field

As discussed in section 5.1.2, the magnetic susceptibility is a function of external magnetic field. The effect of low-field dependent variation of magnetic susceptibility on the inspection of multilayer structure with steel fastener was studied experimentally by applying an external DC magnetic field to the steel fastener.

A DC magnetic field in y-direction is simulated by a DC current in an x direction coil, as shown in Figure 5.8. As the sensors are located on the symmetry line of the x direction coil the normal component magnetic field (Bz) is theoretically zero and hence the external DC field produced by the DC current does not change the bias point of the GMR sensors

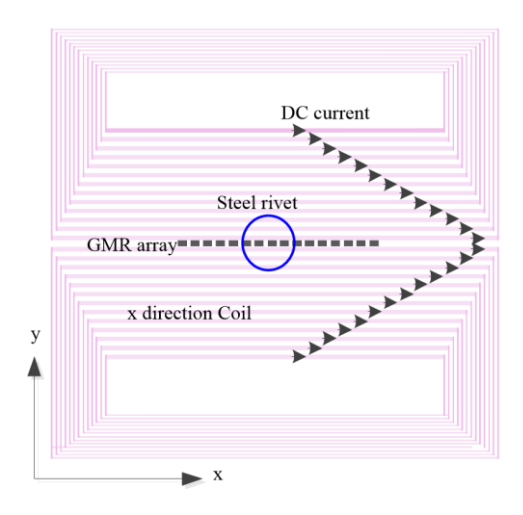


Figure 5.8. DC current in an x direction coil to generate y direction DC magnetic field.

DC currents of different amplitudes were applied in the coil and the steel fastener was exposed to the DC field was scanned using the prototype RoC-GMR probe. The experimental results from a healthy fastener are presented in Figure 5.9. When positive DC current was applied, the right hand side signal become stronger. Conversely, when negative current was applied, the left hand side signal become stronger.

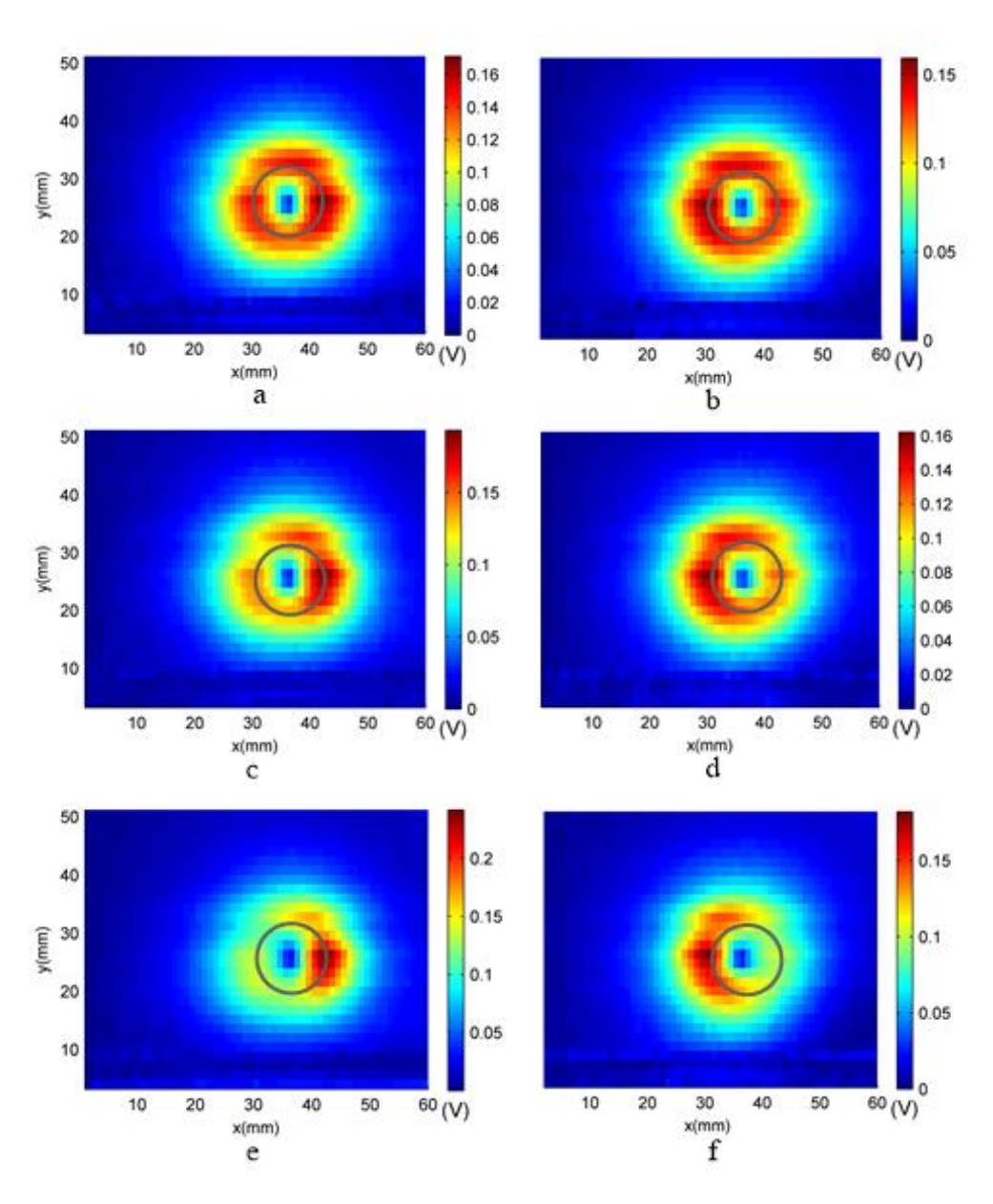


Figure 5.9. Experimental results of healthy steel fastener with additional DC current (a) 0.25A, (b) -0.25A, (c) 0.5A, (d) -0.5A, (e) 1A, (f) -1 A, in the x direction coil.

These experimental results are comparable with the simulation results shown in previous section. It should be noted that the experiment measurements were also influenced by the geomagnetic field. The geomagnetic field has horizontal and vertical components and hence the material property of the steel fastener is much more complex than the material property used in the FEM model.

The experimental results presented in Figure 5.9 show that the effect of 0.25A and - 0.25A DC current in the x direction coil is visible. Meanwhile, it is calculated that 0.25A current in the coil generates 8.44×10^{-5} T horizon magnetic field 5 mm below the center of the coil in air, which is comparable with the geomagnetic field. The study clearly shows that the influence of geomagnetic field cannot be ignored.

5.2.3 Effect of Geomagnetic Field

The effect of geomagnetic field on image data from steel rivets using RoC-GMR probe is studied experimentally. The geometry dimensions of the test sample are as specified in Figure 5.3.

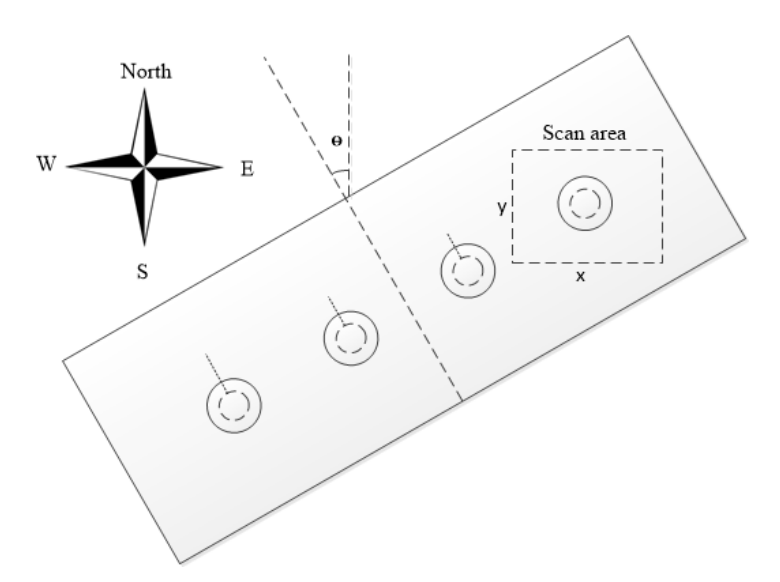


Figure 5.10. Top view of the test sample showing it is rotated by Θ in horizontal plane.

The sample, including the aluminum layers and the rivets, is rotated to different angles relative to the geomagnetic field and is scanned using the RoC-GMR probe, as shown in Figure 5.10.

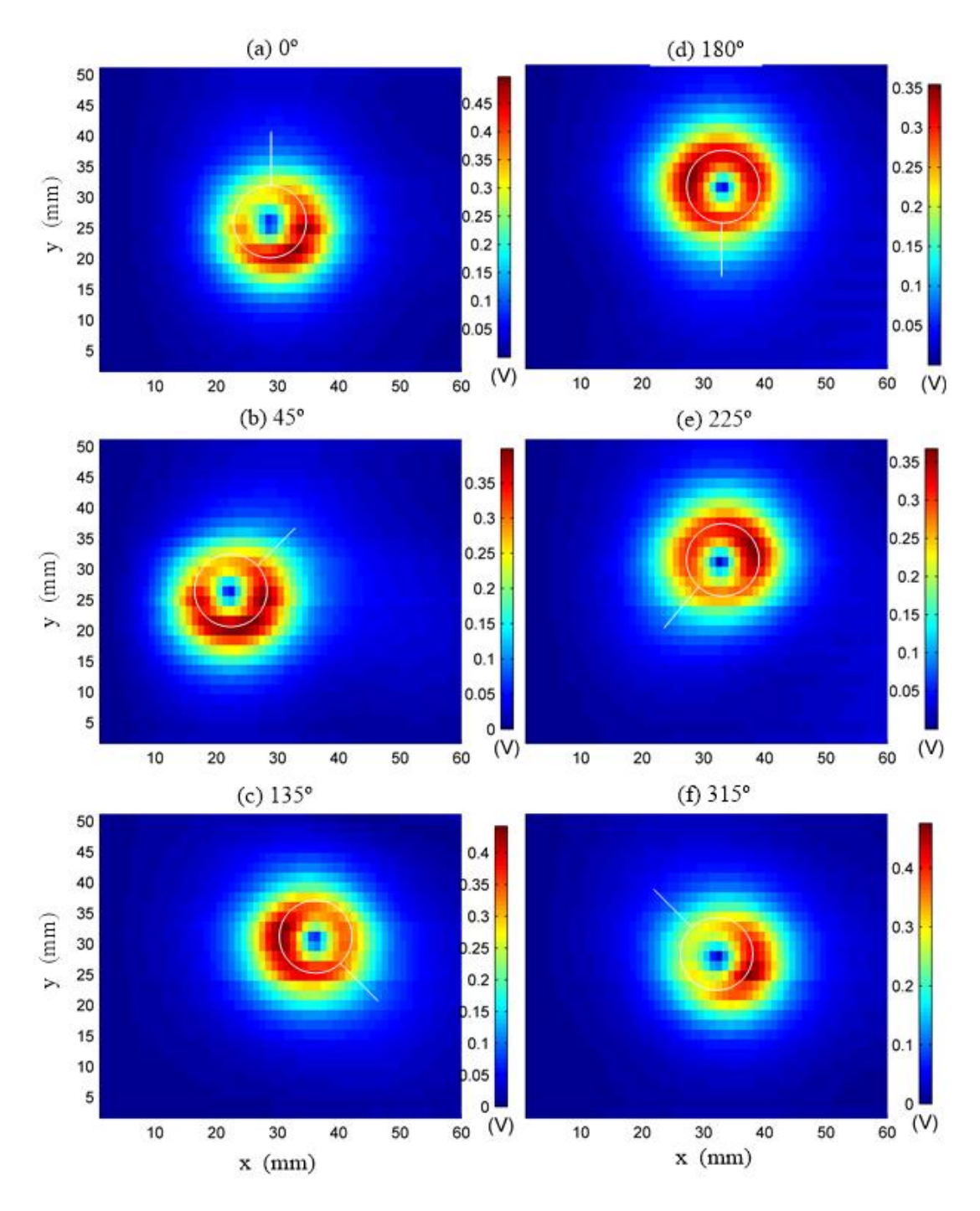


Figure 5.11. Experiment results of steel fastener with 12mm defect. The sample was rotated relative to the geomagnetic field in horizontal plane (a) 0 °, (b) 45 °, (c) 135 °, (d) 180 °, (e) 225 °, (f) 315 °.

The output data of the RoC-GMR probe from a steel fastener with $l_d=12mm$ defect are shown in Figure 5.11. The geomagnetic field influence with the induced fields

around the defect. Deformation coefficient ϵ of image data from a steel fastener and 12mm defect is plotted as a function of defect orientation in Figure 5.12. The coefficient is calculated with contours obtained by setting threshold v equal to 30% of the peak value of non-defect fastener. These results demonstrate that the RoC-GMR probe can detect defects under steel fastener at different orientations. However, due to the effect of geomagnetic field, the deformation coefficient is not constant.

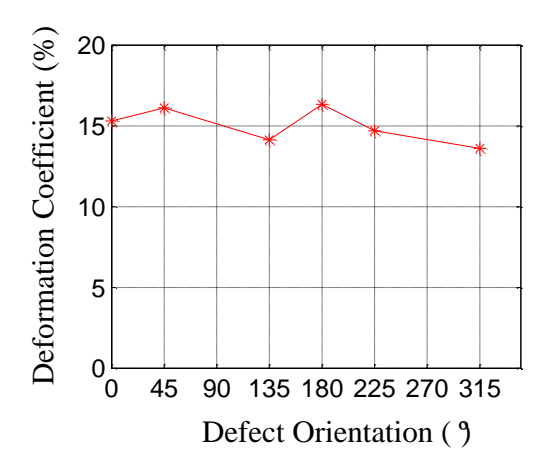


Figure 5.12. Experimental result: deformation coefficient ϵ of steel fastener and 12mm defect as a function of defect orientation.

5.3 Magnetic Balance Measurement Method

Another issue in the inspection of fastener sites is that the steel fastener may be magnetized resulting in a strong remanence. Strong residual magnetism can shift the work point of MR sensor outside of its linear range. Moreover, the limited dynamic range of MR sensor present challenges since the amplitude of the fastener signal is much greater than the defect signal. This section presents the study of magnetic balance measurement (MBM) method to make MR sensor's bias point constant, so as to eliminate the effect of strong external DC field.

5.3.1 Operating Principle

The schematic diagram of the MBM method is as shown in Figure 5.13(a). The output of the MR sensor is amplified and filtered and then feedback to a PID controller. The

low pass filter should be second order or higher. The output of the PID controller is amplified to drive a compensation coil, which generates magnetic field to balance the input magnetic field at the MR sensor position. Instead of measuring the sensor output, the input magnetic field is measured by recording the balance voltage/current of the compensation coil.

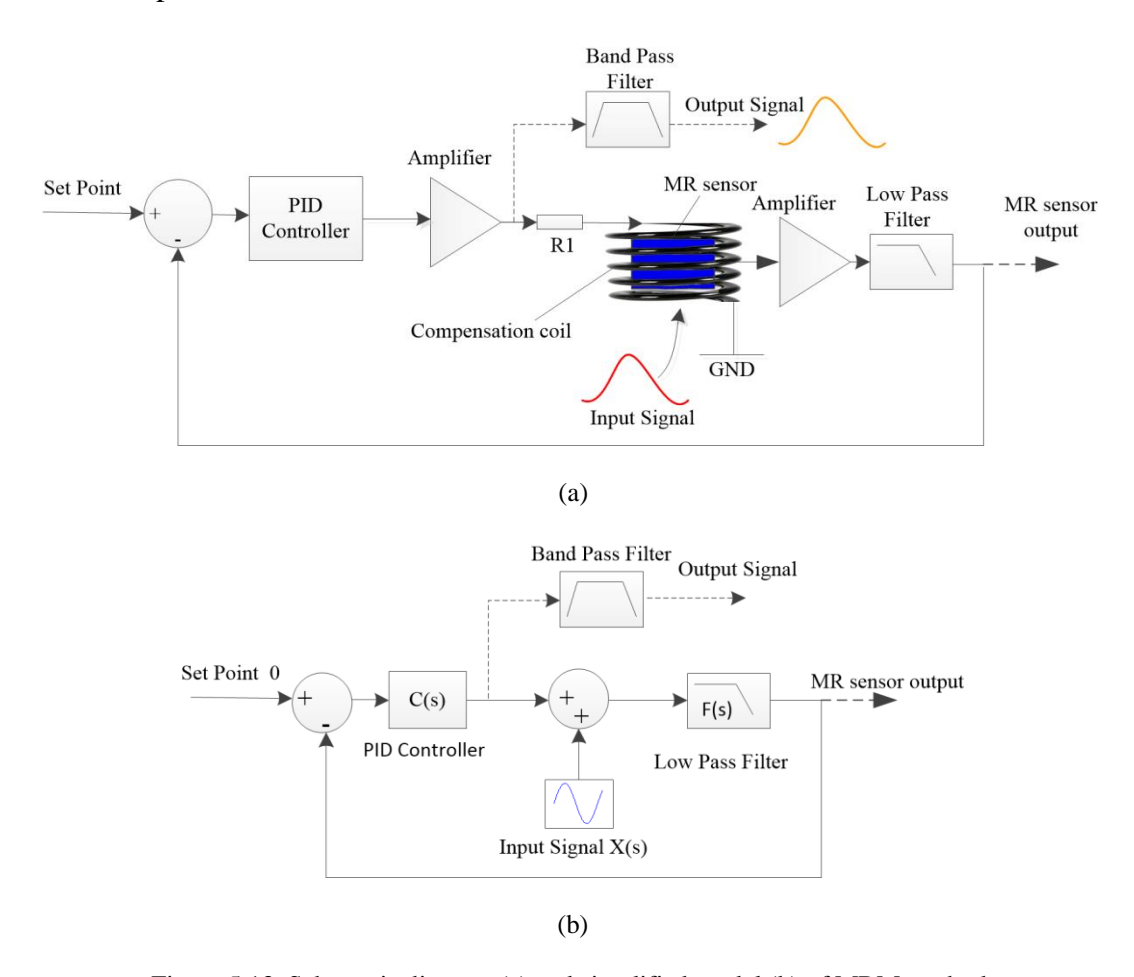


Figure 5.13. Schematic diagram (a) and simplified model (b) of MBM method.

The schematic diagram shown in Figure 5.13 (a) is simplified by a model presented in Figure 5.13 (b). The transfer function of the PID controller is given by equation 5.18.

$$C_{(s)} = K_p(1 + K_I \frac{1}{s} + K_D s)$$
5.18

where s is the complex number frequency in the Laplace transform, K_p the proportional gain, K_I the integral gain, K_D the derivative gain. The proportional term provides an overall control action proportional to the error signal. The integral term

reduces steady–state errors through low-frequency compensation by an integrator. The derivative term improves transient response through high-frequency compensation by a differentiator[96].

Assuming the Laplace transfer of the input signal is X(s), the transfer function of the low pass filter is F(s), the output of the MR sensor $(Y_{Sensor_{(s)}})$ and the output of the PID controller $(Y_{PID_{(s)}})$ is written as equation 5.19 and 5.20 respectively.

$$Y_{Sensor(s)} = \frac{X(s)F(s)}{1 + C(s)F(s)}$$
5.19

$$Y_{PID(s)} = -\frac{X(s)F(s)C(s)}{1+C(s)F(s)}$$
 5.20

At high frequency, e.g. frequency much higher than the cut off frequency (ω_c) of the low pass filter, $|F(j\omega)| \ll 1$, here j is imaginary unit, ω angular frequency. The output signals are small due to the low pass filter. At low frequency $(\omega < \omega_c)$, the gain of the low pass filter is considered constant, e.g. A_L . The output of the MR sensor and the PID controller is given by following equations in frequency domain.

$$Y_{Sensor(j\omega)} = \frac{A_L X(j\omega)}{1 + A_L C(j\omega)}$$
 5.21

$$Y_{PID(j\omega)} = -\frac{A_L X(j\omega)C(j\omega)}{1 + A_L C(j\omega)}$$
5.22

Choosing parameters to make $|A_LC(j\omega)| \gg 1$, from equation 5.21

$$Y_{Sensor(j\omega)} \approx \frac{X(j\omega)}{C(j\omega)}$$
 5.23

From equation 5.18 and 5.23, it is found that when $\omega \to 0$, $|C(j\omega)| \to \infty$. Consequently, $Y_{Sensor(j\omega)} \to 0$ which implies that the effect of static or very low frequency signal and the effect of remanence field of steel fasteners on the MR sensor is eliminated.

In the case of AC input signal, amplitude of variation of the sensor is reduced to $\left|\frac{1}{C(i\omega)}\right|$ times the amplitude of the input signal. Consequently the linear measurement

range of the MR sensor is extended by a factor of $|C(j\omega)|$ using this method as compared to using the MR sensor to measure the field directly.

Substituting $|A_LC(j\omega)| \gg 1$ into equation 5.22, the output of the PID controller is expressed by equation 5.24. The input signal is measured by measuring the PID controller output voltage without sacrificing the sensitivity of the MR sensor.

$$Y_{PID(j\omega)} \approx -X(j\omega)$$
 5.24

5.3.2 Effect of the Compensation Coil on Defect Signal

The MBM utilizes a compensation coil to generate magnetic field to balance the input field. The influence of using the compensation coil on the defect signal is estimated in this section.

Considering the compensation coil is a multi-turns circular coil, the magnetic field of the coil along the coil axis in air is calculated according equation 5.25[97].

$$B = \frac{\mu_0 N r^2 I}{2(a^2 + z^2)^{3/2}}$$
 5.25

where μ_0 is the permeability of air, N the number of turns of the coil, I the current in the coil, r the radius of the coil and z the axial distance from the center of the coil to observation point. Suppose the magnetic field at the center of the coil (z=0) is B_0 . Then equation 5.25 is re-written as equation 5.26.

$$B = B_0 \cdot \frac{1}{(1 + \frac{z^2}{r^2})^{3/2}}$$
 5.26

The magnetic field of circular coil drops rapidly as z increases. From equation 5.26, the magnetic field decreases to 0.44% of B_0 at z=6r. So the effect of the field of compensation coil can be ignored if defect is farther than 6r from the center of the compensation coil. Hence the compensation coil should be fabricated with small radius and located close to the MR sensor. The compensation coil can also be integrated inside MR sensor using micro-processing technology, in which case the

coil radius is of the order of micro meters. In the application considered in this thesis, the defect is embedded in subsurface layers; hence the small size (1.6mm) commercial MR sensor with compensation coil wound outside of the sensor is used.

5.3.3 Numerical Analysis

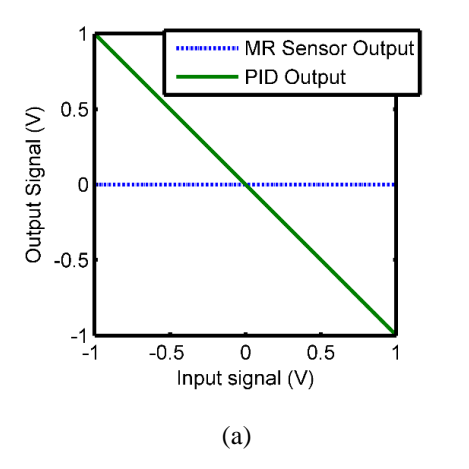
The operation of the MBM is mimicked numerically using Simulink of Matlab. K_p , K_i , K_d in the PID controller is 20,10,3e-6 respectively, which match the parameters used in the prototype that will be presented later. The low pass filter is a $2^{\rm nd}$ order filter with transfer function as specified in equation 5.27.

$$F_{(j\omega)} = \frac{1}{(\frac{j\omega}{\omega_c})^2 + \frac{j\omega}{Q\omega_c} + 1}$$
 5.27

where $\omega_c = 2\pi f$, f=1kHz, Q=0.5.

First, static response of the system is studied. The input signal changes from -1V to 1V with step size 0.1V and the output data are measured after it achieve steady state. The outputs of the PID controller and the MR sensor vs. the input signal are plotted in Figure 5.14(a). It is found that the MR sensor output is constantly zero, since the integral term in the PID controller reduces steady—state errors. The output of the PID controller is negatively linearly correlated with the input signal, which is recorded as measurement of the input signal.

Next, the response of the system to AC signal is calculated. The input signal is sinusoid signal with amplitude 1V, frequency 100Hz. The results are presented in Figure 5.14 (b). The amplitude of the MR sensor output signal is only 0.0476V, which is 4.76% of the input signal. This implies that linear measurement range of the MR sensor is extended more than 21 times, thereby extending the linear dynamic range. Similar to the steady-state response, the PID output is negatively linearly correlated with the input signal. The amplitude of the PID output is 0.953V.



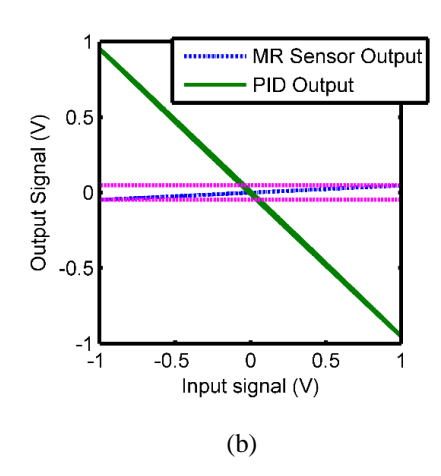
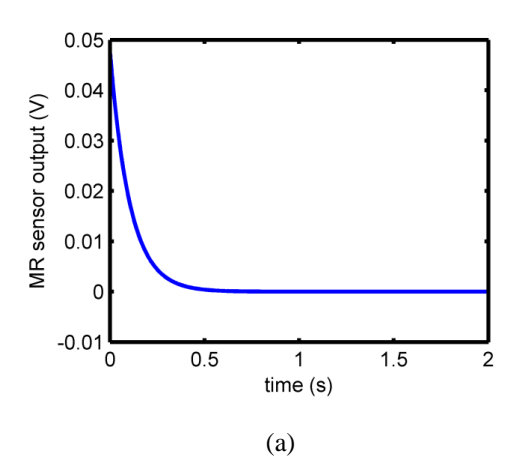


Figure 5.14. Numerical results of static (a) and AC 100Hz (b) outputs vs. input signal.

Next, the transient response to step input signal is simulated and the result is presented in Figure 5.15(a). The step signal is 0V initially and jumped to 1V at t=0s. It is seen that the MR sensor output becomes steady in about 0.5s which implies that the effect of external DC magnetic field on operation point of the MR sensor can be ignored after 0.5s.



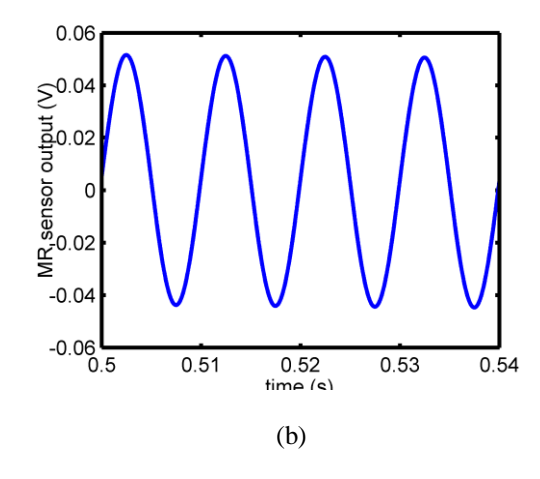


Figure 5.15. (a) Transient response of the MR sensor output to step input signal. (b) Time domain signal of the MR sensor output with input sinusoid signal of 1V amplitude, 100 Hz frequency and 10V DC bias.

Finally, to further illustrate the compensation effect of this method to external DC magnetic fields, a sinusoid AC signal of amplitude 1V, frequency 100 Hz and 10V DC bias is used as the input signal at t=0s. The MR sensor output from t=0.5s to t=0.54s is presented in Figure 5.15 (b). The effect of the strong DC bias is cancelled almost completely.

5.3.4 Experimental Validation of MBM

The operation of the MBM is validated and tested experimentally. The experiment setup is as shown in Figure 5.16. GMR sensor Model GF708 from Sensitec is used to build the prototype. The linear measurement range of the sensor is less than 0.5mT. The sensor is available as a bare die with gold terminals. This configuration offers small package size, allowing us to build a relatively small compensation coil.

The output of the GMR sensor is amplified 20 times by instrumentation amplifier AD620. A compensation coil is wound using 0.1mm diameter copper wire and the GMR sensor is located at the center of the coil. The number of turns of the compensation coils is 20. The radius of the coil is about 0.9mm. SRS SIM 960 analog PID controller from Stanford research system is used as the PID controller. The proportional gain of the PID controller is tuned to the maximum value without oscillation. K_i , K_d was 10 and 3e-6 respectively, which are tuned to achieve best performance of PID controller. The output of SIM960 is amplified by power amplifier Agilent 33502 and then connected to the compensation coil.

A Helmholtz coil is used to generate uniform magnetic field, which was measured by the MR sensor. The radius of the Helmholtz coils is R=90mm. The number of turns of the Helmholtz coils n=12 each. Magnetic field at the center of the Helmholtz coil is calculated according equation 5.28[98].

$$B = (\frac{4}{5})^{3/2} \frac{\mu_0 nI}{R}$$
 5.28

where *I* is current in the Helmholtz coils.

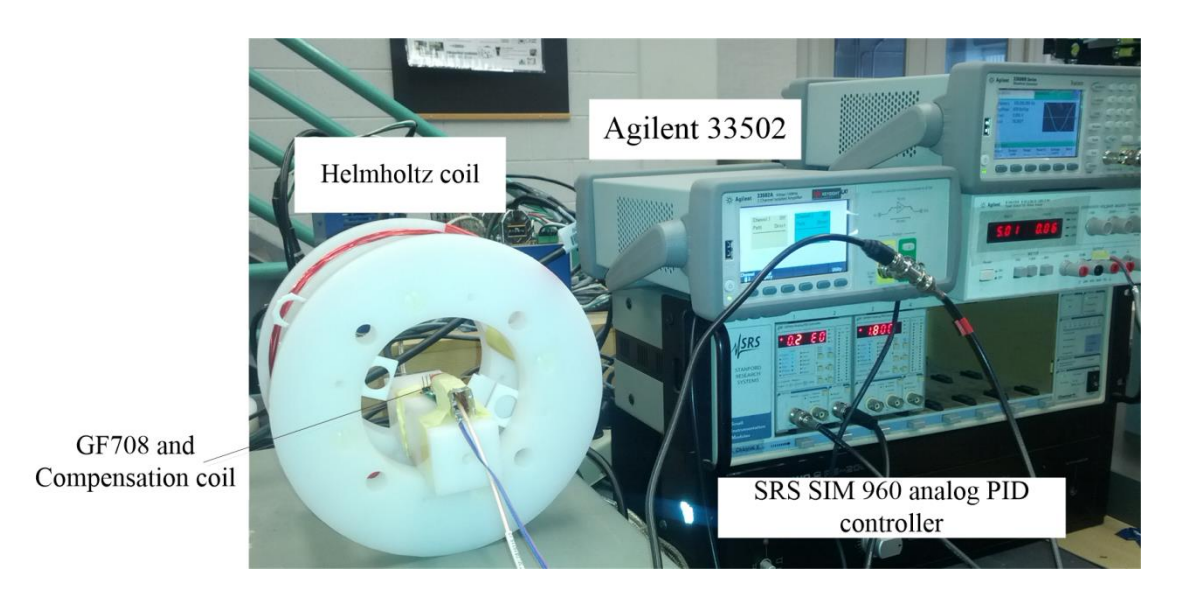


Figure 5.16. Experimental setup for measuring magnetic field

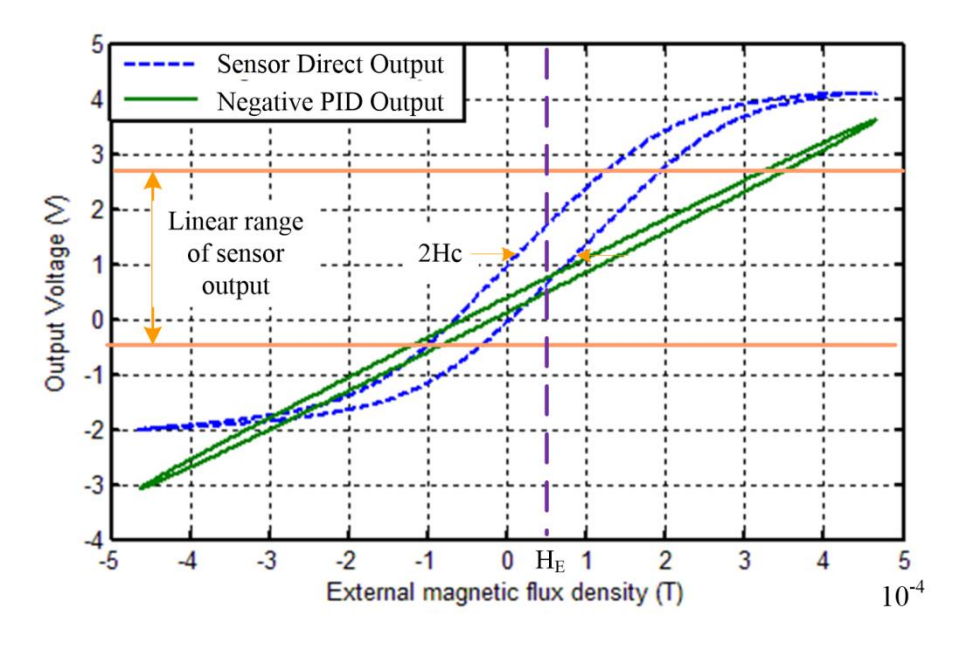


Figure 5.17. Experimental results of output voltage vs. magnetic flux density.

In order to evaluate the MBM method, the magnetic field of the Helmholtz coil is measured using GF708 directly and the proposed method. The results are presented in Figure 5.17. As shown in section 5.2, the MBM output is inversely proportional to the input signal; the negative output of the PID controller is plotted. Magnetic flux density of the Helmholtz coils is calculated according equation 5.28. It is found that the linear range of the sensor is about 2×10^{-4} T and the sensor is saturated with magnetic field greater than 4×10^{-4} T. However, the output of MBM method is

always in linear range when the magnetic flux density varied from -4.6×10^{-4} to 4.6×10^{-4} T. The linear measuring range of MBM method for DC signal is limited by the circuit saturation voltage ($\pm 9V$ in this experiment setup) which is much larger than the output signal range provided by the power amplifier. The coercive field (Hc) in the hysteresis as defined in Figure 5.17 was 3.47×10^{-5} T for the sensor.

5.4 Experimental Output Signal of Magnetized Steel Fastener

5.4.1 Experiment Setup

A prototype probe with MBM for inspection of multi-layer structure was fabricated and instrumented to test the performance of the proposed method. A schematic of the experimental system is shown in Figure 5.18(a).

Orthogonal coils as specified in section 4.2 were used for generating a rotating planar excitation current. The normal component of the magnetic flux density B_z at the center of the orthogonal coil was measured by a GMR sensor. As the sensor is located at the center of the coils, the measured signal is null field when there is no defect and has some perturbation when the symmetry is destroyed by presence of defect.

The experiment system can be configured to use MBM method or GF708 to measure B_z directly by means of the switch S1 and S2. If S1 is off and S2 is connected to contact 2, the compensation coil is disconnected and the output of sensor is connected to the amplifier directly, in which case, the field is measured by the GMR sensor directly. However, if S1 is on and S2 is connected to contact 1, the MBM system works and the signal is measured from the output of the PID controller. A lock-in amplifier model SR830 is used to obtain the baseband signal. The output of the lockin amplifier is transferred to a computer through RS232 cable and stored in the

computer. The experimental measurements are obtained using a high resolution scanning system.

A two-layer aluminum sample with a steel fastener and defect was tested. A schematic of the geometry of two-layer sample is shown in Figure 5.18(b), where l_d is the length of the radial crack ($l_d = 0$ for healthy fastener).

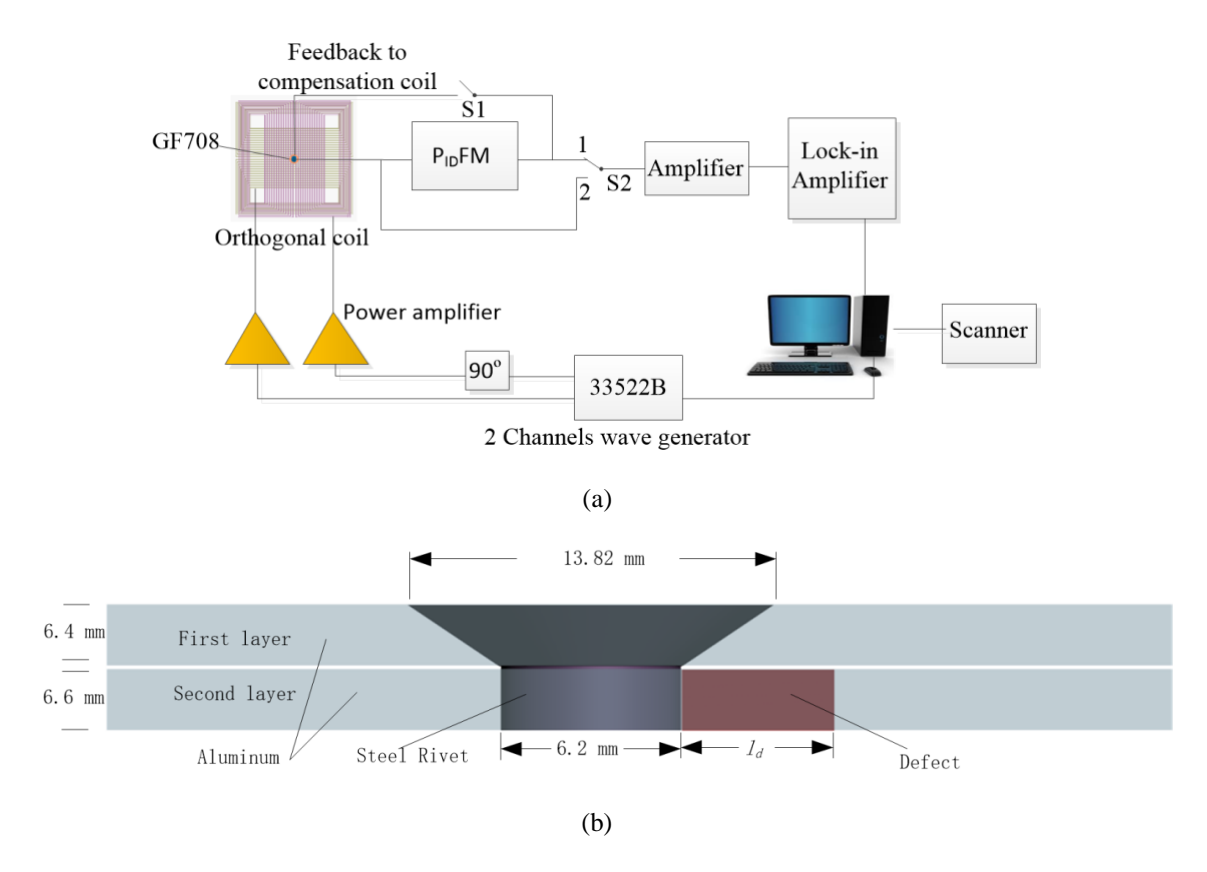


Figure 5.18. Experimental setup: (a) Diagram of experiment system (b) Side view of test sample.

5.4.2 Experimental Results and Analysis

The experimental measurements from a magnetized steel fastener without defect $(l_d = 0)$ are presented in Figure 5.19, where Figure 5.19 (a) was obtained using the GF708 sensor to measure B_z directly and Figure 5.19 (b) is obtained using MBM method. The circles in the images indicate the location of the head of the fastener. The excitation current of frequency 100Hz, amplitude 100mA was applied.

Image of a defect-free fastener should ideally be circular and distorted when a defect is present at the fastener site. However, the image is distorted due to the fastener magnetization if the GMR sensor is used to measure the field directly, as shown in Figure 5.19(a), which can result in a false call. The image obtained using MBM method is relatively more circular, as shown in Figure 5.19 (b).

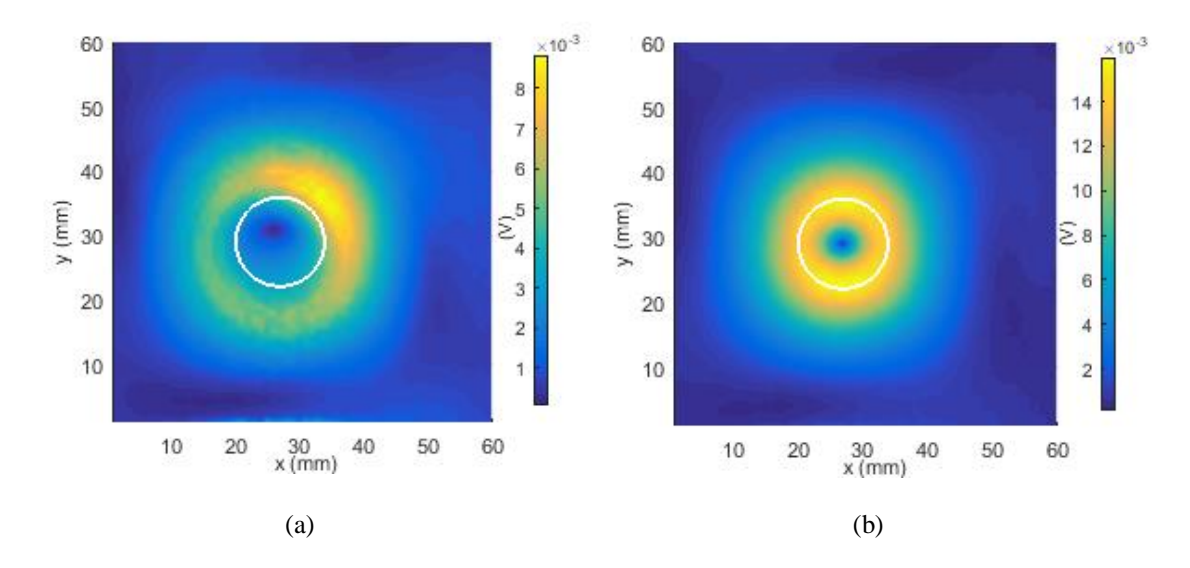


Figure 5.19. Experimental results of defect free magnetized fastener ($l_d = 0$) obtained using GF708 to measure Bz directly (a) and using MBM method(b).

The bias point (DC work point) of the GMR sensor was measured during scan. The results are presented in Figure 5.20. It is seen that the bias point varied from -1.83V to 0.39V when the sensor is used to measure the field directly, as shown in Figure 5.20(a). From the measurement result presented in Figure 5.17, the sensor is shifted outside of its linear range generating a distorted image shown in Figure 5.19(a). However, the changes is bias point of the sensor in MBM is less than 0.0012 V, which is considered as a fixed operation point.

Next, magnetized steel fastener with 12mm defect in the second layer was tested. The experiment results obtained using GF708 to measure Bz directly and using MBM method are compared in Figure 5.21. To quantify the distortion introduced by the presence of the defect, all contiguous pixels above 30% of the peak value are identified and a contour plot enclosing the region containing pixels is drawn. The

defect indication in Figure 5.21(b) is relatively more obvious than that in Figure 5.21(a).

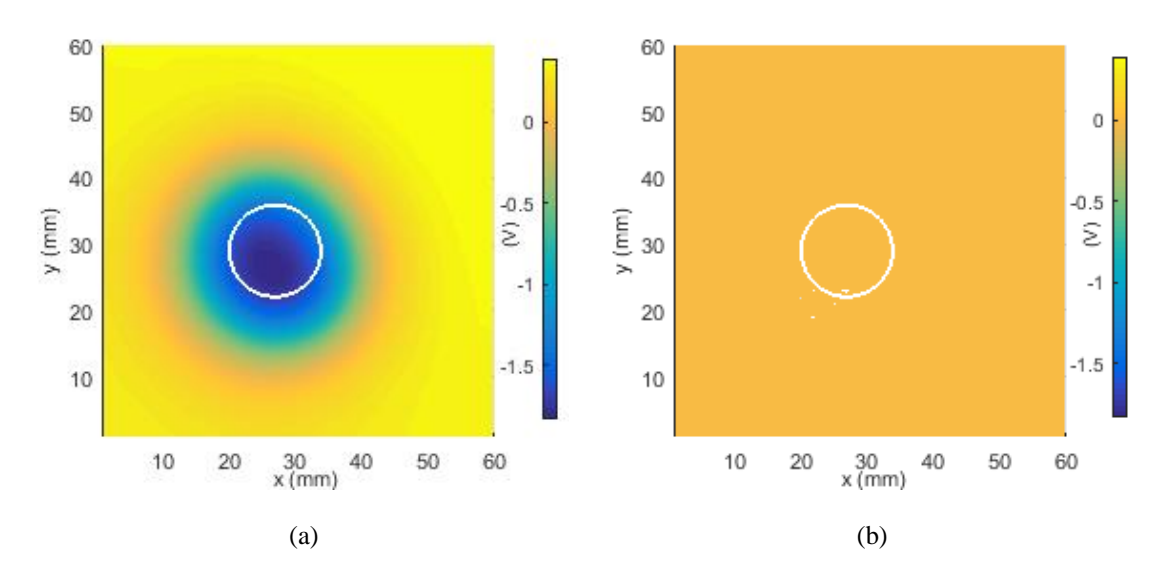


Figure 5.20. Sensor DC bias when measuring the experiment results in Figure 5.19: (a) using the GMR sensor to measure the field directly; (b) using MBM method.

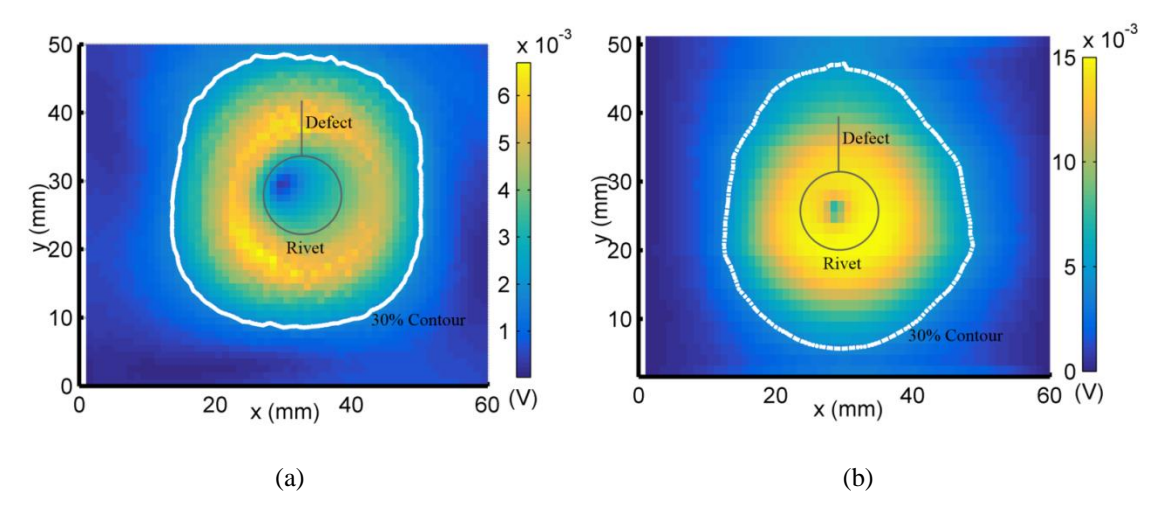


Figure 5.21. Experiment results of magnetized steel fastener with 12 mm defect ($l_d=12$: (a) GF708 measuring Bz directly and (b) MBM method.

5.5 Conclusion

Several conclusions are drawn from the results in this chapter:

(1) Steel rivets become anisotropic in the presence of an external DC magnetic field, which distorts the C-scan image of RoC-GMR probe. This effect can influence with the defect signal and thereby influence the defect detection.

- (2) The influence of geomagnetic field on steel fastener cannot be ignored and should be taken into consideration during post processing.
- (3) A novel scheme, namely, magnetic balance method using MR sensor for inspecting defect around steel fasteners in multilayer structures was presented.
- (4) Numerical analysis first demonstrated the feasibility of MBM method. The bias point of the MR sensor in MBM is kept constant when the fastener is exposed to strong DC field. The effect of the strong remanence field from steel fasteners is eliminated and the operation point of the sensor is kept constant.
- (5) The response to magnetic field was measured showing that the linear measurement range is extended and the hysteresis is reduced by using MBM method.
- (6) Experimental results of defect free magnetized steel fastener show that the MBM method can eliminate the effect of residual magnetism and keep the sensor's bias point constant. Measurement data from magnetized steel fastener with 12 mm length notch show that the MBM method has higher sensitivity to defect detection than that obtained using MR sensor directly.

Chapter 6 Transceiver RoF-EC Probe for Tube Inspection

6.1 Introduction

Nuclear power plants employ steam generator units to transfer thermal energy and isolate the primary radioactive side of the plant from the secondary side of the plant[99]. These tubes are continuously exposed to harsh environmental conditions such as high temperature and pressure resulting in various types of degradation including mechanical wear, stress corrosion cracking, pitting, wall thinning, denting and inter granular attack[99], [100] [101]. In order to ensure the operational safety of the power plants, periodic inspection of steam generator tubes are required. Eddy current inspection techniques have proven to be a fast and effective method for detecting and characterizing flaws in the tube wall[22], [102]. A variety of eddy current probes have been developed for inspection in the last few decades.

6.1.1 Bobbin Probe

The bobbin probe has fast scan speed approximately 1 m/sec and is mainly used for initial detection of possible degradation to quickly determine the areas requiring additional inspection with other probes.

There are mainly two types of bobbin probe: absolute bobbin and differential bobbin probes. Absolute bobbin operates with single bobbin coil and a second identical reference coil, which is used for electronic balancing and is electromagnetically shielded from the inspected tubing. The probe is sensitive to axial cracks and material properties variations in tube free-span sections, and gradually varying wall thinning. Differential bobbin probe has two coils positioned close together with current in one coil, 180 degrees out of phase with the current in the other. The output signal is

obtained as the induced voltage in one coil subtracted from the voltage in the other coil. The probe is sensitive to small defects and abrupt anomalies such as pitting corrosion and fretting wear, relatively unaffected by lift-off, probe wobble, temperature variations, and external interference. The probe is not sensitive to gradual changes and metallurgical variations.

Disadvantages of bobbin probes are the following.

- (1) Insensitive to circumferential cracks, because induced eddy currents are parallel to defects and the probe is inherently unaffected by the presence of such defects.
- (2) Limited resolution for defect location and characterization.

6.1.2 Rotating Probe

Rotating eddy current probes are used for high resolution imaging of steam generator tubes. Pancake or plus Point coils are rotated by motor circumferentially inside tube and moved forward in the axial direction (around 4 inches per second) in a helical pattern.

Rotating probe is sensitive to defects of all orientation, and has high resolution and improved sensitivity to characterize and size defects. However, the mechanical rotation of the coils causes serious wear leading to frequent probe failure. In some cases, the presence of magnetite deposits on tube wall reduces the probe life significantly due to wear. Furthermore, these magnetic deposits can produce a strong signal which obscures the signal from defects. Since the probe has helical scan pattern, the scan speed is slow, which is around 120~80 times slower than that of bobbin probes. Hence, the inspection time and cost increase significantly.

6.1.3 Array Probe

In order to increase inspection speed, the array probe was developed. Nowadays, there are several different types of array probes including: C-probes, X-probe, smart probe and intelligent probe.

The array probe is a transmit-receive probe. The array covers 360 degrees of the circumferential direction of inner tube surface. The probe is optimized to maximize response for different orientation defects and is 10 times faster and has higher signal to noise ratio as compared to the rotating probe.

A typical array probe is composed of an array of pancake eddy current coils. These probe coils are magnetically coupled in a transmit-receive configuration with laterally spaced transmit and receive coils. The transmit (active primary) coils are driven by time-harmonic AC at several frequencies. The receive (passive secondary) coils generate a voltage equal to the time-rate of change of magnetic flux through the coil windings. Anomalies in the test specimen that affect the flow of eddy current and alter the magnetic flux through the windings of the receive coil are detected and characterized by monitoring variations in the receive coil voltage.

Because the coils are configured in a transmit-receive configuration and are geometrically arranged, they are directionally sensitive. One set of coils is used to detect axially oriented defects such as axial cracks. The data generated by these coil sets are referred to as axial channel data. Another set of coils is used to detect circumferentially oriented defects. Both the axial and circumferential coil sets are generally capable of detecting defects that have no directional preference such as volumetric defects and multidirectional cracks. They are capable of detecting and characterizing circumferentially and axially oriented defects such as cracks, as well as volumetric defects such as those caused by corrosion or mechanical fretting.

The array probe has very complicated excitation and data acquisition system, which increases the cost of these probes. A 3×16 array, for example, consists of 48 coils arranged in three rows of 16 coils each. Figure 6.1 shows the coils and the way that the first two axial and circumferential channels are obtained.

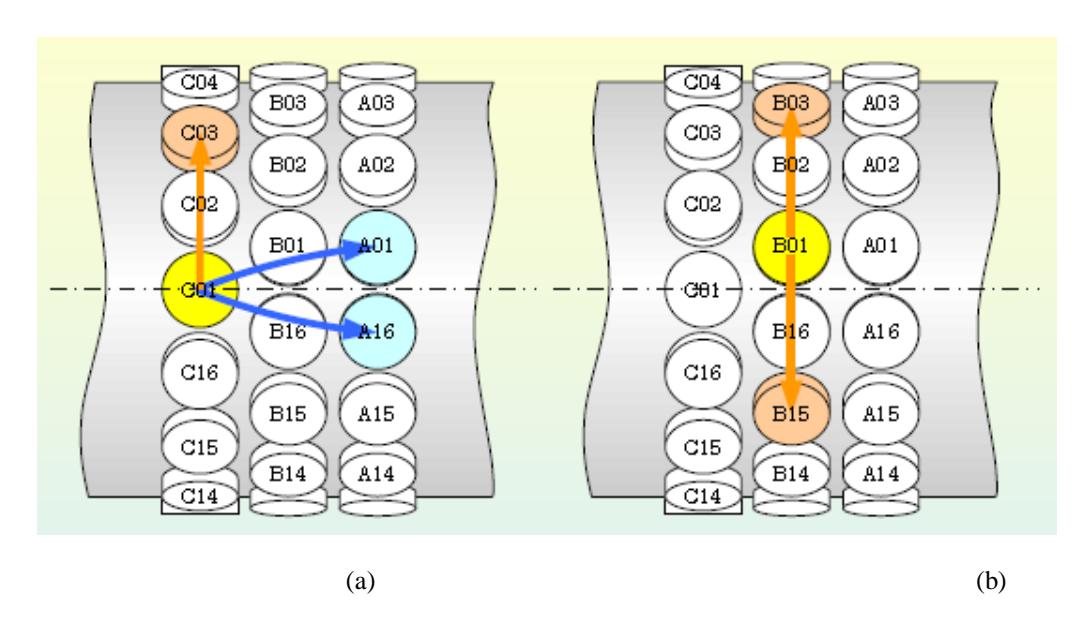


Figure 6.1. Axial and circumferential channels for transmit and receive: (a) axial channels C01-A01 and C01-A16, circumferential channel C01-C03, (b) circumferential channels B01-B03 and B01-B15[103].

6.1.4 Rotating Field Probe with Bobbin Coil

A rotating field (RoF) eddy current probe was proposed by Xin et al. [104], [105]. This design generates a rotating field without mechanically rotating the coils. The principle of RoC-EC probe is similar to that of rotating electrical machines. The RoF-EC probe works in a send-receive mode with excitation and pickup coils. The excitation coil consists of three identical rectangular windings located on same axes physically 120 degrees apart, as show in Figure 6.2. The excitation sources for driving the three windings are three-balanced alternating currents with adjustable amplitude, phase and frequency.

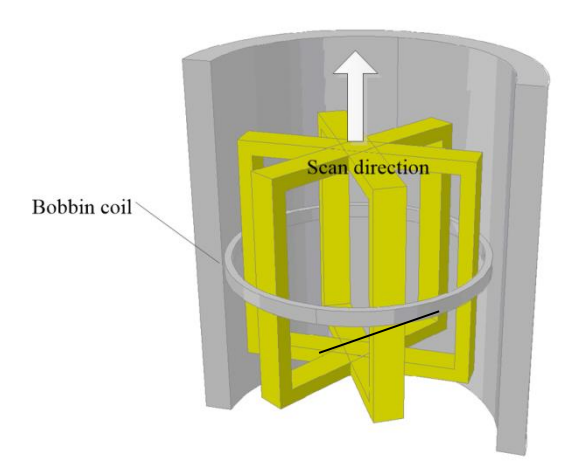


Figure 6.2. 3D model of bobbin pickup and three windings inside the tube[104].

The probe is sensitive to defects of all orientations and offers high operational speed. The disadvantage of the design lies in the need for an additional bobbin coil to pick up the defect signal. The bobbin coil must be wound outside or inside of the three phase exciting windings. If the bobbin coil is located outside of the three phase windings, then the lift off of the three phase windings to tube wall will be increased. If the bobbin coil is located inside the exciting coils, the lift of the bobbin coil to tube wall will be increased. To eliminate the use of bobbin pick up coil, this thesis proposes a novel concept of a transceiver RoF-EC probe.

6.2 Rotating Field Transceiver Probe - Structure and Principle

The RoF-EC probe proposed in this thesis works in transceiver mode[106]. The transceiver coils consist of three identical windings(A,B,C) located 120° apart on the same physical axis, as shown in Figure 6.3(a). The three windings are driven by a three-phase sinusoidal constant current source. Currents in the three windings are identical in amplitude but 120 degrees apart in phase angle. The rotating magnetic field generated by the three phase current is sinusoidal in space and time. The rotating magnetic field induces eddy currents in the tube wall, which flow circularly around a radial axis. Consequently the probe is sensitive to defects of all orientations. Thus the

probe offers detection capability comparable to those obtained with mechanically rotating coil probes but offer higher inspection speed and result in much lower wear and tear[107].

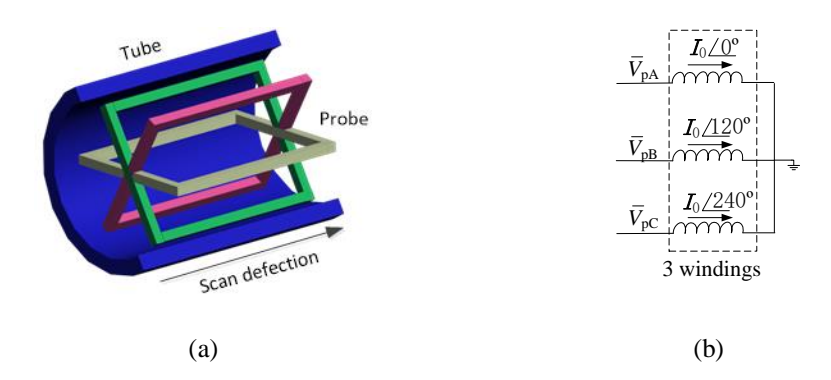


Figure 6.3. (a) 3D diagram of the transceiver coils within a tube. (b) Circuit schematic of the 3 windings.

The terminal phase voltages \overline{V}_{pA} , \overline{V}_{pB} , \overline{V}_{pC} corresponding to the three windings is measured, , as shown in Figure 6.3(b). The terminal voltages is in general expressed as \overline{V}_{p} ,

$$\bar{V}_{\rm p} = Z\bar{I} \tag{6.1}$$

where Z is the coil impedance and \overline{I} is the phase current.

The vector sum of the three phase voltages is equal to zero if the tube wall is defect free. The presence of a defect in the tube wall changes the phase of impedances which alters the balance of the system, resulting in a non-zero signal as given by equation 6.2.

$$\overline{V}_{sum} = \overline{V}_{pA} + \overline{V}_{pB} + \overline{V}_{pC} = \begin{cases} = 0 & when Z_A = Z_B = Z_C \\ \neq 0 & otherwise \end{cases}$$
 6.2

A defect will result in an imbalance in the terminal voltage in the three windings resulting in non-zero \bar{V}_{sum} .

6.3 Defect signals from Transceiver Probe

6.3.1 FEM model

The responses of the transceiver rotating field probe due to defects of different dimensions, directions, locations, and circular orientations are studied using three-dimensional finite element model. The formulation is based on reduced magnetic vector potential Ar, V-Ar formulation[50], [51], [108]. The model solves for the nodal values of the vector magnetic potential A and phasor voltages of the transceiver probe coils are calculated using equation 6.3 [51], [109], [110]

$$\bar{V} = -N \frac{\partial}{\partial t} \iint_{s} \mathbf{B} \cdot \mathbf{n} ds = -N \frac{\partial}{\partial t} \oint \mathbf{A} \cdot d\mathbf{l}$$
 6.3

where N is the number of turns in the coil, S is the average surface area of the coil.

6.3.2 Flat Bottom Hole

First, a flat bottom hole on inner diameter (ID) of the tube wall is simulated. The test geometry is the free span region of steam generators tubes. The inner diameter of the tube is 19.69 mm, and the wall thickness is 0.965 mm. The tube material is Inconel 600 whose conductivity is $9.69*10^5$ S/m. The three-phase coils have diameter, height and thickness of 19mm, 16mm and 0.6 mm, respectively. The excitation current frequency is 45 kHz and current density is 3×10^6 A/m².

The probe moves along the axial direction of the tube (Z-axis) from Z=-25mm to Z=25mm at step size of 1mm. The defect is located at Z=0mm, as shown in Figure 6.4. The simulation results are presented in Figure 6.5. The simulation results were obtained with 3.2 mm diameter flat bottomed holes of varying depths. The probe output signal has a clearly indication of the flat bottom hole. The amplitude of the probe output signal vs. defect depth is plotted in Figure 6.6. The signal amplitude is proportional to the defect depth.

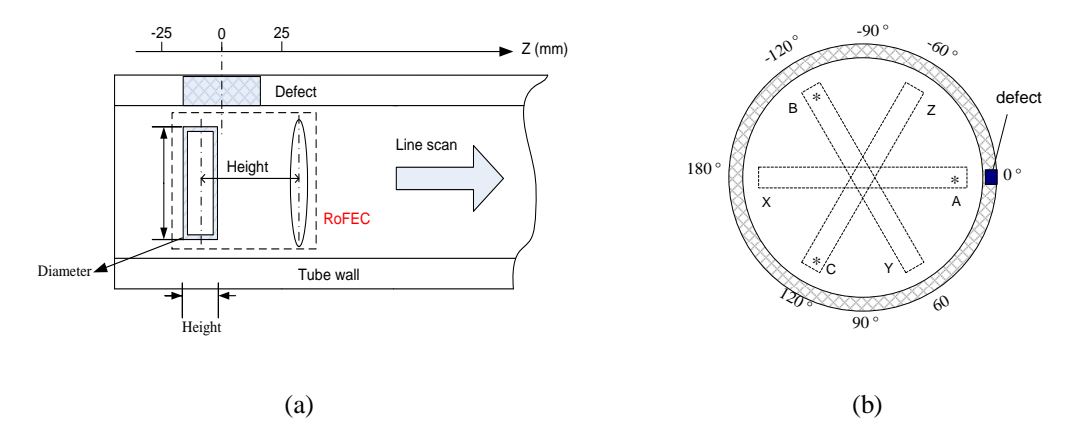


Figure 6.4. (a) Axial direction line scan. (b) Top view of windings.

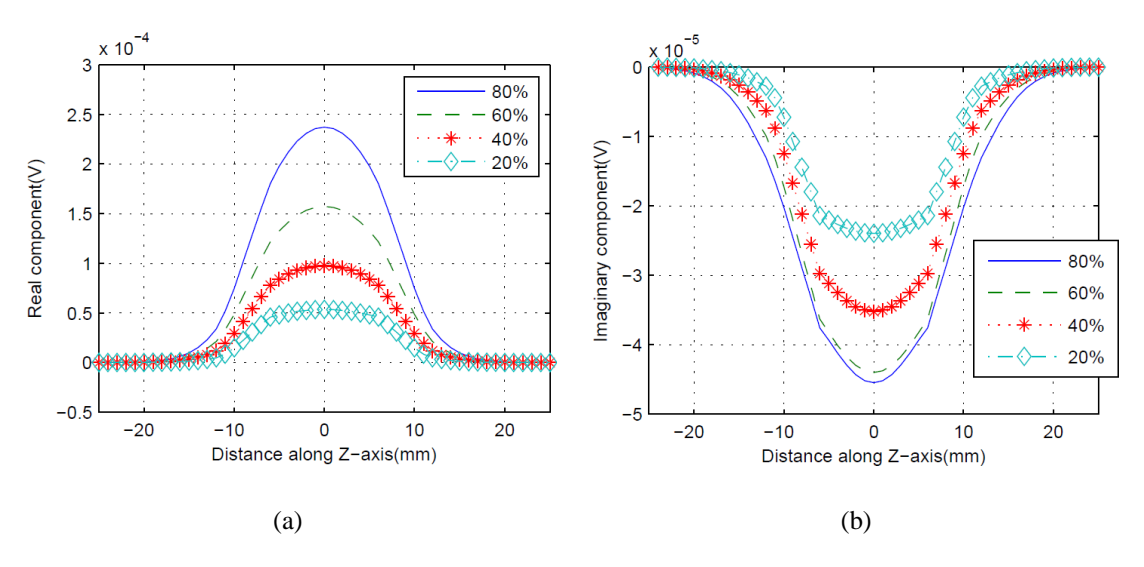


Figure 6.5. Simulation results: (a) real part and (b) imaginary part of probe output signal for ID flat-bottomed holes: diameter 3.2mm, depth 20%, 40%, 60%, and 80%, of tube wall .

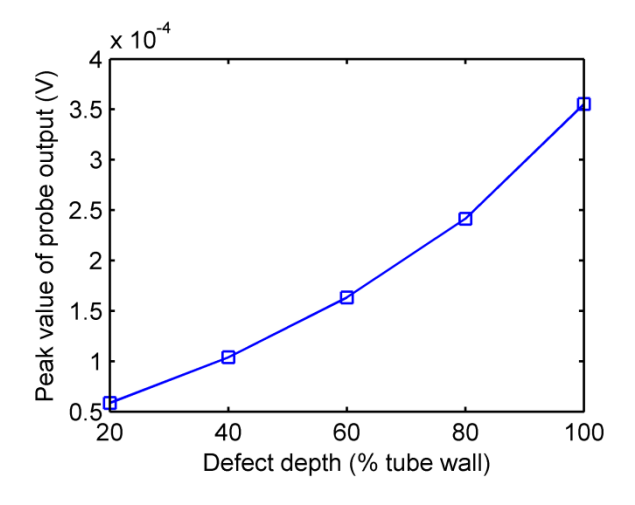


Figure 6.6. Peak value of the probe output signal amplitude vs. flat bottom hole depth.

Next, the rotation of the defect along circumferential direction relative to the probe is studied. As Figure 6.7 shows, the phase angle of the probe output signal is rotated along with the circumferential location of the defect.

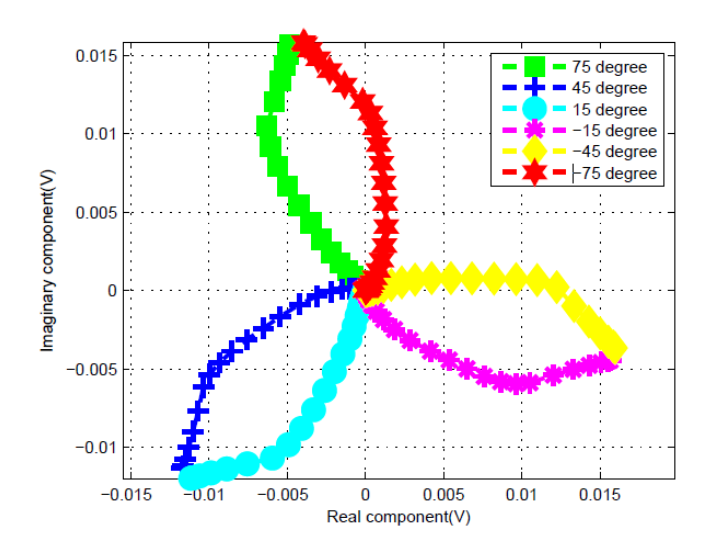


Figure 6.7. Simulation signals obtained with defect located at different circumferential locations

6.3.3 Axial and Circumferential Notch

Next, the responses of the transceiver rotating field probe due to axial and circumferential notches are studied using three-dimensional finite element model.

6.3.3.1 Effect of Defect Depth

In this study, defects are axial or circumferential notches, located at Z = 0mm, 0° circumferentially and the three phase windings are located at 0° , 120° and 240° , inside the tube wall (ID). The depths of the defects are varied from 0.4 mm to 1.4 mm. The length of axial defects is 12mm whereas the length of circumferential defects extends over 60° . The simulation results calculated using equation 6.3 are shown in Figure 6.8. Peak value of the simulation results shown in Figure 6.8 vs. defect depth is plotted in Figure 6.9. The results show that both axial and circumferential defects are detected by the transceiver rotating field probe. The peaks of the signals, which are at the center of defect location, are positively correlated with defect depths.

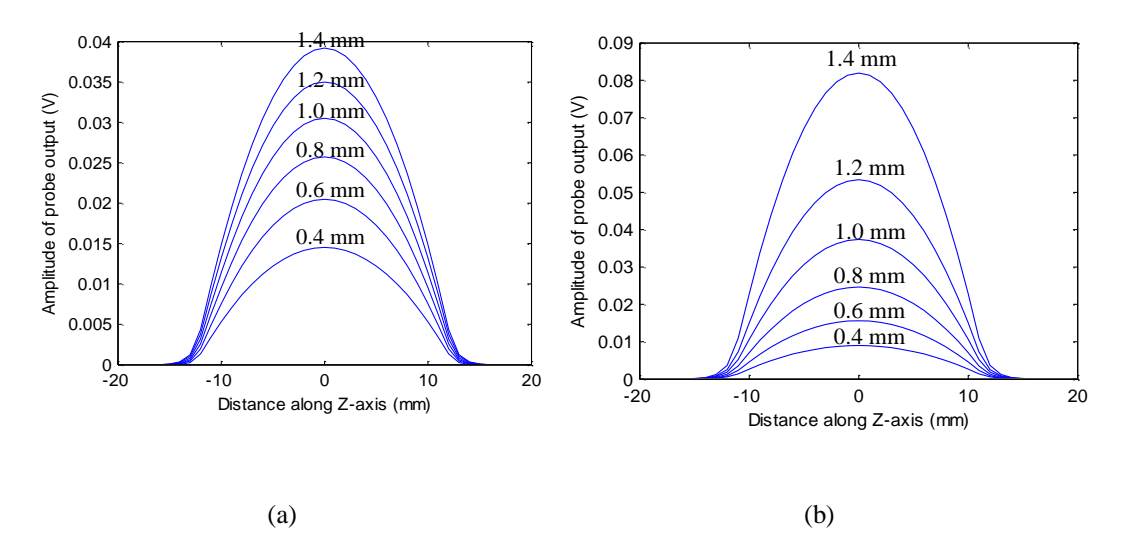


Figure 6.8. Simulation results :probe output signal for varying defect depths for (a) 12mm long axial notch and (b) 60 °circumferential notch.

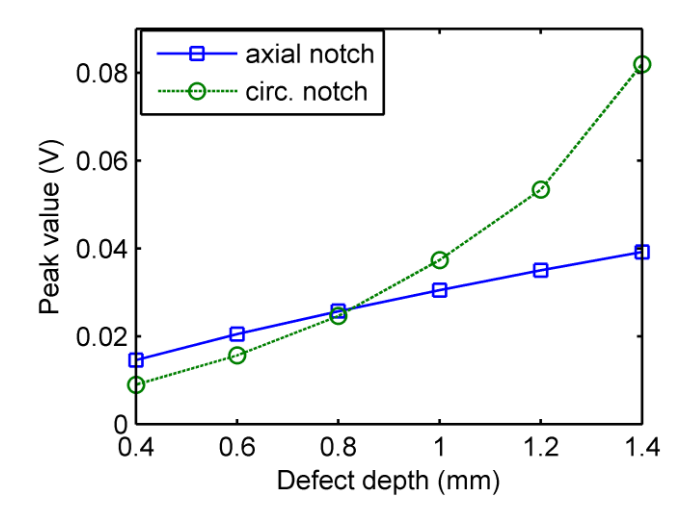


Figure 6.9. Peak value of the probe output signal of axial and circumferential notches vs. defect depth.

6.3.3.2 Effect of Defect Lengths

Next, ID notches of different lengths are simulated. The results are shown in Figure 6.10(a) for an axial defect and in (b) for circumferential defects of depth 0.8mm with different lengths demonstrating that the signals of notches are positively correlated with defect lengths.

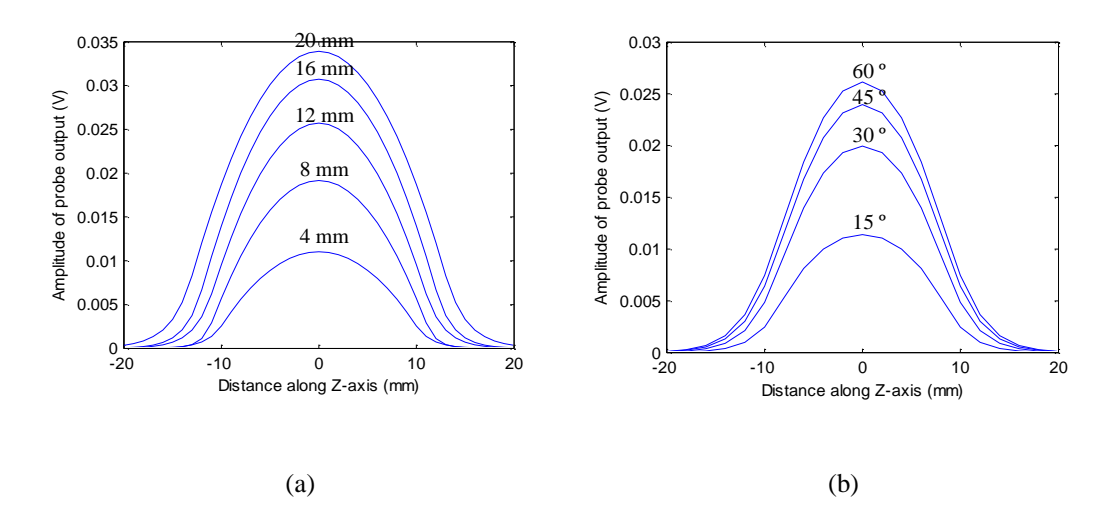


Figure 6.10. Simulation results: probe output signal for varying defect lengths for 0.8mm deep (a) axial notches, (b) circumferential notches.

6.3.3.3 Effect of Circumferential Location of Defect

The feasibility of detecting the defect's angular position is investigated by analysing the transceiver probe signals. Defects in different circumferential locations varying from 0 °to 60 °are simulated.

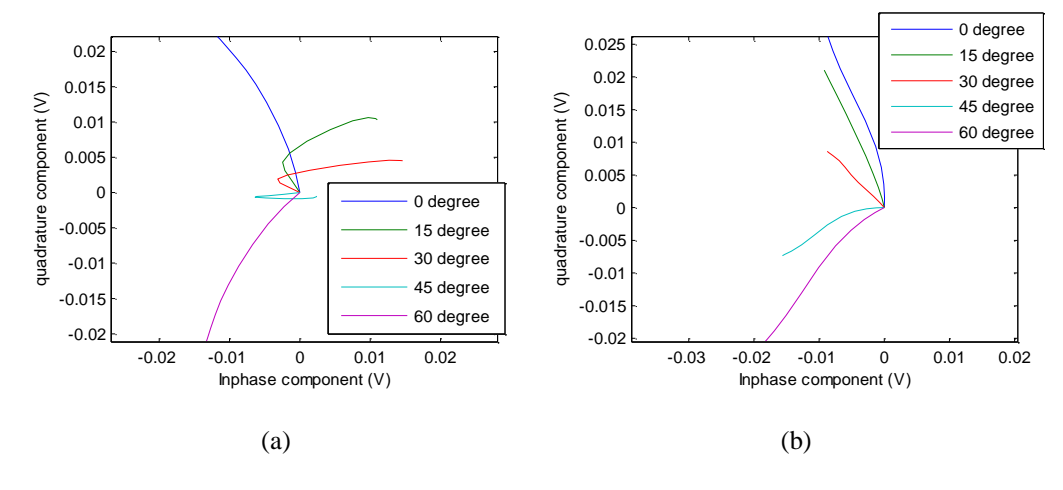


Figure 6.11. Simulation results: Lissajous Pattern seen when the defect circumferential location is varied from 0 °to 45 °(a) axial defect and (b) circumferential defect

Considering the structure of the probe, the response of defect located at angles other than 0° to 60° circularly can be predicted by rotating the corresponding signal. The defects modeled are axial or circumferential through the tube wall (100% of tube wall) notches, located at Z = 0mm. The length of axial defects is 12mm whereas the length of circumferential defects extends over 60° . The simulation results are shown in

Figure 6.11. It is seen that the signal phase rotates by 120 °when the defect location is moved by 60 °, which means that the response will repeat periodically with period 180 °.

6.3.3.4 Effect of ID and OD Defects

Signals from inner diameter (ID) or outer diameter (OD) defects in the tube wall is studied. An axial defect of length 12 mm, depth 0.8 mm (50% tube wall) is simulated at different frequencies: 10 kHz, 30 kHz, 100 kHz, 500 kHz. The output signals are plotted at different excitation frequencies in Figure 6.12. Peak value of the probe output signal of ID and OD defects vs. frequency is plotted in Figure 6.13. The magnitude of the signal increases with frequency for ID defects. But there is no monotonic dependence for an OD defect.

For ID defect that the signal is positively correlated with the excitation frequency, since the induced eddy current in the tube wall and the induced voltage in the coil are positively correlated with the excitation frequency. This is true for OD defect in certain frequency range. However, the penetration depth is another parameter need to be considered for OD defect. As has been discussed in Chapter 2, the penetration depth of eddy current is inversely proportional to the square root of the exciting frequency. When the frequency is high enough, the penetration depth will become very small that little eddy current can penetrate though the tube wall to reach the defect located on the OD of tube wall. As result, for OD defect the signal doesn't increase monotonically as frequency increases.

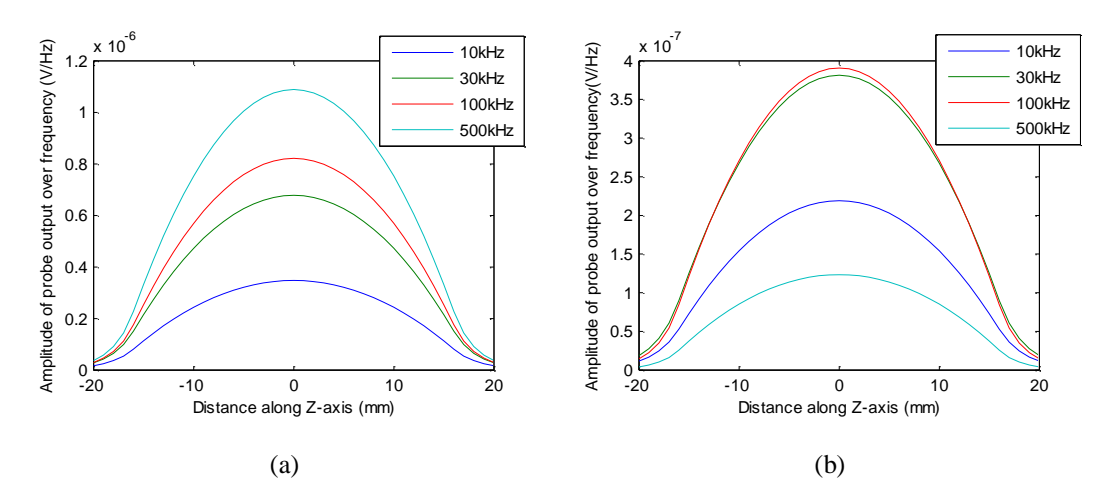


Figure 6.12. Simulation results: normalized amplitude of probe output vs. Z-axis of varying exciting frequency for axial length 12 mm, depth 0.8mm (a) ID and (b) OD defects.

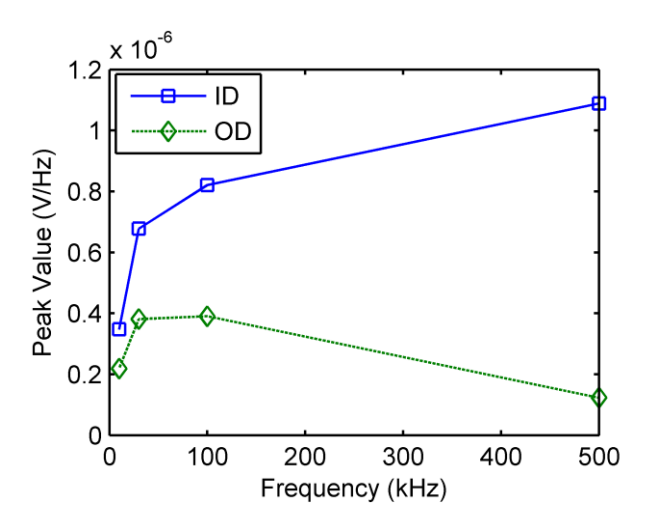


Figure 6.13. Peak value of the probe output signal of ID and OD defects vs. frequency.

6.4 Experiment Validation

A prototype probe with three phase windings has been built to validate the simulation results and demonstrate the proof of concept.

6.4.1 Prototype Probe Design and Experiment Setup

The details of probe design are presented in Figure 6.14 and the parameters are listed in Table 6.1. The three windings employ an identical number of turns. The three DC resistances were measured to be 23Ω , 24.7Ω and 25.5Ω respectively.

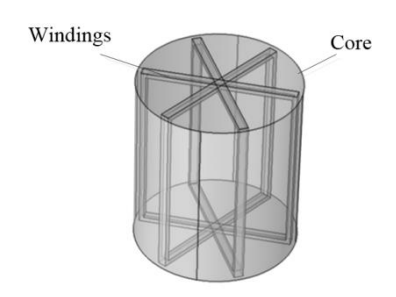


Figure 6.14. 3D diagram of transceiver rotating field probe

Table 6.1. Parameters of transceiver rotating field probe

Windings	OD	Height	Width	Wire	Turns	
	17 mm	20 mm	3mm	Copper AWG 24	160	
Core	OD	Height	Slot Width	Slot depth	Material	
	19 mm	20 mm	3mm	4mm	Plastic	

The three phase sinusoidal excitation circuit is shown in Figure 6.15(a). A two channel function generator is used to generate sinusoidal signals. The two signals are identical in amplitude but 120 °apart in phase. The third phase is obtained by adding these two signals and inverting the resulting signal. A voltage controlled constant current source circuit is shown in Figure 6.15(b), where the resistances are such that R2=R3=R4=R5. The output current is given by $I_{out} = V_{in}/R_1$. The operation frequency range of the system is from 100 Hz to 100 kHz.

Responses from the three phases are added to generate the probe output signal. The addition is performed using an adder circuit. The signal is amplified 20 times by an amplifier. A lock-in amplifier model SR844 from Stanford research system is used to recover the baseband signal and improve the signal-to-noise ratio. The in-phase and quadrature components of the signal are transferred from the lock-in amplifier to a computer though a GPIB cable and stored.

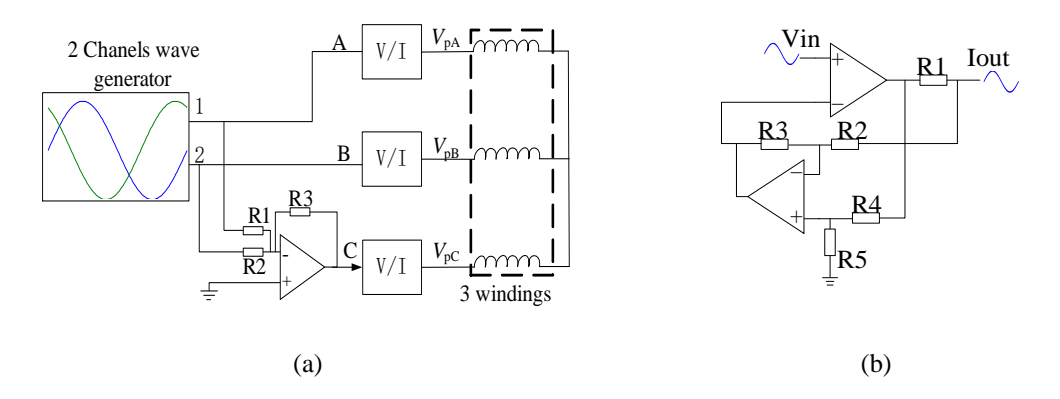


Figure 6.15. (a) Schematic of the excitation system. (b) Constant current source circuit.

The experimental setup is shown in Figure 6.16. A steam generator tube with flat bottomed holes, axial and circumferential notches of varying depths is inspected using the transceiver rotating field probe.

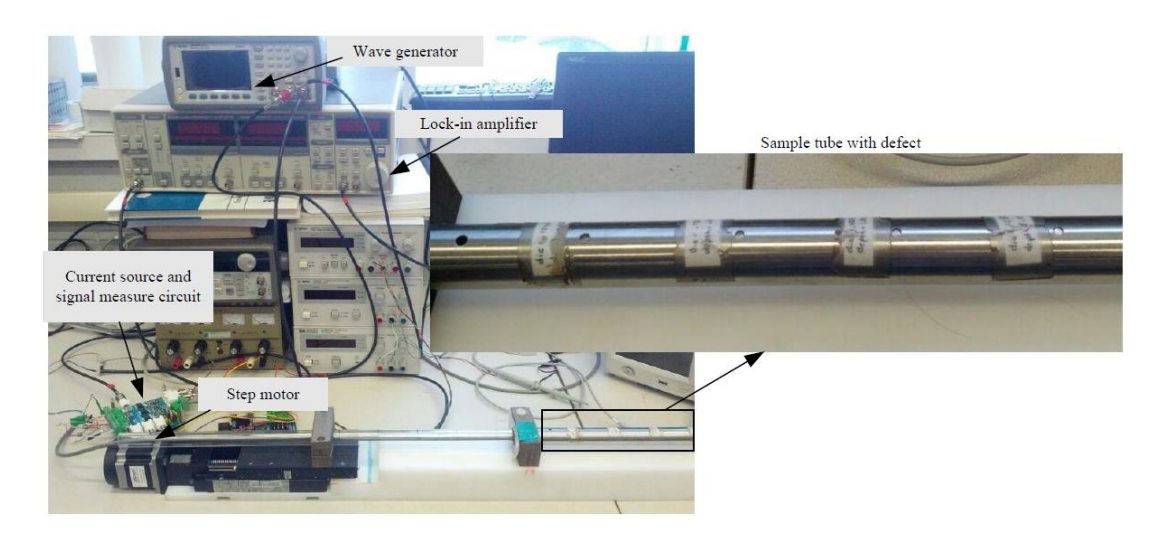


Figure 6.16: Photo of transceiver rotating field probe for tube inspection.

6.4.2 Flat Bottom Hole

Figure 6.17 presents the experimental probe output signals obtained from defects of different depths. The current in each phase is 0.02A. The flat-bottomed hole diameter is 3.2 mm. For the purposes of validation, these experimentally derived signals should be compared with the simulation signal shown in Figure 6.5. It should be noted that the experimental signal is not zero in the absence of a defect since the three phase windings are not identical.

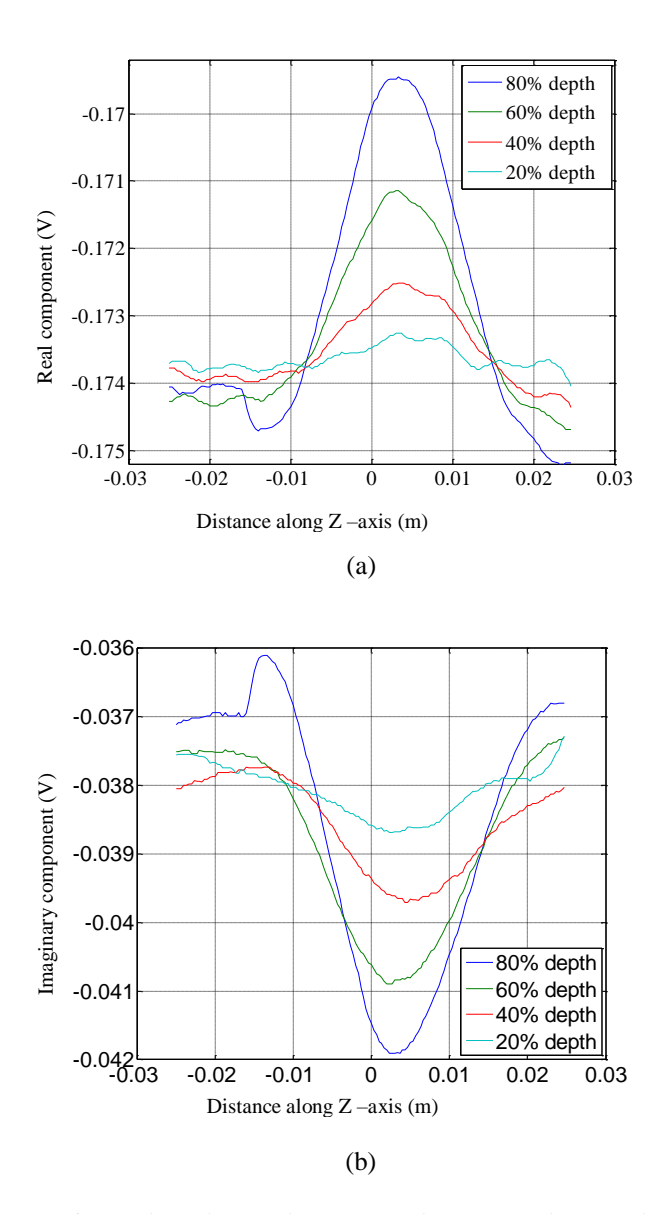


Figure 6.17. Experimental results: probe output voltage,(a) real part and (b)imaginary part.

6.4.3 Axial and Circumferential Notch

A steam generator tube sample with machined axial and circumferential notches is inspected using the prototype probe. The tube material is INCONEL 690. The geometric dimensions of the tube and the defects are specified in Figure 6.18. The machined notches, named (a)-(e), are located on the outside of tube wall.

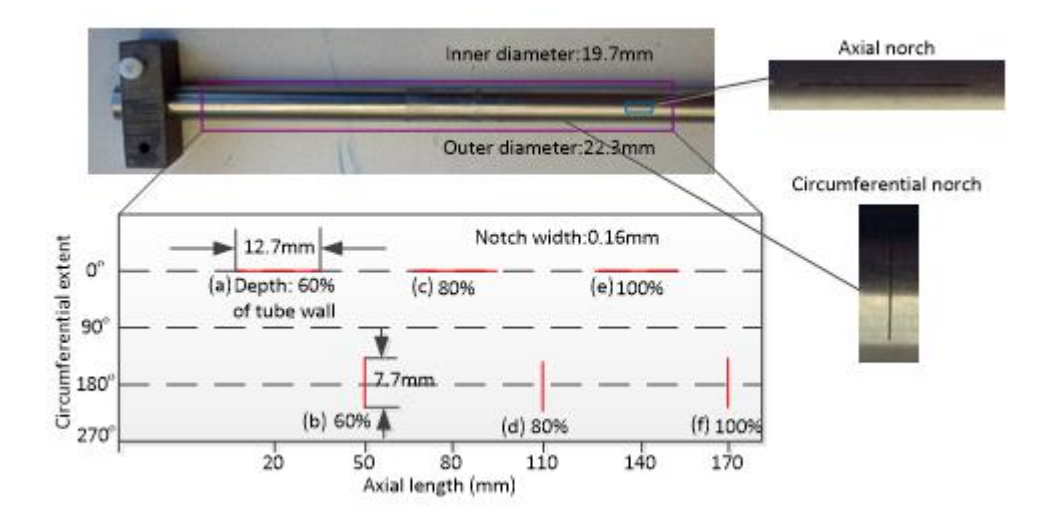


Figure 6.18. Geometry dimensions of steam generator tube with machined notches.

The transceiver RoF-EC probe scans along the tube axial direction with the 'A' phase winding of the three-phase exciting coils located at 30 °circumferentially. Figure 6.19 presents the experimental probe output signals. As the defects are not far away from each other; the signals from adjacent defects overlap and influence each other to some extent. The experimental result shows that both axial and circumferential notches are detected by this rotating field probe operating in transceiver mode. The axial locations of the defects and the local peak of the signal are listed in Table 6.2. The axial location of the defects and local signal peak coincide well, which means that the axial location of the defect can be determined from the output signal of the probe.

Next, the circumferential location of defect is varied. The Lissajous plots of defects e and f with circumferential locations varying from 0° to 45° are shown in Figure 6.18 and Figure 6.20 respectively.

It is found that the phase angles of the signals rotate approximately 90 ° when the defect is moved by 45 °circumferentially. Due to symmetry of the probe coil geometry, this probe cannot distinguish defects located at α^{o} from $(180+\alpha)^{o}$ circumferentially ,where α is any angle. It is should also be noticed that the magnitude of the signal of circumferential notch depends on the circumferential location of the

defect, since the induced current, especially the axially directed eddy current, is not uniform along the circumference of the tube wall.

Table 6.2. Axial location of the defects and correlated signal peak

	a	b	c	d	e	f
Defect axial location (mm)	20	50	80	110	140	170
Local signal peak axial location (mm)	20.33	47.9	78.2	110.3	142.1	171.2

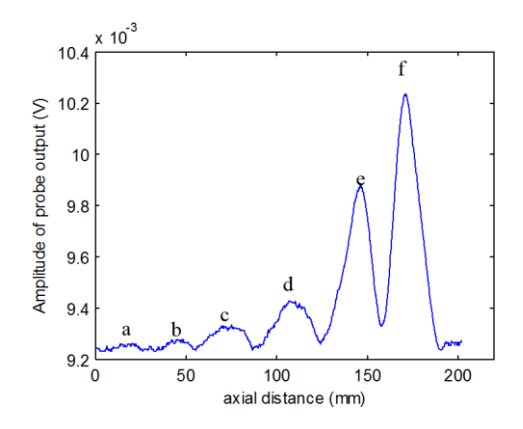


Figure 6.19 : Experimental results: amplitude of probe output as a function of probe location along the tube axis.

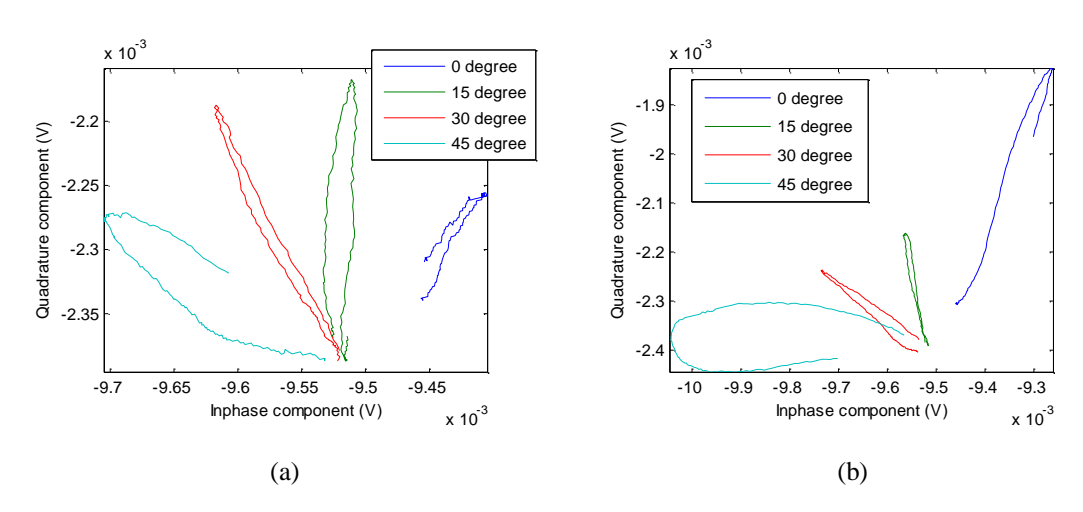


Figure 6.20. Experiment results: Lissajous Pattern seen when the defect circumferential location is varied from 0 °to 45 °of (a) signals of axial notch (b) signals of circumferential notch.

6.5 Conclusion

The novel transceiver probe employs a rotating electromagnetic field and avoids mechanical rotation of coils. A transceiver configuration is proposed with the probe output signal equal to the sum of the three phase voltages. A major advantage of this design is that a relatively simple control and excitation hardware system is needed.

The probe employs a relatively simple mechanical structure, offers high inspection speed since it does not involve mechanical rotation.

Both axial and circumferential defects as well as ID and OD defects are detected by the probe. The probe signal peak magnitude is proportional to the defect depths. The defect's axial location can be estimated by locating the peak of the signal.

The drawbacks of the transceiver RoF-EC probe are: (1) 1D scan data and not a C-scan image is generated for visualization of defects. (2) Will not distinguish between single and multiple defects at same axial location. (3) The magnitude of the signal of circumferential defect depends on the defect's circumferential location relative to coil windings.

These problems are addressed in the proposed probe design in Chapter 7.

Chapter 7 RoC-GMR Probe for Tube Inspection

7.1 Motivation

The transceiver RoF-EC probe presented in Chapter 6 is suitable for detecting and locating defects in steam generator tubes in nuclear power plants with high inspection speed. The main limitation of the RoF-EC probe is that it produces a single line scan data in contrast to a C-scan image generated by array coil probes and rotating probes. This chapter describes the design, development and evaluation of a novel RoC-GMR probe that can provide C-scan images of the induced fields by using an array of GMR sensors.

The RoC-GMR probe design proposed in this chapter has following advantages compare with other probes.

- (1) GMR sensors offer high sensitivity over a wide range of frequencies from DC to MHz frequencies with potentially very fine spatial resolution.
- (2) In a commercial array probe, because the coils are configured in a transmit-receive configuration and are geometrically arranged, they are directionally sensitive. Both axial channel and circumferential channels are required to detect different orientations of cracks. In contrast, the RoC-GMR probe is sensitive to all orientation cracks and the topological shape and orientation of the defect can be characterized from the C-scan image.
- (3) This probe can achieve higher inspection speed as compared to array probe and rotating probe, since it does not work in transmit-receive configuration, or need mechanical rotation.

(4) Array probe has very complicated excitation and data acquisition system. In contrast, the excitation and data acquisition system of RoC-GMR probe is much simpler, as described in the next section.

7.2 Operation Principle

The RoC-GMR probe for tube utilizes rotating current excitation and giant magnetoresistance (GMR) array sensors for measuring the induced magnetic fields. In Chapter 3, the RoC-GMR probe for fastener inspection in multilayer planar structure is introduced. A similar principle is used for tube inspection. The top view of RoC-GMR probe for riveted structure inspection with orthogonal coils and array sensors is shown schematically in Figure 7.1(a). Two planar coils that are

perpendicular to each other and are excited by current sources that are 90° apart in phase generate rotating eddy currents with GMR sensors to pick up the normal

component of the induced magnetic field. The resulting signal contains information of

defect in the sample. If the probe is rolled into a cylinder, as shown in Figure 7.1(b),

we get a RoC-GMR probe that is used for tube inspection.

Instead of x and y direction coils, this probe has axial and circumferential coils, which are perpendicular to each other at every intersection. The currents in the two coils are written as in equation 7.1 and 7.2.

$$I_c = I_{0c}\cos(\omega t) \tag{7.1}$$

$$I_a = I_{0a}\cos(\omega t + 90^0) 7.2$$

where I_c is current in the circumferential coil, I_a current in the axial coil, ω angular frequency, I_{0c} and I_{0a} are current amplitude of the circumferential and axial current respectively. The magnetic field generated by the coils is sinusoidal in time, and so are the induced eddy currents in the sample.

The total eddy current (J_{eddy}) in the tube wall is written as

$$J_{eddy} = \bar{J}_c \boldsymbol{\varphi} + \bar{J}_z \mathbf{z} \tag{7.3}$$

where φ , \mathbf{z} are unit vectors in the cylindrical coordinate system, \bar{J}_c and \bar{J}_z are the circumferential and axial eddy current density phasors. The total eddy current vector rotates in space and is sensitive to defects at arbitrary orientations.

A circumferential array of GMR sensors measures the radial component of induced magnetic field. The probe scans along axial direction inside tube and a C-scan image is acquired during a line scan.

GMR sensor offers high sensitivity over a wide range of frequencies from DC to MHz [111]. The spatial distance between sensors as fine as 1.6 mm is achieved using commercial GMR sensors and even much finer, in the order of micro-meter, using microfabrication technologies to integrate sensors in a signal chip[112].

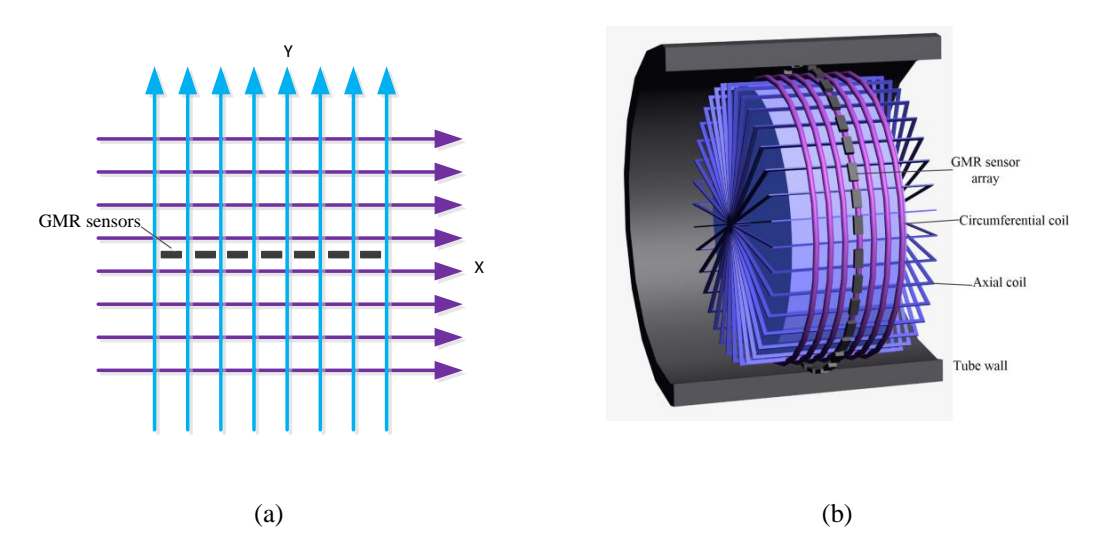


Figure 7.1. (a) Top view of RoC-GMR probe for riveted structure inspection. (2) 3D diagram of RoC-GMR probe for tube inspection

7.3 Simulation Result of Eddy Current in Tube Wall

The excitation coils inside tube without defect are simulated to understand the underlying physical process. Exploiting the superposition principle, the circumferential and axial excitation currents are considered independently.

The geometry of the free span region in a steam generator is modeled. The inner and outer diameter of the simulated tube is 19.7mm, and 22.3mm respectively. The material of tube is Inconel 600, with conductivity 9.69*10⁵ S/m.

7.3.1 Circumferential Current

First, the induced eddy current due to the circumferential coil is calculated. The circumferential coil consists of uniformly distributed wires. The dimensions of the coil are specified in Figure 7.2. The current in the coil is given by $I_c = \cos(2\pi ft)$, where f=30 kHz. The frequency of 30 KHz is chosen so as to ensure adequate skin depth to penetrate the tube wall thickness. The eddy currents induced by the circumferential coil flows circumferentially in the tube wall. The in-phase (real) and quadrature (imaginary) component of the circumferential eddy current density in the tube wall is presented in Figure 7.3. The circumferential coil is similar to a bobbin coil and the induced eddy current flows circumferentially in the tube wall, which is sensitive to axial defects.

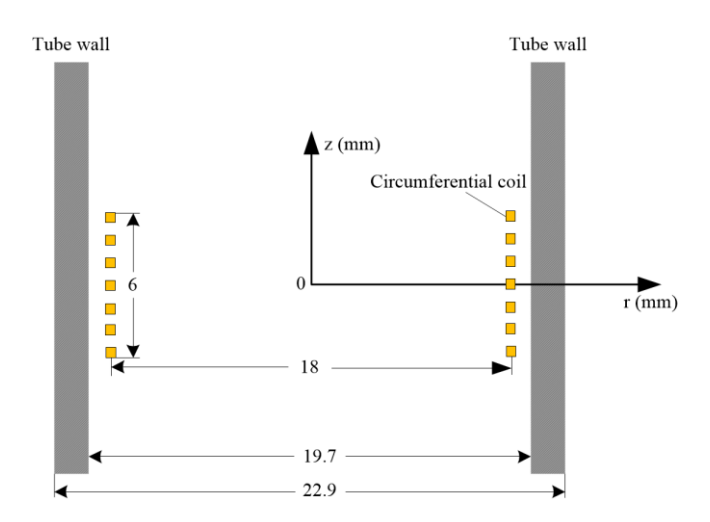


Figure 7.2. Lateral view of circumferential coil and tube wall.

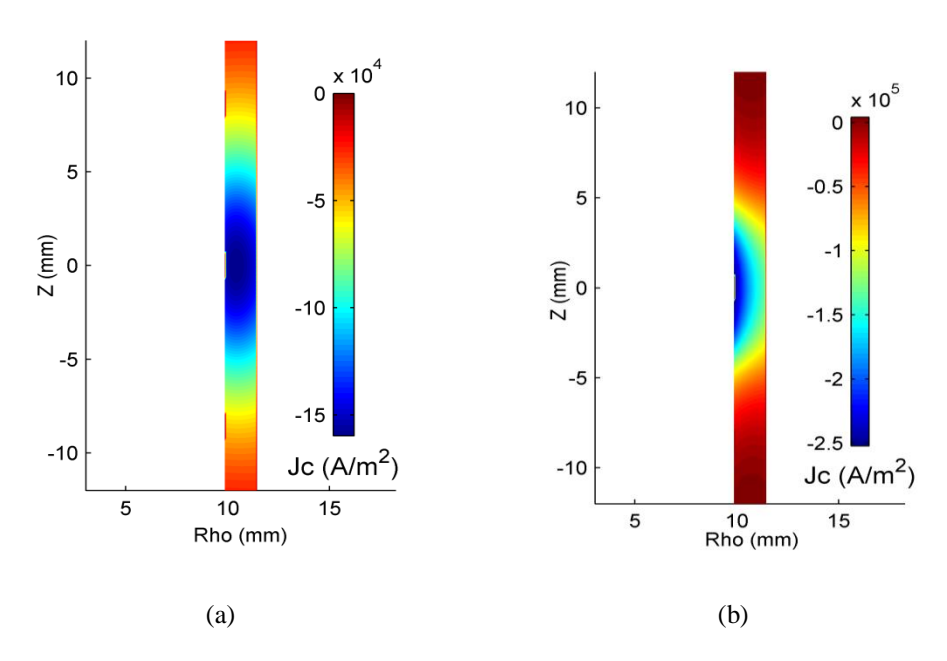


Figure 7.3. Simulation result of in-phase (a) and quadrature (b) component of circumferential eddy current density in a cross-section of tube wall.

7.3.2 Axial Current

Next, the axial coil is simulated. The top and lateral views of the axial coil are as shown in Figure 7.4. Current in the axial coil is $I_a = \cos(2\pi f t + 90^{\circ})$, where f=30 kHz. The induced current in tube wall mainly flows in axial direction near z=0 plane where the GMR sensors are located. The in-phase and quadrature component induced eddy current density in axial direction at z=0 plane are shown in Figure 7.5. From the results presented in Figure 7.5, it is seen that the axial induced current is largely uniform except in the area where the excitation current changes direction. The fact that the length along the circumference where the eddy current density drops to less than 36.8% (1/e) of average value is about 4.8% of the circumference leads to two conclusions namely: i) large circumferential defect, e.g. defect longer than 4.8% of the circumference, is detected with high probability; ii) low probability of missing small defect lying in the null region of the coil. To obtain absolutely full coverage of small circumferential defect, two axial coils that are shifted relative to each other must be used.

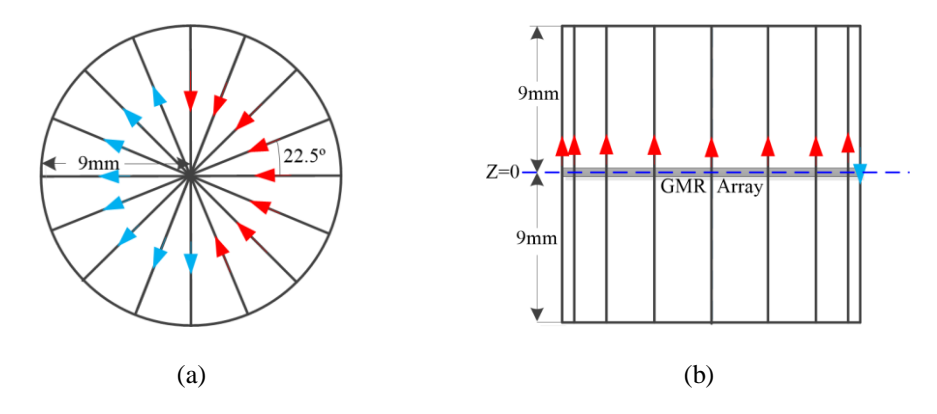


Figure 7.4. Top view (a) and lateral view (b) of axial coil.

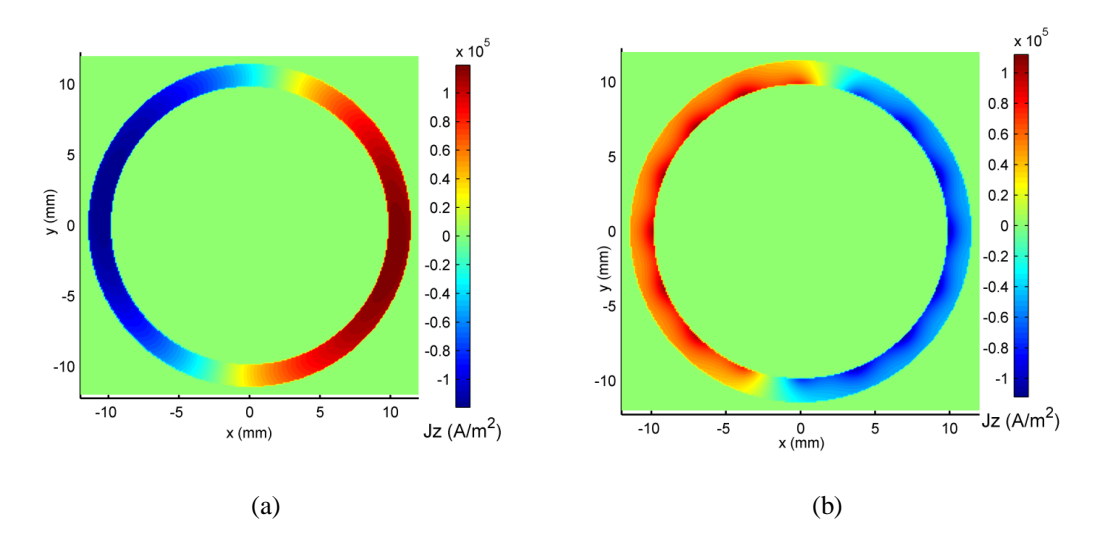


Figure 7.5. Simulation result of (a) real and (b) imaginary component of axial eddy current density, measured on z=0 plane.

7.4 Simulated Signals using RoC-GMR Probe

Signals of defects of different size, orientation and location in the tube wall are predicted using the FEM model to study the detection capability of the RoC-GMR probe.

7.4.1 Axial and Circumferential Notch

Axial and circumferential notches are simulated to obtain the probe signals. The dimensions of the axial notch are length = 12 mm and width = 0.5 mm, and dimensions of circumferential notch is 7.7 mm \times 0.5 mm. The depth of the notch is 100% of the tube wall. The notches are located at $(z, \Theta) = (0.180 \, \%)$. The simulation

results of axial and circumferential notches are presented in Figure 7.6 and Figure 7.7 respectively.

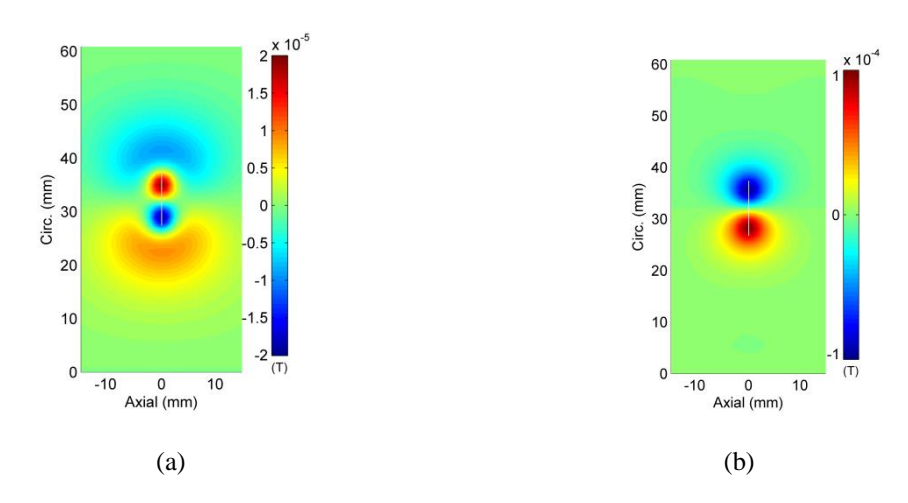


Figure 7.6. Simulation result of circumferential notch (7.7 mm×0.5 mm, 100% tube wall): (a) real component and (b) imaginary component.

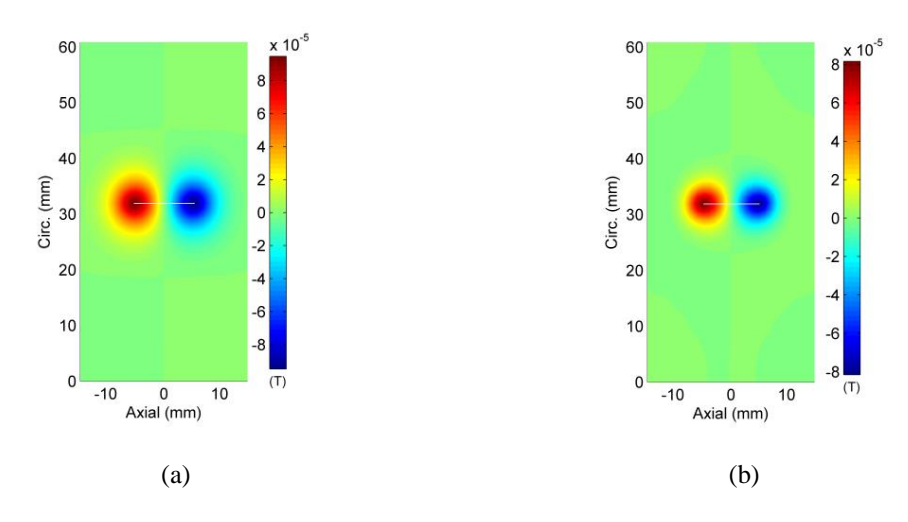


Figure 7.7. Simulation result of axial notch (12 mm×0.5 mm, 100% tube wall): (a) real component and (b) imaginary component.

Both circumferential and axial notches are detected by the probe. The peak values of magnitude of the signals from axial and circumferential notches are 1.13×10^{-4} and 2.12×10^{-5} respectively which implies that the probe has similar sensitivity to defects at different orientations. For a long thin notch, there are two lobes indicating the two ends of the defect in the C-scan image.

7.4.2 Effect of Defect Depth

Next, OD circumferential notches (7.7 mm×0.5 mm) of increasing depths (varying from 12.5% to 87.5% of the tube wall) are simulated. The simulation results are presented in Figure 7.8. To further analyze the results, data along the circumferential scan at Z=0mm is plotted in Figure 7.9. Figure 7.10 is the corresponding Lissajous Pattern of real and imaginary component of the data in Figure 7.8. The magnitude of the signal is positively correlated with the defect depth.

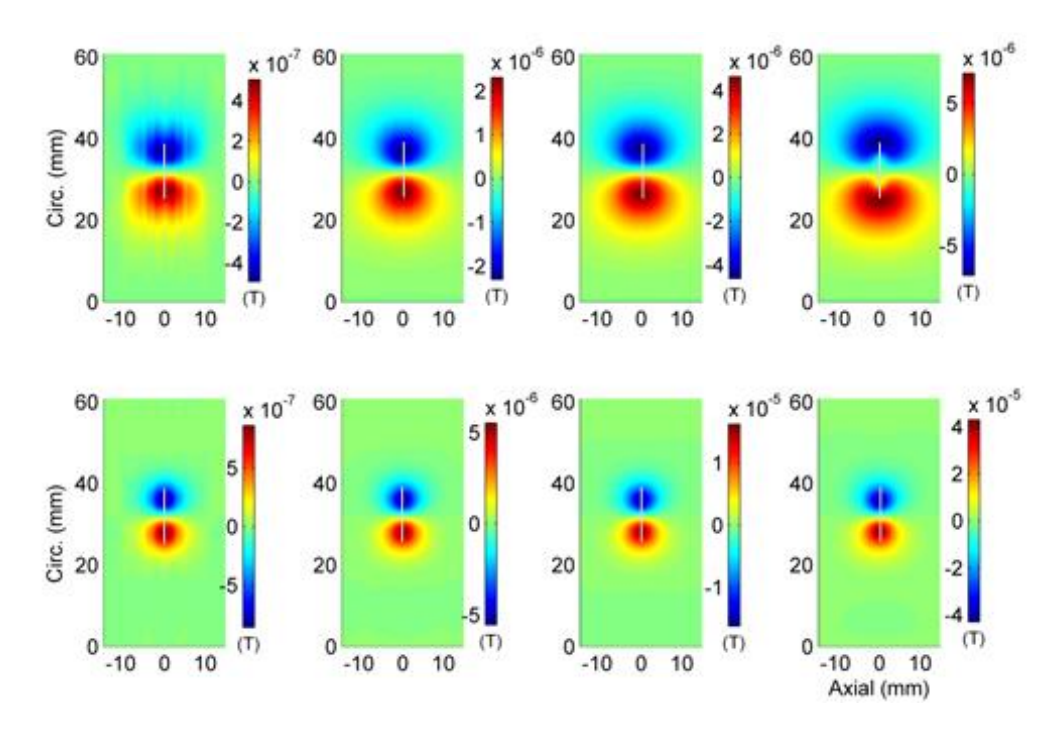


Figure 7.8. Simulation result of circumferential notch (7.7 mm×0.5 mm) with different depths: 1/8, 3/8, 5/8 and 7/8 of the tube wall from left to right. First row: Real component; Second row: imaginary component.

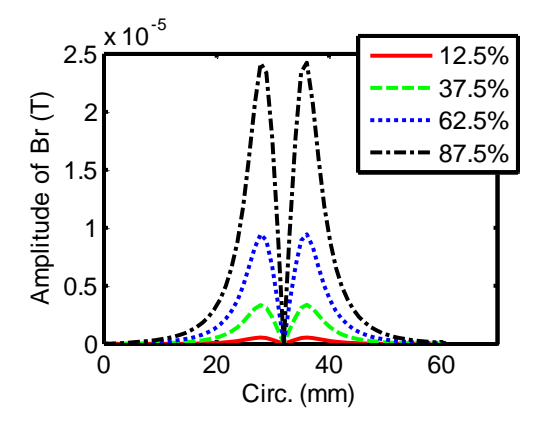


Figure 7.9. Simulation results of circumferential notches with different depths: amplitude of RoC-GMR probe signal vs. circular distance along the circumferential direction at Z=0mm.

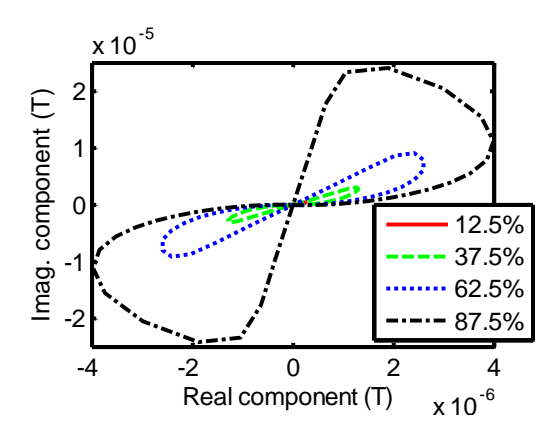


Figure 7.10. Simulation results circumferential notches with different depths: Lissajous Pattern seen of real and imaginary component along the circumferential direction at Z=0mm.

7.4.3 Effect of Defect Length

OD circumferential notches of different lengths (varying from 1mm to 5mm of the tube wall) are simulated. The depth of the notch is 50% of the tube wall, width is 1mm. The simulation results are presented in Figure 7.11. Data along the circumferential scan at Z=0mm is plotted in Figure 7.12. Figure 7.13 is the corresponding Lissajous Patterns of real and imaginary component of the data on the line scan.

The magnitude of the signal is positively correlated with the defect length. It is possible to detect defect of size 1mm × 1mm defect using proposed RoC-GMR probe.

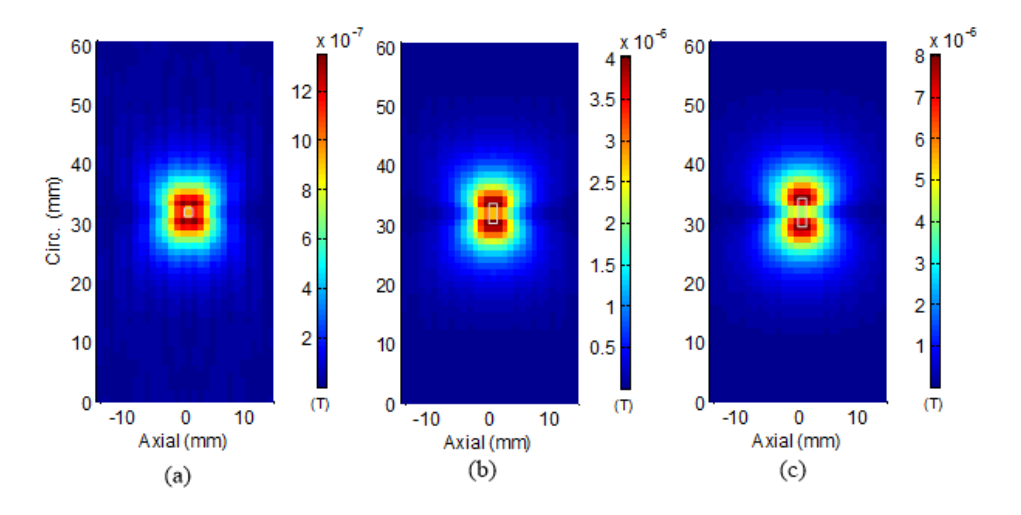


Figure 7.11. Simulation result of 50% tube wall OD circumferential notch length (a) 1mm, (b) 2.5mm, (c) 5mm × width 1mm.

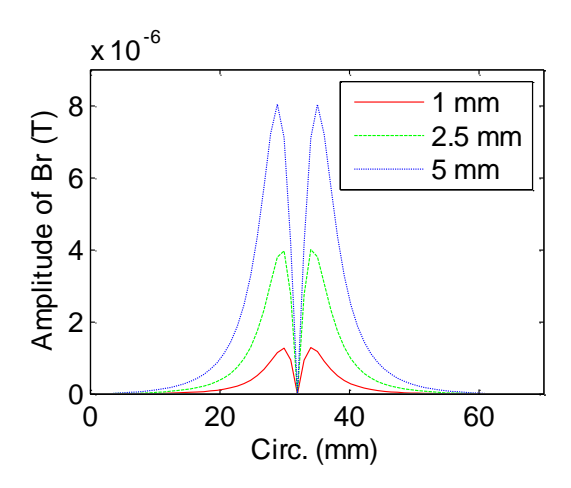


Figure 7.12. Simulation results of 50% tube wall OD circumferential notch with width 1mm and different length. Amplitude of RoC-GMR probe signal vs. circular distance along the circumferential direction at Z=0mm.

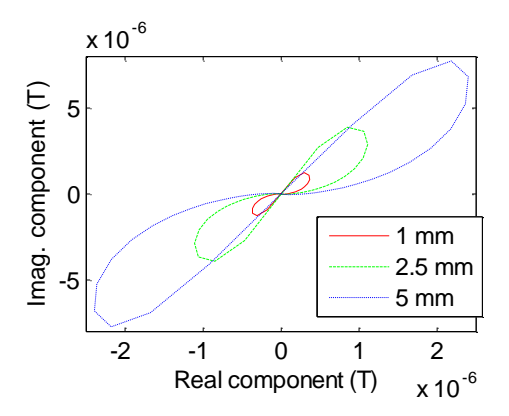


Figure 7.13. Simulation results of 50% tube wall OD circumferential notch with width 1mm and different length. Lissajous Pattern seen of real and imaginary component along the circumferential direction at Z=0mm.

7.4.4 Flat Bottom Hole

Lastly, a 2mm diameter circular flat-bottomed hole is introduced in the tube wall and the inspection with the RoC-GMR probe is simulated. The defect is located on the OD of the tube wall, with depth 50% of the tube wall. The defect is located at Z=0mm. All the other parameters are identical as specified in section 7.4.

The in-phase and quadrature components of probe output image of the simulation results are presented in Figure 7.14.

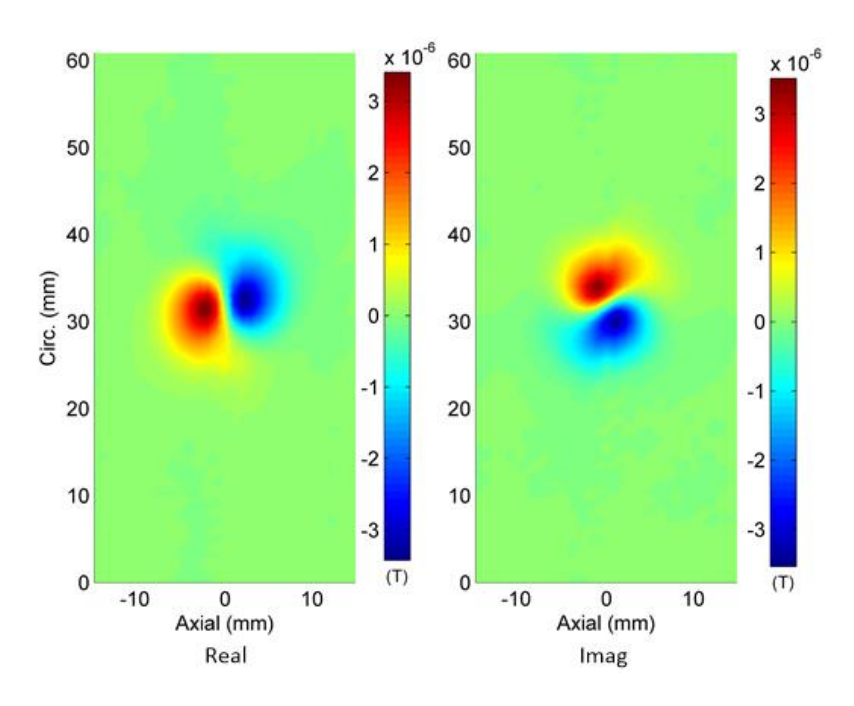
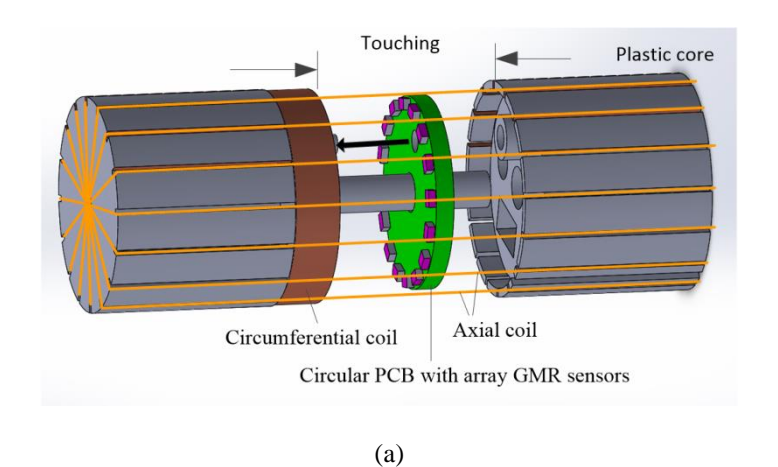


Figure 7.14. Simulation result of 2mm diameter flat bottom hole, left-in-phase component; right - quadrature component.

7.5 Prototype Probe Design

A prototype probe with 16 GMR sensors, axial and circumferential excitaion coils, signal condition circuit and data acquisition system has been built, as shown in Figure 7.15(a). The GMR sensors are soldered on a circular printed circuit board. The radius of the circle where the GMR sensors are located is 8.5mm. The axial and circumferential coils are fabricated on a 3D print plastic core. The diameter and height of the plastic core is 19mm and 20mm respectively. The circular PCB with GMR sensor array, multiplexer and pre-amplifier circuit is located inside the core.

A two-phase current source is used to drive the circumferential and axial coils. The two phase currents are identical in frequency 30 kHz and 90 ° apart in phase. Amplitudes of the excitation currents are 295 mA.



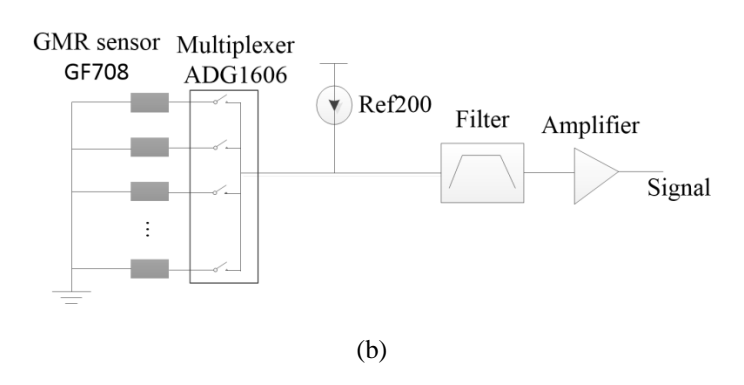


Figure 7.15. (a) Schematic of the prototype probe. (b) Schematic diagram of experimental system.

A schematic of the experimental system is as shown in Figure 7.15(b). The GMR sensors are connected using a multiplexer ADG1606. A DC constant current source Ref200 is used to driven the sensors. The variation of resistance of the GMR sensors is transferred to voltage signal according to equation 7.4 where I_0 is constant ($I_0 = 100\mu\text{A}$), ΔR is resistance changes of the GMR sensor, ΔV is voltage signal.

$$\Delta V = I_0 \Delta R \tag{7.4}$$

The voltage signal is connected to a band pass filter, which is designed to work in frequency range from 25 kHz to 500 kHz. Then the signal is amplified by a factor of 50. A lock-in amplifier model SR844 from Stanford research system is used to recover the baseband signal and improve the signal-to-noise ratio. The in-phase and quadrature components of the signal are transferred from the lock-in amplifier to a computer though a GPIB cable and stored.

7.6 Experimental Results and Discussion

7.6.1 Axial and Circumferential Notches

Steam generator tube with machined axial and circumferential notches is inspected using the prototype probe. The tube material is INCONEL 690. The inner and outer radius of the tube is 9.84mm, and 11.11mm respectively. The machined notches' dimensions and locations are specified in Figure 7.16. The axial excitation current changes direction along the dash lines.

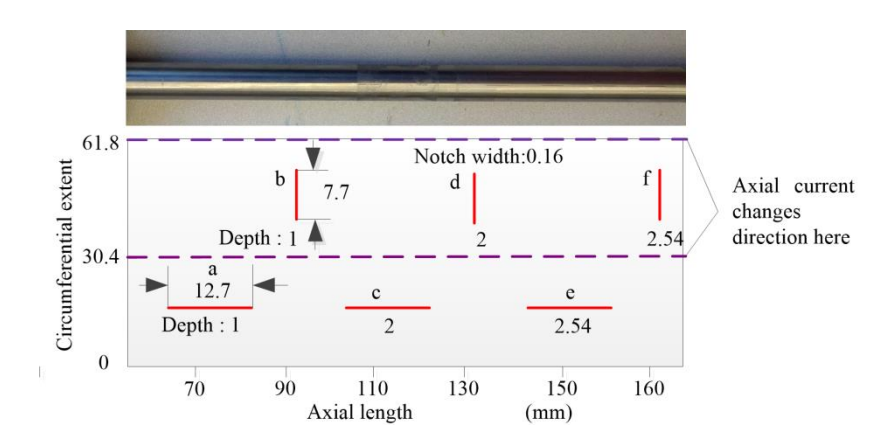


Figure 7.16. Geometry dimensions of steam generator tube sample with machined notches.

Experimental C-scan images of the axial notches are presented in Figure 7.17 and the images of the circumferential notches are presented Figure 7.18. For the purposes of comparison these experimentally derived images should be compared with the simulation results.

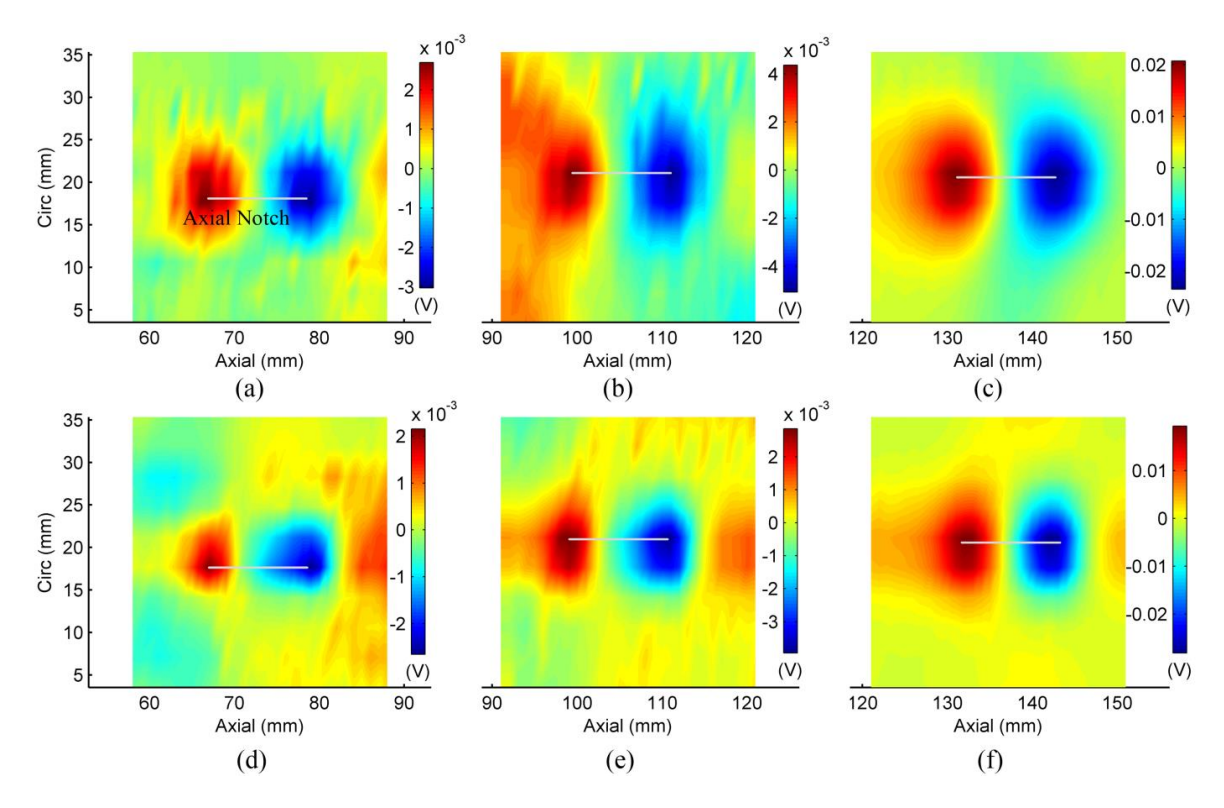


Figure 7.17. Experimental output images of RoC-GMR probe of OD axial notches. (a) –(c) in phase (real) component for depths 60%,80%, and 100% of tube wall; (d) –(f) quadrature (imaginary) component for depths 60%,80%, and 100% of tube wall.

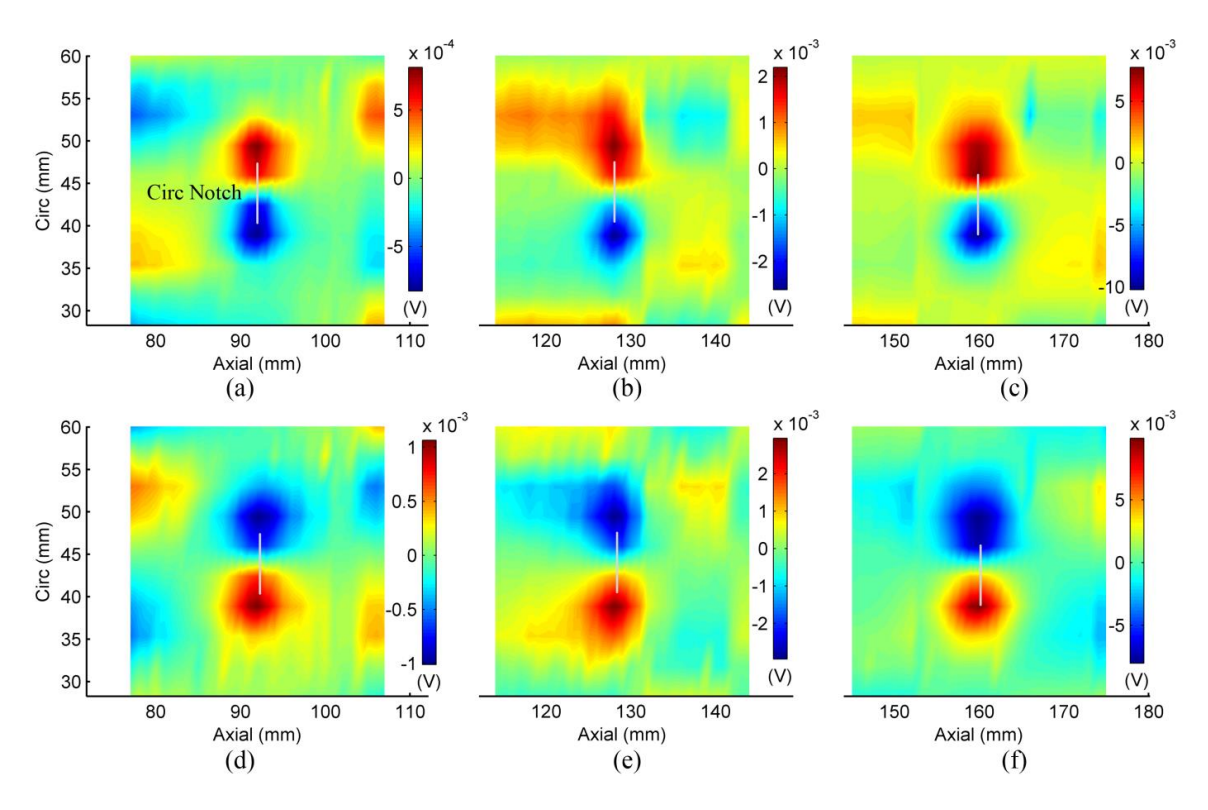


Figure 7.18. Experimental output images of RoC-GMR probe of OD circumferential notches. (a) –(c) in phase component for depths 60%,80%, and 100% of tube wall; (d) –(f) quadrature component for depths 60%,80%, and 100% of tube wall.

As seen in the simulation results, both axial and circumferential notches are detected experimentally by the prototype RoC-GMR probe. The magnitude of the signals from axial and circumferential notches are comparable indicating that the probe has similar sensitivity to defect at different orientations. For notches, the experimental C-scan image also has two lobes located at the two ends of the defect.

The through notches (depth 100% of tube wall) have strongest signal and best signal to noise ratio. However, for depth 60% and 80% TW notches, the signal is lower And noisier. One main source of the noise is vibriation of the probe during scan, which can be greatly reduced by improving the scan control.

To further analyze the data of different depth notches; Lissajous Pattern seen of inphase and quadrature component of line scan along the axial direction through the defect center of the data shown in Figure 7.17 is presented in Figure 7.19. This result should be compared with the simulation results shown in Figure 7.10 qualitatively.

Amplitude of \bar{B}_r measured along a line scan through the C-scan data shown in Figure 7.17 is presented in Figure 7.20. It is seen that the magnitude of the signal is positively correlated with the defect depth. The peak value of experimental signal of axial notch of depth 80% tube wall is 2.68×10^{-5} T, whereas the simulation result of axial notch of depth 87.5% tube wall is 2.42×10^{-5} T. The simulation and experimental results are therefore considered to be reasonably close. The difference between simulation and experiment results is due to the fact that the parameters of the circumferential coil, e.g. number of turns and height, used in the simulation model are not identical to that of the experimental system. Further, material properties used in simulation may also vary from actual values of the test sample.

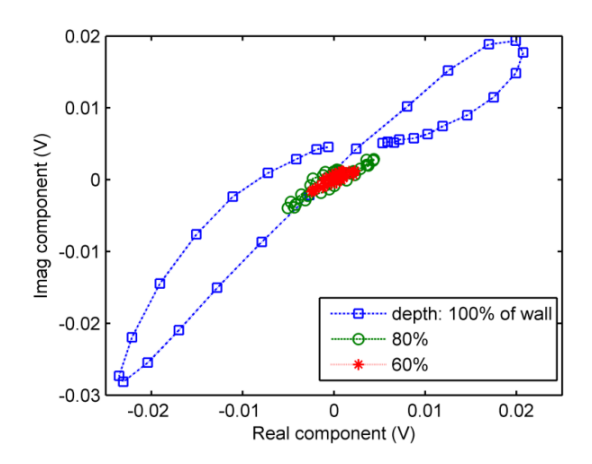


Figure 7.19. Lissajous Pattern of the line scan along the axial direction through the defect center of the experimental data shown in Figure 7.17.

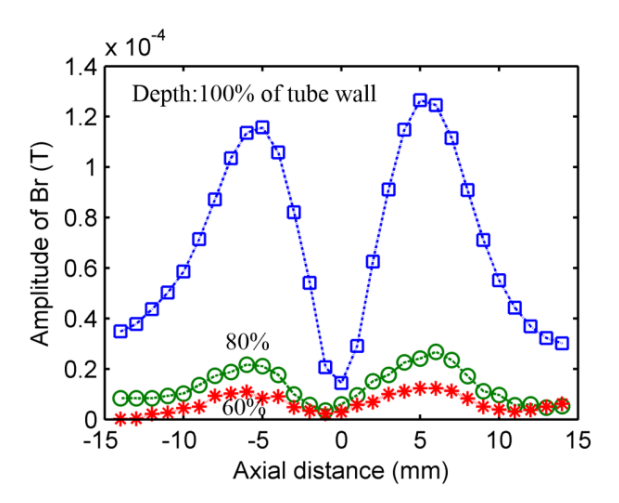


Figure 7.20. Amplitude of \bar{B}_r along the axial direction through the defect center of the experimental data shown in Figure 7.17.

7.6.2 Flat Bottom Hole

Next, a 3mm diameter circular flat-bottomed hole in the tube wall is inspected using the RoC-GMR prototype probe. The flat bottom hole is through the tube wall (100%TW). The excitation current frequency was 30 kHz. Amplitudes of the current in the axial coil and the circumferential coil were 261 mA and 113 mA respectively. Amplitude of the axial current is greater than that of circumferential current since it has been found from previous experimental results that the signal generated by axial current is weaker than that generated by circumferential coil, which is due to the fact that the axial coil is sparser than the circumferential coil. The real and imaginary

components of the simulation results are presented in Figure 7.21. This experimental result can be compared with the simulation result presented in Figure 7.14 qualitatively. The experimental results validate the simulation model and demonstrate the feasibility of the novel probe design.

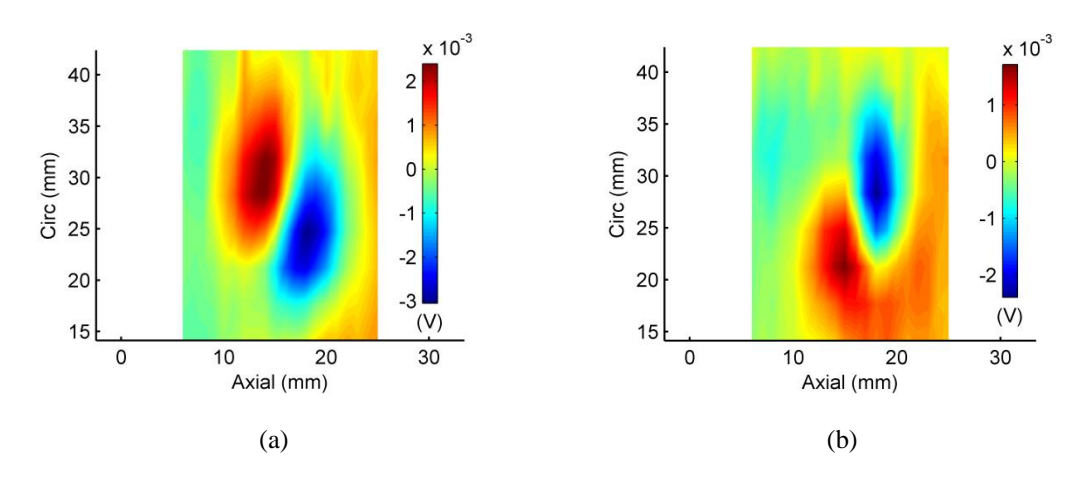


Figure 7.21. Experimental result of 3mm diameter flat bottom hole: (a) in-phase component; (b) quadrature component.

7.7 Conclusion

A novel probe for steam generator tube inspection has been presented in this chapter. The probe employs a rotating eddy current excitation; consequently it is sensitive to defect of all orientations.

GMR array sensors are used to measure the radial component of magnetic field. GMR sensors offer high sensitivity over a wide range of frequencies and provide potentially very high space resolution.

Experimental results obtained using the prototype probe to inspect steam generator tube with machined notches show that both axial and circumferential notches are detected with similar sensitivity. One can determine defect location and orientation, as well as can characterize and size defect from the output C-scan image of the probe. Experimental results from steam generator tube with flat bottom hole show that flat

bottom holes are detected by the probe. Experimental results validate the simulation model and further demonstrate the feasibility of the concepts that are presented.

The probe can be used for detecting defects in steam generator tubes in nuclear power

plants. However a significant amount of development and testing remains to be done.

Chapter 8 Summary and Future Work

8.1 Accomplishments and Conclusions

This thesis considered the inspection of planar, riveted multilayer geometries in airframes and tube geometries encountered in heat exchange units. The shortcomings of existing probes used in industry had been outline. The research carried out during the course of this dissertation was focused on addressing these shortcomings. The research has resulted in the following contributions to the field of electromagnetic NDE.

- (1) Presented a new approach using differential GMR sensor arrays together with rotating current excitation for the detection of fatigue cracks around fasteners with arbitrary orientation in multilayer structures. Differential measurement scheme takes into account the need for eliminating the ambient/background field of orthogonal coils in the case of array sensors.
- (2) Presented a new optimized non-uniform distributed multilayer orthogonal coil design fabricated on multi-layer print circuit board so as to generate more uniform excitation fields.
- (3) The effect of magnetic anisotropy of the steel fastener on the image data was identified as an issue and analyzed.
- (4) A novel scheme, based on MBM method with MR sensor for inspecting defect around steel fasteners was proposed. The bias point of the MR sensor in MBM was kept constant, so the effect of the strong remanence field is eliminated and characteristic of the sensor is kept constant.
- (5) A novel rotating transceiver eddy current probe for tube inspection has been presented, simulated and experimentally validated.

(6) Novel RoC-GMR probe for tube inspection was proposed. The feasibility of the probe was studied numerically and validated experimentally. Both axial and circumferential notches, as well as flat bottom hole are detected using the RoC-GMR probe. Defect location, orientation and size can be estimated from the output C-scan image of the probe.

8.2 Future Work

Although the proposed probes have been studied numerically and validated experimentally in lab, they are not tested on real structures with real defects in field. These probes most be further developed and extensively tested in the coming years.

8.2.1 RoC-GMR probe for multilayer structure inspection

- (1) Further improvement in sensitivity, signal to noise ratio and reduction of overall size of the probe need to be addressed.
- (2) Optimize the probe design to improve its performance for complex geometry inspection, e.g. fastener with close edge, curved surface etc.
- (3) Integrate the compensation coil of MBM method on MR sensor chip to reduce its overall size. Develop a simple and effective PID controller analog circuit to replace SRS SIM 960 analog PID controller to reduce the system cost and size.

8.2.2 RoC-GMR probe for tube inspection

- (1) Integrate the GMR sensors and multiplexer circuit in a single chip to improve its spatial resolution.
- (2) Optimize the parameters of the excitation coils to improve the probe's performance, including the coils' height, diameter, number of turns and excitation current amplitudes and frequency.

- (3) Develop suitable mechanical structure to keep the lift-off constant and reduce vibration during scan for the probe, so as to increase signal to noise ratio.
- (4) Develop post processing algorithm to locate, size and characterize defect from the output image of the probe.

BIBLIOGRAPHY

BIBLIOGRAPHY

- [1] A. S. M. Handbook, "Nondestructive evaluation and quality control," *ASM Int.*, vol. 17, p. 5, 1992.
- [2] T. Warren and J. Ni, "An automated radiographic NDT system for weld inspection," *NDTE Int.*, vol. 29, no. 3, pp. 157–162, 1996.
- [3] J. Krautkrämer and H. Krautkrämer, "Ultrasonic testing of materials. 3," 1975.
- [4] O. P. Moore ,S. S. Udpa, *Nondestructive testing handbook: eletromagnetic testing*, American Society for Nondestructive Testing, 2004.
- [5] D. Jiles, "Review of Magnetic Methods for Nondestructive Evaluation," *Ndt Int.*, vol. 21, no. 5, pp. 311–319, Oct. 1988.
- [6] D. J. Groner and D. E. Nieser, "U. S. Air Force aging aircraft corrosion," *Can. Aeronaut. Space J.*, vol. 42, no. 2, pp. 63–67, 1996.
- [7] G. Almeida, J. Gonzalez, L. Rosado, P. Vilaça, and T. G. Santos, "Advances in NDT and Materials Characterization by Eddy Currents," *Procedia CIRP*, vol. 7, pp. 359–364, Jan. 2013.
- [8] P. Xu, S. Huang, and W. Zhao, "A new differential eddy current testing sensor used for detecting crack extension direction," *NDT E Int.*, vol. 44, no. 4, pp. 339–343, Jul. 2011.
- [9] L. S. Rosado, J. C. Gonzalez, T. G. Santos, P. M. Ramos, and M. Piedade, "Geometric optimization of a differential planar eddy currents probe for non-destructive testing," *Sens. Actuators Phys.*, vol. 197, pp. 96–105, Aug. 2013.
- [10]T. Dogaru and S. T. Smith, "Giant magnetoresistance-based eddy-current sensor," *IEEE Trans. Magn.*, vol. 37, no. 5, pp. 3831–3838, Sep. 2001.
- [11] L. S. Rosado, F. A. Cardoso, S. Cardoso, P. M. Ramos, P. P. Freitas, and M. Piedade, "Eddy currents testing probe with magneto-resistive sensors and differential measurement," *Sens. Actuators -Phys.*, vol. 212, pp. 58–67, Jun. 2014.
- [12] R. Hamia, C. Cordier, S. Saez, and C. Dolabdjian, "Eddy-Current Nondestructive Testing Using an Improved GMR Magnetometer and a Single Wire as Inducer: A FEM Performance Analysis," *Ieee Trans. Magn.*, vol. 46, no. 10, pp. 3731–3737, Oct. 2010.
- [13] J. H. Espina-Hernandez, E. Ramirez-Pacheco, F. Caleyo, J. A. Perez-Benitez, and J. M. Hallen, "Rapid estimation of artificial near-side crack dimensions in aluminium using a GMR-based eddy current sensor," *Ndt E Int.*, vol. 51, pp. 94–100, Oct. 2012.

- [14] R. Hamia, C. Cordier, and C. Dolabdjian, "Eddy-current non-destructive testing system for the determination of crack orientation," *Ndt E Int.*, vol. 61, pp. 24–28, Jan. 2014.
- [15] N. Lei, L. Udpa, S. Udpa, and Z. Zeng, "Rotating field eddy current (RoFEC)-probe for steam generator inspection," *Int. J. Appl. Electromagn. Mech.*, vol. 33, no. 3–4, pp. 1279–1285, 2010.
- [16] Y. Le Diraison and P.-Y. Joubert, "Rotating Field Eddy Current Imaging for the Non-Destructive Evaluation of Buried and Oriented Defects in Riveted Lap-Joints," *Sens. Lett.*, vol. 7, no. 3, pp. 406–411, Jun. 2009.
- [17] M. Kurokawa, R. Miyauchi, K. Enami, and M. Matsumoto, "New eddy current probe for NDE of steam generator tubes," *Stud. Appl. Electromagn. Mech.*, vol. 15, pp. 57–64, 1999.
- [18] P. E. MacDonald, V. N. Shah, L. W. Ward, and P. G. Ellison, *Steam generator tube failures*. Safety Programs Division, Office for Analysis and Evaluation of Operational Data, US Nuclear Regulatory Commission, 1996.
- [19] V. Monebhurrun, B. Duchêne, and D. Lesselier, "Three-dimensional inversion of eddy current data for non-destructive evaluation of steam generator tubes," *Inverse Probl.*, vol. 14, no. 3, p. 707, 1998.
- [20] T. Takagi, M. Uesaka, and K. Miya, "Electromagnetic NDE research activities in JSAEM," in *Electromagnetic Nondestructive Evaluation*, vol. 12, T. Takagi, J. R. Bowler, and Y. Yoshida, Eds. 1997, pp. 9–16.
- [21] L. S. Obrutsky, V. S. Cecco, S. P. Sullivan, and D. Humphrey, "Transmit receive eddy current probes for circumferential cracks in heat exchanger tubes," *Mater. Eval.*, vol. 54, no. 1, pp. 93–98, Jan. 1996.
- [22] B. Raj and T. Jayakumar, "NDE methodologies for characterisation of defects, stresses and microstructures in pressure vessels and pipes," *Int. J. Press. Vessels Pip.*, vol. 73, no. 2, pp. 133–146, Sep. 1997.
- [23] P. Y. Joubert, D. Miller, D. Placko, and E. Savin, "Multi-detector eddy current probe for the non-destructive evaluation of steam generator tubes, designed for an imaging approach," in *Electromagnetic Nondestructive Evaluation (iii)*, vol. 15, D. Lesselier and A. Razek, Eds. 1999, pp. 34–44.
- [24] G. J. Saulnier, R. S. Blue, J. C. Newell, D. Isaacson, and P. M. Edic, "Electrical impedance tomography," *IEEE Signal Process. Mag.*, vol. 18, no. 6, pp. 31–43, Nov. 2001.
- [25] M. Cheney, D. Isaacson, and J. C. Newell, "Electrical impedance tomography," *Siam Rev.*, vol. 41, no. 1, pp. 85–101, Mar. 1999.
- [26] Y. Zou and Z. Guo, "A review of electrical impedance techniques for breast cancer detection," *Med. Eng. Phys.*, vol. 25, no. 2, pp. 79–90, Mar. 2003.

- [27] Y. Deng and X. Liu, "Electromagnetic Imaging Methods for Nondestructive Evaluation Applications," *Sensors*, vol. 11, no. 12, pp. 11774–11808, Dec. 2011.
- [28] J. Xin, "Design and analysis of rotating field eddy current probe for tube inspection," MICHIGAN STATE UNIVERSITY, 2014.
- [29] G. L. Nicholson, A. G. Kostryzhev, X. J. Hao, and C. L. Davis, "Modelling and experimental measurements of idealised and light-moderate RCF cracks in rails using an ACFM sensor," *NDT E Int.*, vol. 44, no. 5, pp. 427–437, Sep. 2011.
- [30] M. Ph Papaelias, C. Roberts, and C. L. Davis, "A review on non-destructive evaluation of rails: state-of-the-art and future development," *Proc. Inst. Mech. Eng. Part F J. Rail Rapid Transit*, vol. 222, no. 4, pp. 367–384, Dec. 2008.
- [31] K. Arunachalam, V. R. Melapudi, L. Udpa, and S. S. Udpa, "Microwave NDT of cement-based materials using far-field reflection coefficients," *NDT E Int.*, vol. 39, no. 7, pp. 585–593, Oct. 2006.
- [32] M. Sayar, D. Seo, and K. Ogawa, "Non-destructive microwave detection of layer thickness in degraded thermal barrier coatings using K- and W-band frequency range," *NDT E Int.*, vol. 42, no. 5, pp. 398–403, Jul. 2009.
- [33] J. P. Guillet, B. Recur, L. Frederique, B. Bousquet, L. Canioni, I. Manek-Hönninger, P. Desbarats, and P. Mounaix, "Review of Terahertz tomography techniques," *J. Infrared Millim. Terahertz Waves*, vol. 35, no. 4, pp. 382–411, 2014.
- [34] D. Saeedkia, Handbook of Terahertz Technology for Imaging, Sensing and Communications. Elsevier, 2013.
- [35] C. Jansen, S. Wietzke, O. Peters, M. Scheller, N. Vieweg, M. Salhi, N. Krumbholz, C. Jördens, T. Hochrein, and M. Koch, "Terahertz imaging: applications and perspectives," *Appl. Opt.*, vol. 49, no. 19, pp. E48–E57, 2010.
- [36] M. Tonouchi, "Cutting-edge terahertz technology," *Nat. Photonics*, vol. 1, no. 2, pp. 97–105, 2007.
- [37] A. Dobroiu, C. Otani, and K. Kawase, "Terahertz-wave sources and imaging applications," *Meas. Sci. Technol.*, vol. 17, no. 11, p. R161, 2006.
- [38] D. M. Mittleman, M. Gupta, R. Neelamani, R. G. Baraniuk, J. V. Rudd, and M. Koch, "Recent advances in terahertz imaging," *Appl. Phys. B*, vol. 68, no. 6, pp. 1085–1094, 1999.
- [39] D. Grischkowsky, S. Keiding, M. Van Exter, and C. Fattinger, "Far-infrared time-domain spectroscopy with terahertz beams of dielectrics and semiconductors," *JOSA B*, vol. 7, no. 10, pp. 2006–2015, 1990.
- [40] G. J. Wilmink, B. L. Ibey, T. Tongue, B. Schulkin, N. Laman, X. G. Peralta, C. C. Roth, C. Z. Cerna, B. D. Rivest, J. E. Grundt, and others, "Development of a compact terahertz time-domain spectrometer for the measurement of the optical

- properties of biological tissues," *J. Biomed. Opt.*, vol. 16, no. 4, pp. 47006–47006, 2011.
- [41] N. Oda, T. Ishi, S. Kurashina, T. Sudou, M. Miyoshi, T. Morimoto, T. Yamazaki, T. Tsuboi, and T. Sasaki, "Palm-size and real-time terahertz imager, and its application to development of terahertz sources," 2013, vol. 8716, pp. 871603-871603-10.
- [42] G. Yang, A. Tamburrino, L. Udpa, S. S. Udpa, Z. Zeng, Y. Deng, and P. Que, "Pulsed Eddy-Current Based Giant Magnetoresistive System for the Inspection of Aircraft Structures," *Ieee Trans. Magn.*, vol. 46, no. 3, pp. 910–917, Mar. 2010.
- [43] R. Ludwig and X.-W. Dai, "Numerical and analytical modeling of pulsed eddy currents in a conducting half-space," *IEEE Trans. Magn.*, vol. 26, no. 1, pp. 299–307, Jan. 1990.
- [44] J. C. Moulder and J. A. Bieber, "Pulsed eddy-current measurements of corrosion and cracking in aging aircraft," in *Nondestructive Characterization of Materials in Aging Systems*, vol. 503, R. L. Crane, J. D. Achenbach, S. P. Shah, T. E. Matikas, P. T. KhuriYakub, and R. S. Gilmore, Eds. Warrendale: Materials Research Society, 1998, pp. 263–268.
- [45] J. Bowler and M. Johnson, "Pulsed eddy-current response to a conducting half-space," *IEEE Trans. Magn.*, vol. 33, no. 3, pp. 2258–2264, May 1997.
- [46] R. H. Cole, "Time Domain Reflectometry," *Annu. Rev. Phys. Chem.*, vol. 28, no. 1, pp. 283–300, 1977.
- [47] D. A. Robinson, S. B. Jones, J. M. Wraith, D. Or, and S. P. Friedman, "A Review of Advances in Dielectric and Electrical Conductivity Measurement in Soils Using Time Domain Reflectometry," *Vadose Zone J.*, vol. 2, no. 4, p. 444, 2003.
- [48] R. Matsuzaki, Y. Nozawa, A. Todoroki, and M. Kawasaki, "Crack visualization of metallic structures using time-domain reflectometry with two-dimensional microstrip lines," *NDT E Int.*, vol. 66, pp. 34–42, Sep. 2014.
- [49] N. Ida and W. Lord, "A finite element model for three-dimensional Eddy current NDT phenomena," *IEEE Trans. Magn.*, vol. 21, no. 6, pp. 2635–2643, Nov. 1985.
- [50] Z. Zeng, L. Udpa, S. S. Udpa, and M. S. C. Chan, "Reduced Magnetic Vector Potential Formulation in the Finite Element Analysis of Eddy Current Nondestructive Testing," *IEEE Trans. Magn.*, vol. 45, no. 3, pp. 964–967, Mar. 2009.
- [51] E. X. Xu and J. Simkin, "Total and reduced magnetic vector potentials and electrical scalar potential for eddy current calculation," *Ieee Trans. Magn.*, vol. 40, no. 2, pp. 938–940, Mar. 2004.

- [52] J. Lenz and A. S. Edelstein, "Magnetic sensors and their applications," *Ieee Sens. J.*, vol. 6, no. 3, pp. 631–649, Jun. 2006.
- [53] F. Primdahl, "The fluxgate magnetometer," *J. Phys. [E]*, vol. 12, no. 4, p. 241, Apr. 1979.
- [54] W. G. Jenks, S. S. H. Sadeghi, and J. P. Wikswo, "SQUIDs for nondestructive evaluation," *J. Phys. -Appl. Phys.*, vol. 30, no. 3, pp. 293–323, Feb. 1997.
- [55] S. T. Keenan and E. J. Romans, "Compensated high temperature SQUID gradiometer for mobile NDE in magnetically noisy environments," *NDT E Int.*, vol. 47, pp. 1–6, Apr. 2012.
- [56] M. Le, J. Lee, J. Jun, J. Kim, S. Moh, and K. Shin, "Hall sensor array based validation of estimation of crack size in metals using magnetic dipole models," *Ndt E Int.*, vol. 53, pp. 18–25, Jan. 2013.
- [57] U. Holm, H. Sohlstrom, and T. Brogardh, "Measurement system for magneto-optic sensor materials," *J. Phys. [E]*, vol. 17, no. 10, p. 885, Oct. 1984.
- [58] S. J. Lee, S. H. Song, D. C. Jiles, and H. Hauser, "Magnetooptic sensor for remote evaluation of surfaces," *IEEE Trans. Magn.*, vol. 41, no. 7, pp. 2257–2259, Jul. 2005.
- [59] K. Chomsuwan, S. Yamada, and M. Iwahara, "Improvement on Defect Detection Performance of PCB Inspection Based on ECT Technique With Multi-SV-GMR Sensor," *IEEE Trans. Magn.*, vol. 43, no. 6, pp. 2394–2396, Jun. 2007.
- [60] L.-W. Guo and J.-Y. Ma, "High-sensitive biosensor based on GMR in self-suspended grating," *Guangzi XuebaoActa Photonica Sin.*, vol. 41, no. 12, pp. 1483–1487, 2012.
- [61] N. V. Nair, V. R. Melapudi, H. R. Jimenez, X. Liu, Y. Deng, Z. Zeng, L. Udpa, T. J. Moran, and S. S. Udpa, "A GMR-Based Eddy Current System for NDE of Aircraft Structures," *IEEE Trans. Magn.*, vol. 42, no. 10, pp. 3312–3314, Oct. 2006.
- [62] M. von Kreutzbruck, K. Allweins, T. Ruhl, M. Muck, C. Heiden, H. J. Krause, and R. Hohmann, "Defect detection and classification using a SQUID based multiple frequency eddy current NDE system," *Ieee Trans. Appl. Supercond.*, vol. 11, no. 1, pp. 1032–1037, Mar. 2001.
- [63] M. V. Kreutzbruck, U. Baby, A. Theiss, M. Muck, and C. Heiden, "Inspection of aircraft parts with high remanent magnetization by eddy current SQUID NDE," *IEEE Trans. Appl. Supercond.*, vol. 9, no. 2, pp. 3805–3808, Jun. 1999.
- [64] R. Hohmann, M. Maus, D. Lomparski, M. Gruneklee, Y. Zhang, H.-J. Krause, H. Bousack, and A. I. Braginski, "Aircraft wheel testing with machine-cooled HTS SQUID gradiometer system," *IEEE Trans. Appl. Supercond.*, vol. 9, no. 2, pp. 3801–3804, Jun. 1999.

- [65] M. v.Kreutzbruck, K. Troll, M. Muck, C. Heiden, and Y. Zhang, "Experiments on eddy current NDE with HTS rf SQUIDS," *IEEE Trans. Appl. Supercond.*, vol. 7, no. 2, pp. 3279–3282, Jun. 1997.
- [66] M. Mück, M. v Kreutzbruck, U. Baby, J. Tröll, and C. Heiden, "Eddy current nondestructive material evaluation based on HTS SQUIDs," *Phys. C Supercond.*, vol. 282–287, Part 1, pp. 407–410, Aug. 1997.
- [67] G. Yang, Z. Zeng, Y. Deng, X. Liu, L. Udpa, A. Tamburrino, and S. S. Udpa, "3D EC-GMR sensor system for detection of subsurface defects at steel fastener sites," *NDT E Int.*, vol. 50, pp. 20–28, Sep. 2012.
- [68] G. Yang, G. Dib, L. Udpa, A. Tamburrino, and S. S. Udpa, "Rotating Field EC-GMR Sensor for Crack Detection at Fastener Site in Layered Structures," *IEEE Sens. J.*, pp. 1–1, 2014.
- [69] C. Ye, Y. Huang, L. Udpa, and S. S. Udpa, "Differential Sensor Measurement with Rotating Current Excitation for Evaluating Multilayer Structures," *IEEE Sens. J.*, vol. PP, no. 99, pp. 1–1, 2015.
- [70] D. Rogers and A. Hopfinger, "Application of Genetic Function Approximation to Quantitative Structure-Activity-Relationships and Quantitative Structure-Property Relationships," *J. Chem. Inf. Comput. Sci.*, vol. 34, no. 4, pp. 854–866, Aug. 1994.
- [71] M. Morris, "Factorial Sampling Plans for Preliminary Computational Experiments," *Technometrics*, vol. 33, no. 2, pp. 161–174, May 1991.
- [72] V. Jones, "A Polynomial Invariant for Knots Via Vonneumann-Algebras," *Bull. Am. Math. Soc.*, vol. 12, no. 1, pp. 103–111, 1985.
- [73] "GF708 MagnetoResistive Magnetic Field Sensor." [Online]. Available: http://www.sensitec.com/english/products/magnetic-field/gf708.html.
- [74] F. Mart ´n-Hern ´andez, M. J. Dekkers, I. M. A. Bominaar-Silkens, and J. C. Maan, "Magnetic anisotropy behaviour of pyrrhotite as determined by low- and high-field experiments," *Geophys. J. Int.*, vol. 174, no. 1, pp. 42–54, Jul. 2008.
- [75] T. Nagata, "Basic magnetic properties of rocks under the effects of mechanical stresses," *Tectonophysics*, vol. 9, no. 2, pp. 167–195, 1970.
- [76] H. František, "Low-field variation of magnetic susceptibility and its effect on the anisotropy of magnetic susceptibility of rocks," *Geophys. J. Int.*, vol. 150, no. 3, pp. 715–723, Sep. 2002.
- [77] M. Blaszkiewicz, L. Albertin, and W. Junker, "The Eddy current technique for determining residual stresses in steels," in *Nondestructive Characterization of Materials Vii, Pts 1 and 2*, vol. 210–2, A. L. Bartos, R. E. Green, and C. O. Ruud, Eds. Stafa-Zurich: Trans Tech Publications Ltd, 1996, pp. 179–185.

- [78] L. Luming, H. Songling, W. Xiaofeng, S. Keren, and W. Su, "Magnetic field abnormality caused by welding residual stress," *J. Magn. Magn. Mater.*, vol. 261, no. 3, pp. 385–391, 2003.
- [79] S. Chikazumi, *Physics of Ferromagnetism 2e*. Oxford University Press, 2009.
- [80] Z. Włodarski, "Analytical description of magnetization curves," *Phys. B Condens. Matter*, vol. 373, no. 2, pp. 323–327, Mar. 2006.
- [81] G. Biorci and D. Pescetti, "Analytical theory of the behaviour of ferromagnetic materials," *Il Nuovo Cimento*, vol. 7, no. 6, pp. 829–842, Mar. 1958.
- [82] F. Fiorillo, L. R. Dupre, C. Appino, and A. Rietto, "Comprehensive model of magnetization curve, hysteresis loops, and losses in any direction in grain-oriented Fe-Si," *IEEE Trans. Magn.*, vol. 38, no. 3, pp. 1467–1476, May 2002.
- [83] V. Basso and G. Bertotti, "Description of magnetic interactions and Henkel plots by the Preisach hysteresis model," *IEEE Trans. Magn.*, vol. 30, no. 1, pp. 64–72, Jan. 1994.
- [84] D. J. Craik and M. J. Wood, "Magnetization changes induced by stress in a constant applied field," *J. Phys. Appl. Phys.*, vol. 3, no. 7, p. 1009, Jul. 1970.
- [85] V. Zablotskii, J. I. Perez-Landazabal, V. Recarte, and C. Gomez-Polo, "Temperature dependence of magnetic susceptibility in the vicinity of martensitic transformation in ferromagnetic shape memory alloys," *J. Phys.-Condens. Matter*, vol. 22, no. 31, p. 316004, Aug. 2010.
- [86] A. Kosterov, "Low-temperature magnetization and AC susceptibility of magnetite: effect of thermomagnetic history," *Geophys. J. Int.*, vol. 154, no. 1, pp. 58–71, Jul. 2003.
- [87] L. Warne, "Eddy-Current Power Dissipation at Sharp Corners an External Impedance Solution Applied to a Wedge with Large Ratio of Internal to External Magnetic Permeabilities," *J. Electromagn. Waves Appl.*, vol. 8, no. 7, pp. 933–956, 1994.
- [88] A. Skauge and B. Matre, "3-Phase Relative Permeabilities in Brine Oil Microemulsion Systems," *Situ*, vol. 15, no. 1, pp. 35–61, 1991.
- [89] V. L. Kostenko, "Microwave measurements of the complex permittivities and permeabilities of magnetodielectrics," *Meas. Tech.*, vol. 39, no. 4, pp. 429–431, Apr. 1996.
- [90] R. Birss, "Magnetomechanical effects in the Rayleigh region," *IEEE Trans. Magn.*, vol. 7, no. 1, pp. 113–133, Mar. 1971.
- [91] A. Koller, E. Pfrenger, and K. Stierstadt, "New Interpretation of the Rayleigh Law," *J. Appl. Phys.*, vol. 39, no. 2, pp. 869–870, Feb. 1968.
- [92] H. Markert and A. Lehmann, "Three-dimensional Rayleigh hysteresis of oriented core samples from the German Continental Deep Drilling Program:

- susceptibility tensor, Rayleigh tensor, three-dimensional Rayleigh law," *Geophys. J. Int.*, vol. 127, no. 1, pp. 201–214, Oct. 1996.
- [93] N. Tsyganenko, "Global Quantitative Models of the Geomagnetic-Field in the Cislunar Magnetosphere for Different Disturbance Levels," *Planet. Space Sci.*, vol. 35, no. 11, pp. 1347–1358, Nov. 1987.
- [94] Y. Guyodo and J. P. Valet, "Global changes in intensity of the Earth's magnetic field during the past 800 kyr," *Nature*, vol. 399, no. 6733, pp. 249–252, May 1999.
- [95] "World Magnetic Model Home Page." [Online]. Available: http://www.ngdc.noaa.gov/geomag/WMM/DoDWMM.shtml. [Accessed: 12-May-2015].
- [96] K. H. Ang, G. Chong, and Y. Li, "PID control system analysis, design, and technology," *IEEE Trans. Control Syst. Technol.*, vol. 13, no. 4, pp. 559–576, Jul. 2005.
- [97] L. Cohen, B. Roth, J. Nilsson, N. Dang, M. Panizza, S. Bandinelli, W. Friauf, and M. Hallett, "Effects of Coil Design on Delivery of Focal Magnetic Stimulation Technical Considerations," *Electroencephalogr. Clin. Neurophysiol.*, vol. 75, no. 4, pp. 350–357, Apr. 1990.
- [98] J. Kirschvink, "Uniform Magnetic-Fields and Double-Wrapped Coil Systems Improved Techniques for the Design of Bioelectromagnetic Experiments," *Bioelectromagnetics*, vol. 13, no. 5, pp. 401–411, 1992.
- [99] D. R. Diercks, W. J. Shack, and J. Muscara, "Overview of steam generator tube degradation and integrity issues," *Nucl. Eng. Des.*, vol. 194, no. 1, pp. 19–30, Nov. 1999.
- [100] D. R. Diercks, J. Muscara, and W. J. Shack, "Steam generator tube integrity program," *Nucl. Eng. Des.*, vol. 165, no. 1–2, pp. 143–149, Aug. 1996.
- [101] J. B. Lee, J. H. Park, S. H. Lee, H. D. Kim, and H. S. Chung, "Prediction of crack growth in steam generator tubes using Monte Carlo simulation," *Cmes-Comput. Model. Eng. Sci.*, vol. 11, no. 1, pp. 9–16, Jan. 2006.
- [102] H. Fukutomi, T. Takagi, and M. Nishikawa, "Remote field eddy current technique applied to non-magnetic steam generator tubes," *NDT E Int.*, vol. 34, no. 1, pp. 17–23, Jan. 2001.
- [103] H. Huang, N. Sakurai, T. Takagi, and T. Uchimoto, "Design of an eddy-current array probe for crack sizing in steam generator tubes," *NDT E Int.*, vol. 36, no. 7, pp. 515–522, Oct. 2003.
- [104] J. Xin, N. Lei, L. Udpa, and S. S. Udpa, "Rotating field eddy current probe with bobbin pickup coil for steam generator tubes inspection," *Ndt E Int.*, vol. 54, pp. 45–55, Mar. 2013.

- [105] J. Xin, N. Lei, L. Udpa, and S. S. Udpa, "Nondestructive Inspection Using Rotating Magnetic Field Eddy-Current Probe," *IEEE Trans. Magn.*, vol. 47, no. 5, pp. 1070–1073, May 2011.
- [106] Chaofeng Ye, Yue Huang, L.Udpa, and S.S. UDPA, "Rotating Current EC GMR Probe with Differential Measurement for Inspecting Multilayer Riveted Structures," Sens. J. IEEE.
- [107] J. Xin, E. Tarkleson, N. Lei, L. Udpa, and S. S. Udpa, "Novel Rotating Field Probe for Inspection of Tubes," *Rev. Prog. Quant. Nondestruct. Eval. Vols 31a* 31b, vol. 1430, pp. 358–365, 2012.
- [108] Z. Zeng, L. Udpa, and S. S. Udpa, "Finite-Element Model for Simulation of Ferrite-Core Eddy-Current Probe," *Ieee Trans. Magn.*, vol. 46, no. 3, pp. 905–909, Mar. 2010.
- [109] Y. Y. Yao, H. X. Xia, G. Z. Ni, X. B. Liang, S. Y. Yang, and P. H. Ni, "3-D Eddy current analysis in the end region of a turbogenerator by using reduced magnetic vector potential," *Ieee Trans. Magn.*, vol. 42, no. 4, pp. 1323–1326, Apr. 2006.
- [110] Z. Zeng, X. Liu, Y. Deng, L. Udpa, and S. Udpa, "Reduced magnetic vector potential and electric scalar potential formulation for eddy current modeling," *Przeglad Elektrotechniczny*, vol. 83, no. 6, pp. 35–37, 2007.
- [111] M. Valentino, C. Bonavolonta, N. Marrocco, and G. P. Pepe, "Giant Magnetoresistive Second Order Electronic Gradiometer for Non-Destructive Evaluation Applications," *Sens. Lett.*, vol. 7, no. 3, pp. 390–393, Jun. 2009.
- [112] C. H. Smith, R. W. Schneider, T. Dogaru, and S. T. Smith, "GMR magnetic sensor arrays for NDE eddy-current testing," in *AIP Conference Proceedings*, 2003, vol. 657, pp. 419–426.